Material Removal Control for Teleoperated Robotic Sanding

Cameron Devine

A dissertation
submitted in partial fulfillment of the
requirements for the degree of

Doctor of Philosophy

University of Washington

2022

Reading Committee:
Santosh Devasia, Chair
Joseph Garbini, Chair
Ramulu Mamidala

Program Authorized to Offer Degree:
Mechanical Engineering

University of Washington

Abstract

Material Removal Control for Teleoperated Robotic Sanding

Cameron Devine

Co-Chairs of the Supervisory Committee:
Santosh Devasia
Department of Mechanical Engineering

Joseph Garbini
Department of Mechanical Engineering

During manufacturing of composite parts, minor surface defects are often repaired by applying fairing compound to the affected area and sanding to the desired surface profile. This sanding is commonly performed using hand-held sanding tools leading to ergonomic injuries. Teleoperated robotic sanding completely removes the operator from the dangerous forces and vibrations which were causing these injuries. Unfortunately, with teleoperated robotic sanding the operator's sensory perception is reduced making it difficult to effectively control the depth of material removed. For this reason it is desirable to automatically control the rate of material removal. However, existing methods for controlling the rate of material removal are not compatible with teleoperation as the path of the sander, and the speed along the path are unknown a priori. Therefore, a new method for controlling the rate of material removed was derived. Tests to validate this method have shown it reduces the spatial variation in depth of material removed by at least 30% in simulation vs constant force control. Similar experiments on physical robotic hardware have reduced the variation by at least 20%. Experiments with a human in the loop have shown an improvement of at least 19% in the spatial variation of material removed when compared to constant force control when using the physical robotic hardware. Several qualitative metrics also favor the proposed method.

For example, operators often felt they produced a better end result and could remove material more precisely with the proposed method. These results show that controlling the rate of material removal during teleoperated robotic sanding helps produce a better end result.

DEDICATION

To my wife, Tamara, and all the other individuals who have not been given a chance to earn a doctoral degree.

ACKNOWLEDGMENTS

Without the support of numerous individuals, this thesis would never have been completed. Of vital importance were my advisors, Professor Joseph Garbini and Professor Santosh Devasia, whose thoughtful questions and guidance were invaluable in this research and my overall development as an engineer and scholar. Without their advice and encouragement throughout both my Master's and Ph.D. programs, I would not be the person I am today. The input of my committee has also benefited this work in unique and key ways. Jim Buttrick brought to this project a wealth of hands-on knowledge of aerospace manufacturing, which added greatly to the background and motivation of this thesis. Professor Ramulu Mamidala provided key insights of the theoretical study of manufacturing processes, which proved valuable while modeling the sanding process. Professor Sam Burden offered many suggestions of possible uses and extensions of the methods proposed in this thesis, some of which are listed in the future work section. Finally, Professor Dwayne Arola, who graciously stepped in when one of my committee members was not able to attend my final exam.

I must also thank Jim Buttrick, Kevin Bray, and Sam Pedigo, respectively, the founding, former, and current directors of the Boeing Advanced Research Center, without whom this work would not have received funding. My fellow students in the BARC lab have also been essential in supporting this work. Particularly, Parker Owan, Tony Piaskowy, Ben Tereshchuk, and Kyle Schultz have been a consistent sounding board for ideas or troubleshooting problems. I am also grateful for the help of Peter Correa, William Hsieh, and Nikolay Bykov who helped work on various parts of this project. Most importantly, I must acknowledge the work of Lance McCann. As part of this project, he spent numerous hours interfacing between the BARC lab and Boeing. He streamlined many aspects of this project by sharing

his knowledge of designing, programming, and commissioning industrial systems from his career as a skilled controls engineer. Finally, he has been a friend, fellow Ph.D. student, and key sounding board for all aspects of this project.

Most of all, I need to thank my wife, Tamara Ramsay. They have both indirectly and directly supported this work in so many ways: putting up with "a little" extra work in the evenings, reading and editing drafts, listening when I would talk about whatever challenges I was facing in my research, and forcing me to take breaks from my work. Without them, it would have been difficult for me to have remained sane throughout this process.

TABLE OF CONTENTS

LIST OF FIGURES

LIST OF TABLES

Chapter 1

INTRODUCTION

This work aims to reduce ergonomic injuries stemming from hand sanding of composite parts by improving teleoperated robotic sanding to reduce surface height variation and decrease cycle times. The motivation for this work comes from aircraft interior panels which consist of two surfaces of fiberglass with a honeycomb structure in between. These panels are manufactured by squeezing the three layers together and heating the assembly to cure an epoxy resin. Different panel geometries can be created by squishing the part into the desired shape while curing. The resulting part is lightweight and strong, but when bent while green the weave of the fiberglass material can spread, creating pinholes in the part surface. These pinholes are filled using a process called "sweep and sand" where the affected area is covered with a fairing compound and sanded to remove the excess and ensure a smooth surface, which matches the original surface contour. This sanding is performed by hand and is known to cause ergonomic injuries such as repetitive stress injuries [1] in the wrist, elbow, and shoulder. These injuries are caused by the mechanic applying pressure to an orbital sander while moving it over the part surface, especially when reaching is required to access the defective portion of the part. The vibration of the sander is also known to cause vibration white finger [2] where blood vessels are damaged [3] resulting in poor blood flow primarily to the fingers, causing them to turn white, become numb, and in severe cases can cause muscular issues. To avoid these ergonomic injuries a method of sanding parts safely should be found, which is the focus of this thesis.

To mitigate against these ergonomic issues, several specialized tools have been developed. The first tool consists of a hand guided gantry system and a pneumatically controlled device designed to apply a constant and controllable downward force on the sander. While this

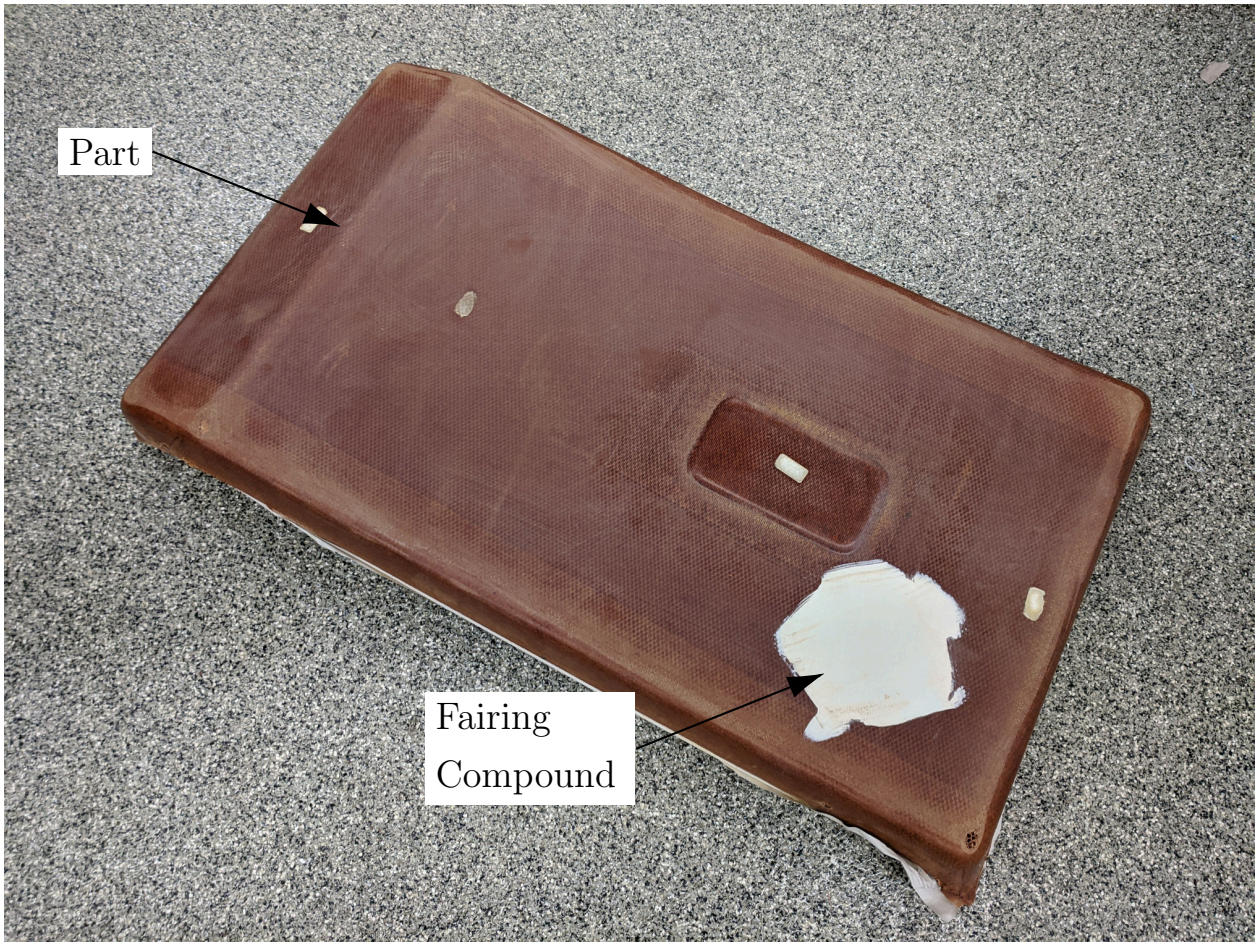

Figure 1.1: A typical part requiring sanding to remove the excess fairing compound applied to the site of a part defect.

tool successfully damps vibrations and reduces forces on the operator, it is of limited use because it only works on flat surfaces. Another tool which has been developed is a sander with a weight and a long handle. This provides many of the same benefits of the previous tool at a much lower cost; however, this tool only works for flat horizontal panels. Robotic sanding [4, 5] is an attractive option to mitigate against the ergonomic risks of hand sanding as it completely removes the operator from harmful forces and vibrations and is capable of sanding parts of arbitrary geometry. However, existing systems utilize a pre-planned path which is not easily compatible with this task since the fairing compound applied to the part, as shown in Fig. 1.1, has an unknown and non-constant thickness. Teleoperation can utilize the skill of existing mechanics to determine, in real time, the portions of the part surface where sanding is necessary to meet quality standards. Therefore, during teleoperation the velocity of the tool over the part surface is commanded in real time by the operator. Since this velocity is non-constant, a constant contact force would cause a varying depth of material to be removed, potentially leading to an inconsistently sanded part, which would not meet quality standards. While it would be possible for the operator to manually control the contact force to keep the depth of material removed consistent, this would likely be difficult because of the reduced sensory perception available during teleoperation. Therefore, the contact force should be automatically modulated to maintain a consistent depth of material removed. Teleoperation further allows the operator to compensate for differences in the distribution of material removal due to unmodeled effects.

While robotic systems with a pre-planned path are able to remove a spatially consistent depth of material [6], these methods are not compatible with teleoperation due to the robot path being inherently unknown a priori. A common method for removing a spatially consistent depth of material is to use a path that evenly covers the part surface, and to move along that path at a constant speed while removing material at a temporally constant rate. To ensure a temporally constant volume of material is removed, the contact force and speed of the abrasive against the part should both be kept constant. These quantities can also be time varying and kept in correct relation to each other to maintain a constant volumetric

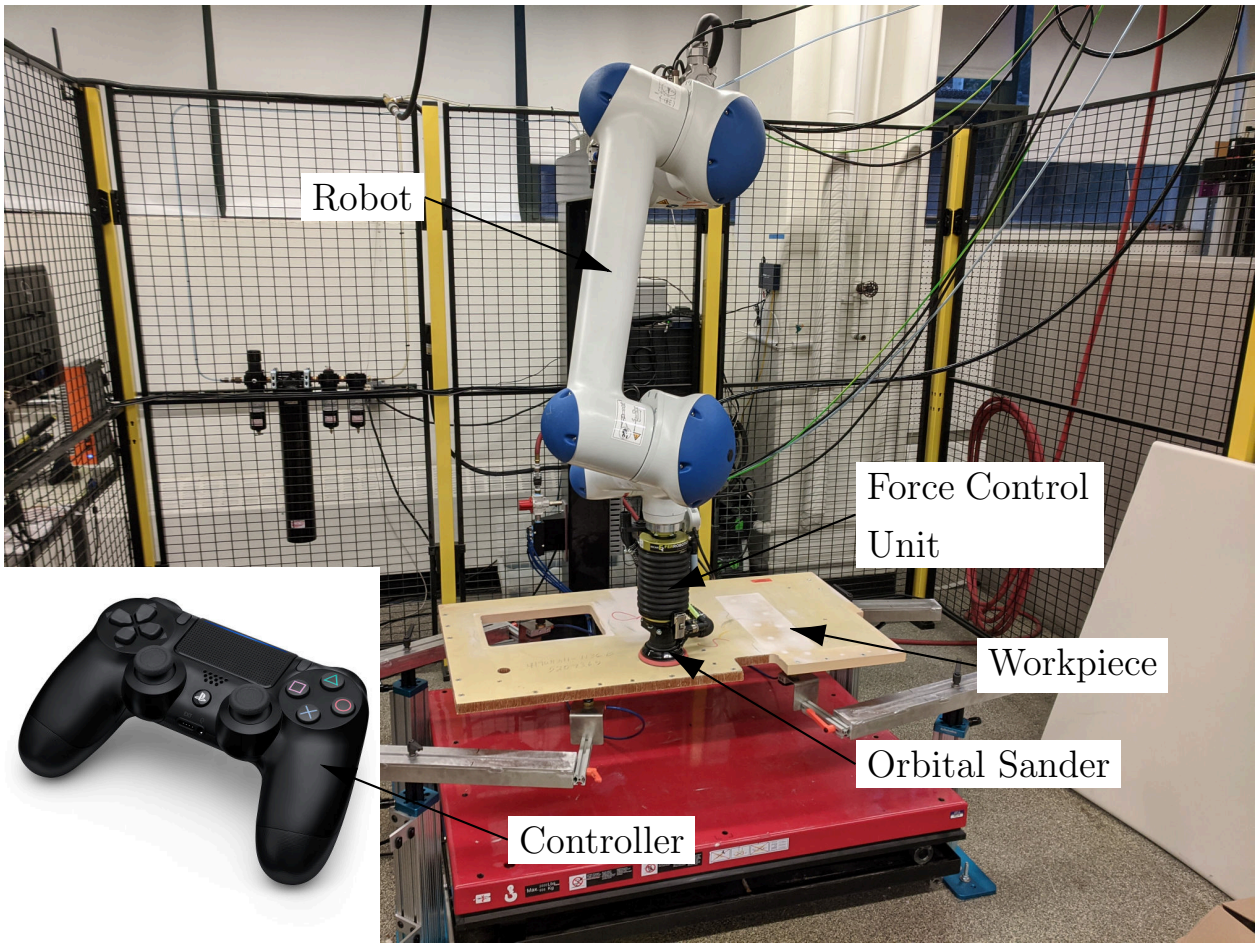

Figure 1.2: The robot sanding system consisting of a Yaskawa HC10 collaborative robot, FerRobotics ACF force control unit, Sioux orbital sander, and a Sony DualShock 4 game controller.

material removal rate. If the speed of the tool over the part surface is not constant, or other constraints of the previous method cannot be met, optimization techniques have been used to create a plan for removing a spatially consistent depth of material. However, with teleoperation neither of these approaches are applicable as the velocity is unknown a priori.

A robotic sanding system was built in the BARC lab for teleoperation which is shown in Fig. 1.2. This system consists of a Yaskawa Motoman HC10 collaborative robot for positioning the sanding tool. A FerRobotics ACF force control unit is used to apply the required force to the sanding tool. A Sioux orbital sander is then mounted on the end of the force control unit. An Intel RealSense L515 LIDAR depth camera is used to determine the geometry of parts placed in the workspace. Human operators can use a Sony DualShock 4 game controller as a human interface device to command the robot motion. Finally, a PC running Linux and ROS [7] is used to command the robot motion.

1.1 Problem Statement and Research Questions

Previous research has enabled the depth of material removed during abrasive surface finishing tasks to be controlled [6]. However, this research has assumed a known path and speed along the path. With a teleoperated robotic system, the path and speed along the path are not know a priori. Because of this, existing methods for controlling the depth of material removed cannot be used; therefore, a new method needs to be developed. My contributions are a method for controlling the depth of material removed during teleoperation on flat and convex surfaces and an analysis of its performance in different use cases to determine in what cases it will be useful to the operator. This contribution is broken into the following two questions:

Q1. How can the depth of material removal be controlled when the tool speed is not known a priori?

When sanding flat parts the depth of material removed can be kept spatially consistent by maintaining a constant temporal volumetric rate of material removal moving the

sander with a constant speed along a path which equally covers all areas of the part surface. A temporally constant volumetric rate of material removal can be trivially attained by keeping the contact force and tool abrasive speed constant. When these parameters cannot be held constant, optimization techniques can be utilized to create a spatially consistent depth of material removed. In this case the contact force or other parameters can be modulated to obtain a spatially consistent depth of material removed. With teleoperated robotic sanding the speed along the path is inherently unknown a priori, which invalidates the classic methods of controlling the depth of material removed. For this reason a new method of controlling the depth of material removed is needed which is applicable when the path and speed along the path is unknown, as is the case during teleoperation. The following steps will be used to develop and validate this new method of controlling the depth of material removed;

Q1.1. modeling the rate of material removal for flat and curved surfaces,

Q1.2. deriving a controller for the material removal rate by inverting the model, and

Q1.3. validating the model via simulation and experiment.

Q2. Does the proposed approach improve the performance of teleoperated robotic sanding?

While the previous question addressed the method for controlling the depth of material removed during teleoperated robotic sanding, it did not evaluate how useful the method is. A series of experiments are necessary to determine if the proposed method is advantageous in this use case. To determine the performance of the system with a human operator the experiments must include a human operator in the loop. The performance can then be measured by looking at different metrics including the surface height variation, part completion time, and the operators feelings about the proposed method. The following experiments and analysis will provide data and insights necessary for determining the effectiveness of the proposed method during teleoperation:

Control (Q1)			Performance (Q2)		
$f = \frac{2\bar{h}Rv_l}{E\omega_m k_p}$					
Model (Q1.1)	Control (Q1.2)	Validation (Q1.3)	Simulated (Q2.1)	Physical (Q2.2)	Analysis (Q2.3)
Chapter 3	Chapter 3	Chapter 4	Chapters 5 and 7	Chapter 6	Chapter 7

Figure 1.3: A graphical representation of the research questions and thesis organization.

Q2.1. run a sanding experiment with and without the proposed approach in a virtual environment on both flat and curved surfaces,

Q2.2. run the same experiment using physical robotic hardware, and

Q2.3. perform a comparative analysis of the results.

These research questions are summarized in Fig. 1.3.

1.2 Outline

This thesis is organized as follows, in Chapter 2 the relevant literature is covered. Then, in Chapter 3 the model and material removal rate controller is derived answering Q1.1 and Q1.2. Next, in Chapter 4 the proposed model and controller are validated as required by Q1.3. Afterwards, human robot interaction experiments using both a virtual environment and the physical robotic sanding system are designed and performed in Chapters 5, 6, and 7 to fulfill Q2.1 and Q2.2. Subsequently, an analysis comparing the results of the human robot interaction experiments is detailed in Chapter 7 answering Q2.3. Final analysis and conclusions along with possible future work is discussed in Chapter 8.

Chapter 2
LITERATURE REVIEW

While the literature on robotic sanding is limited, there are some notable publications. Poiree et al. [8] characterized the rate of material removal when using a random orbital sander on MDF. Using a different approach, Taylor et al. [9] and Saloni et al. [10] both quantified the material removal rate with different sanding parameters on wood including wood species, abrasive type, grit size, and pressure. Kabir et al. [11] continued this work by determining the minimum number of experiments to find an optimal set of sanding parameters. Huo et al. [12] created an automatic system for sanding parts on a belt sander; while Wen and Pagilla [4] created a robotic sanding system including force control, part scanning, and normalization. Finally, Maric et al. [13] designed a program by demonstration robotic sanding system. From this literature some aspects of the work of Wen and Pagilla [4] were utilized in designing the system for controlling the robot motion and the work of Poiree et al. [8] was used as a starting point for modeling the rate of material removal for this problem.

2.1 Material Removal Rate Modeling

In 1927 Frank W. Preston published an empirical formula for the rate of material removal in glass polishing machines [14]. This formula has since been applied in various abrasive material removal applications. In 1860 Theodore Reye derived a theoretical model of the wear parts experience when they slide against each other [15] and in 1953 John Frederick Archard published an identical model [16]. The empirically and theoretically derived models can be shown to be mathematically identical, therefore both of these models are an equally valid starting point for modeling the material removed on a part surface, and have previously been used for deriving material removal rate models [6, 17]. Poiree et al. [8] derived a model

from the Preston equation which takes into account the orbital and free rotating velocities of a random orbital sander where the velocity may not be constant at all points on the tool surface. Furthermore, various work has been performed to model the pressure distribution when polishing, which is especially important on non-flat surfaces. Tian et al. [18], Ren et al. [19], and Li et al. [20] used Hertzian contact mechanics [21] to estimate the polishing pressure distribution. Using a different approach, Tsai et al. [6] assumed a constant pressure distribution with a variable contact area. Feng et al. [22] and Wang et al. [23] used a pressure distribution model where the local pressure is linearly related to the local deformation of the sanding tool. Feng et al. [22] performed this work only for flat surfaces, while Wang et al. [23] included curved surfaces. Instead of deriving a pressure distribution model, Zhao et al. [24] and Xiao et al. [25] performed finite element modeling to check their respective pressure distribution models. Finally, avoiding modeling completely, Cheung et al. [26] used curved fitting methods to directly quantify the effects of curvature on the spatial distribution of material removed in jet polishing using experimental data.

These models typically provide a mass or volume rate of material removal. This material removal rate can then be integrated over a planned path to determine the spatial distribution of material removed. Alternatively, a small section of an arbitrary sanding path can be considered, and the depth of material removed can be calculated. Zhang et al. [27] considered a straight section of path, while Fan et al. [17, 28] considered a curved section of path. In this thesis the work of Poiree et al. [8] will be extended to model the depth of material removed on curved surfaces using methods similar to those of Tian et al. [18] and Tsai et al. [6] using the same pressure distribution model as Feng et al. [22] and Wang et al. [23] and integrating over a straight section of path like Zhang et al. [27].

2.2 Material Removal Rate Control

In 1977 Robert Jones published a paper [29] on Computer Controlled Optical Polishing (CCOS). In this technique, an optical lens is measured to determine the spatial distribution of glass that needs to be removed over its surface to create the desired shape. Next, the

"dwell time" at each point on the lens is determined. This "dwell time" is the amount of time the system should spend polishing a given area before moving to the next. The lens can then be re-measured and the process repeated. While this paper describes the basic method used, it does not give a thorough description of the dwell time calculation. There is a significant body of research dedicated to solving this dwell time calculation problem, such as the paper by Zhang et al. [30] which presents a linear algebra based method for determining dwell time or the paper by Tam et al. [31] which uses constrained optimization techniques.

Along with controlling dwell time, other control methods are possible. Due to the difficulty of directly sensing the rate of material removal, most material removal rate control systems operate by calculating a desired value for one term of a model with the other terms either measured or estimated. For example, the contact force that results in a given material removal rate can be calculated from the measured speed of the sanding tool abrasive against the part surface and an estimate of the part curvature. To estimate the part curvature point cloud data [32] or a NURBS surface [6] can be used. The robotic system can then use a feedback control loop to reach the calculated value, in this example contact force. Force control is the primary method of implementing a constant material removal rate system [6, 33]; however other terms can be controlled. For example, Xu et al. [34] modulated the speed of their polishing tool along a pre-planned path to keep a spatially consistent depth of material removal, and Ding et al. [35] controlled the rotational velocity of their polishing tool in order to control the material removal rate. As force control is the easiest to implement on the system described in the introduction (Chapter 1) it will be used. Furthermore, a method for controlling the depth of material removed when the speed of the robot along its path is unknown a priori will be derived, which is not possible with current methods.

2.3 Teleoperation

Some research in the area of teleoperation for robotic sanding, and similar processes, has already been completed. Nagata et al. have written several papers on using a joystick to teach a polishing operation to a robot [36, 37, 38]. There is also research on haptic control of abrasive surface finishing including Choo et al. [39] who created a haptically controlled grinding robot. Girbes-Juan et al. [40] similarly studied the effects of haptic control on a task designed to mimic abrasive surface treatment and included a learning framework to enable shared control while Enomoto et al. [41] used similar techniques to enable autonomous operation. There has also been some work on hand guiding of robots for finishing tasks. An impedance based method for hand guiding a sanding robot was designed by Maric et al. [13]. Similarly, Gaz et al. [42] and Solanes et al. [43] derived methods for maintaining normality and controlling force while allowing a robot to be manipulated by hand. As non-haptic teleoperation has not been proposed for real time non-teaching control of an abrasive surface treatment task, this thesis will explore a new method of teleoperation for abrasive material removal tasks.

2.4 Human Robot Interaction

Although there is no existing research analyzing the interaction between humans and sanding robots, there is a rich body of literature that can be used to help design experiments. Hoffman [44] evaluated the statistical significance of different questions for evaluating human robot interaction, and Owan [45] developed a human robot interaction experiment for evaluating a robotic system with shared autonomy. Both of these works provide insight into how to evaluate the users views on the operation of a robotic system. Furthermore, Steinfeld et al. [46] compiled a list of different metrics for human robot interaction. By drawing from both the works of Hoffman [44] and Steinfeld et al. [46] the quantitative and qualitative performance of the proposed control system can be evaluated.

Chapter 3

MATERIAL REMOVAL RATE MODELING AND CONTROL

Since existing methods of controlling the depth of material removed are not compatible with teleoperation due to the velocity being unknown a priori, a new method must be derived. This method will be derived by first modeling the depth of material removed on a surface of known shape then inverting the model to find the normal force required to remove a given depth of material. The model will be derived in two steps. The first step of the derivation is to form a general model applicable to any abrasive tool. This generic model will then be used to define a model applicable only to orbital sanders.

3.1 Assumptions

To make this problem tractable, a few simplifying assumptions are necessary. Although the tool may not be moving along a linear path, we will assume that the sander will be moving in a straight line for one full diameter and during this time it will remain normal to the part surface. It is also assumed that the contact force with the part, part curvature, abrasive speed, and linear velocity will remain constant as well. While these assumptions may not perfectly reflect the actual motion and parameters, they will allow a model to be derived which is computationally simple enough to be used for real-time control.

3.2 Model Derivation

The Preston equation [14],

$$\dot{h}(x,y) = k_p p(x,y) v(x,y), \tag{3.1}$$

relates the volumetric rate of material removal per unit area $\dot{h}(x,y)$ to the pressure applied to the abrasive surface $p(x,y)$ and the speed of the abrasive against the part $v(x,y)$ all at a

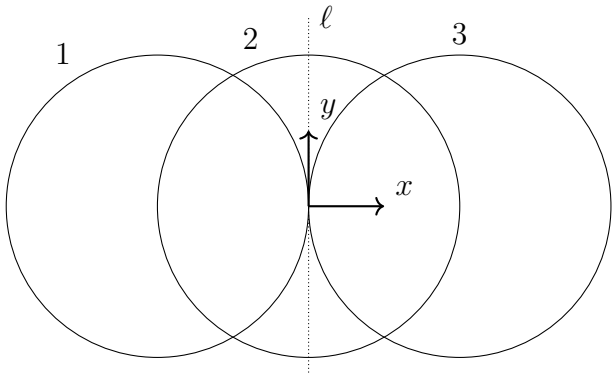

Figure 3.1: An arbitrarily shaped sander represented by circles 1, 2, and 3, moving over a line ℓ.

given (x, y) location using a constant[1] k_p. Using the SI system the variables can be assumed to have the following units, the rate of material removal per unit area $\dot{h}(x, y)$ has units $\frac{\mathrm{m}}{\mathrm{s}}$, the pressure $p(x, y)$ has units $\frac{\mathrm{N}}{\mathrm{m}^2}$, the abrasive speed $v(x, y)$ has units $\frac{\mathrm{m}}{\mathrm{s}}$, and the constant k_p has units $\frac{\mathrm{ms}^2}{\mathrm{kg}}$. From eq. 3.1 a model of the depth of material removed can be derived for which the velocity at which the sander is moving does not need to be known a priori. As we are assuming the sander is moving in a straight line we can model the depth of material removed on a line ℓ perpendicular to the direction of travel. This is shown in Fig. 3.1 where an arbitrarily shaped sander assumed to have a length L in the x direction and a width w in the y direction moves from the location denoted by circle 1 to the location denoted by circle 3, completely passing over line ℓ. As the sander moves over this line, it removes material proportionally to the pressure applied and the speed of the abrasive against the part as shown in eq. 3.1. From this information, the depth of material removed at any point $h(y)$, and the average depth of material removed on line ℓ, $\bar{h}$, can be found. First, the depth of material removed $h(y)$ at a given location y on line ℓ can be found by integrating eq. 3.1 in time as the sander moves with speed v_l across line ℓ, in this case assumed to be the x

[1]This constant must be found experimentally [47].

direction. At time t, the sander is then assumed to be in the position $x = v_l t$,

$$h(y) = \int_{-\frac{L}{2v_l}}^{\frac{L}{2v_l}} \dot{h}(v_l t, y)\, dt \tag{3.2}$$

$$= k_p \int_{-\frac{L}{2v_l}}^{\frac{L}{2v_l}} p(v_l t, y) v(v_l t, y)\, dt, \tag{3.3}$$

where $h(y)$ is the depth of material removed at y on line ℓ. Using u-substitution with $x = v_l t$ eq. 3.3 can be simplified to,

$$h(y) = \frac{k_p}{v_l} \int_{\frac{-L}{2}}^{\frac{L}{2}} p(x, y) v(x, y)\, dx, \tag{3.4}$$

where the limits are $\frac{-L}{2}$ to $\frac{L}{2}$ which is the distance required for the sander to completely cross the line ℓ. To control the material removal process a single value is of more use than a function. Therefore, the average depth of material removed on line ℓ can be calculated,

$$\bar{h} = \frac{1}{w} \int_{\frac{-w}{2}}^{\frac{w}{2}} h(y)\, dy \tag{3.5}$$

$$= \frac{k_p}{w v_l} \int_{\frac{-L}{2}}^{\frac{L}{2}} \int_{\frac{-w}{2}}^{\frac{w}{2}} p(x, y) v(x, y)\, dx\, dy, \tag{3.6}$$

where the sander width w is the distance over which the depth of material removed is averaged. This equation can be transformed from a double integral to an area integral over the abrasive surface A,

$$\bar{h} = \frac{k_p}{w v_l} \iint_A p(x, y) v(x, y)\, dA, \tag{3.7}$$

where w is the width of material removed which is the distance on line ℓ in Fig. 3.1 where material is removed. This allows the average depth of material removed on line ℓ, $\bar{h}$, to be calculated for abrasive tools of arbitrary shape.

3.3 Application to a Random Orbital Sander

As the robotic system described in Chapter 1 includes an orbital sander, the generic model derived in the previous section should be further specified to accurately model the velocity

of the sanding abrasive against the part. Random orbital sanders have both a driven orbital motion and a freely rotating pad as shown in Fig. 3.2. The driven orbital motion with rotational velocity ω_m moves the center of the sanding pad in an eccentric orbit, while the pad is free to rotate about its center with rotational velocity ω_p. Furthermore, the entire sander is moved along the path at a velocity v_l. To determine a model for the speed of a random orbital sander's abrasive against the part surface, a stationary sander is examined, then linear motion is added.

3.3.1 Stationary Sander

Poiree, et al. [8] studied the motion of a stationary orbital sander and given a point on a stationary orbital sander at a radius r from the center of the pad as shown in figs. 3.1 and 3.2, the speed of the abrasive against the part $v_s(r,t)$ at time t is,

$$v_s(r,t) = \sqrt{r^2\omega_p^2 + E^2\omega_m^2 + 2rE\omega_p\omega_m \cos\left(\omega_p - \omega_m\right) t}, \tag{3.8}$$

where, E is the eccentricity of the orbital motion defined in Fig. 3.2, ω_m is the rotational speed of the orbital motion, and ω_p is the rotational speed of the pad. Poiree, et al. [8] also found that the rotational speed of the orbiting motion tends to be substantially higher than the rotational speed of the pad. For example, a sander with a radius of $R = 44$ mm and an eccentricity of $E = 5$ mm running at an orbital speed of $\omega_m = 5946$ RPM and a rotational speed of $\omega_p = 211$ RPM, as measured by Poiree, et al. [8], will produce only a 5% error if the rotational speed of the pad is neglected, $\omega_p = 0$. Therefore, the equation for the speed of the abrasive against the part for a stationary sander can be simplified to,

$$v_s = E\omega_m, \tag{3.9}$$

with only a small decrease in accuracy.

3.3.2 Moving Sander

The speed at which a sander is moved across the part v_l also influences the total speed of the abrasive $v(x,y)$ used in eq. 3.7. In eq. 3.9 the speed of the abrasive against the part is

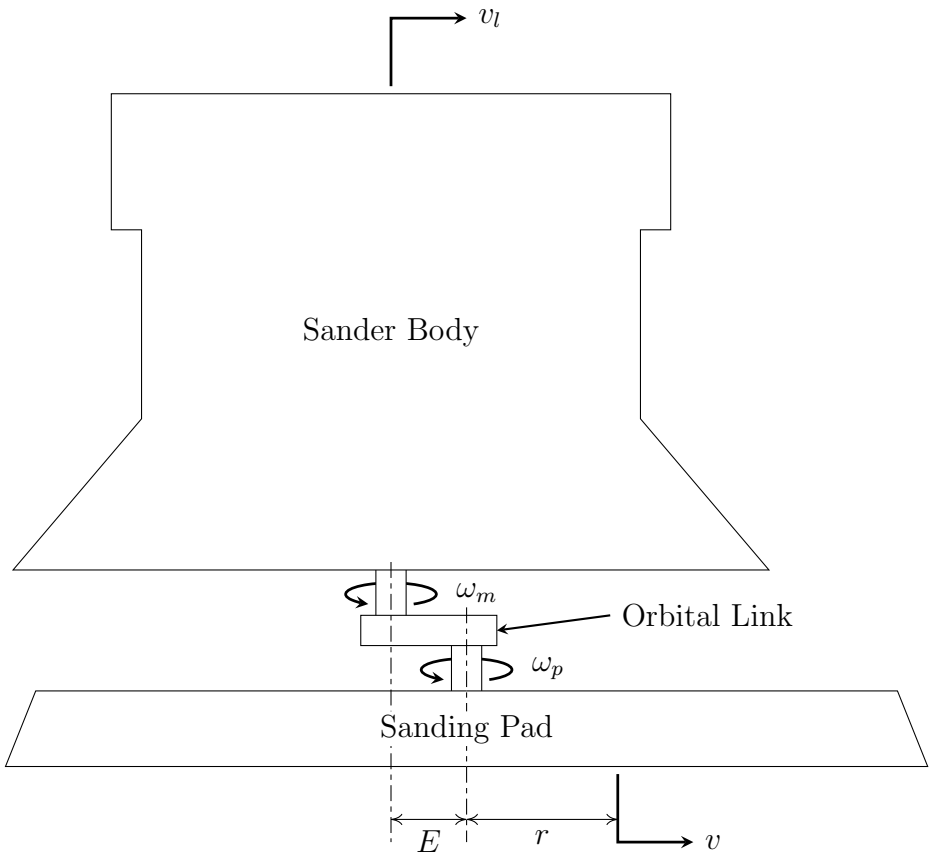

Figure 3.2: A diagram of the motion of the sander including the linear velocity the sander body is moved by the robot v_l, the motor driven shaft with rotational velocity ω_m, the orbital link with an offset distance of E, the free rotating shaft with a rotational velocity ω_p, and the total velocity v of a point a distance r away from the center of the sanding pad.

constant; however, its direction is not. The velocity of the sander modeled in eq. 3.9 is,

$$\vec{v}_s(t) = \begin{bmatrix} E\omega_m \sin \omega_m t \\ E\omega_m \cos \omega_m t \end{bmatrix}, \tag{3.10}$$

where $\vec{v}_s$ is the velocity corresponding to the simplified stationary sander speed in eq 3.9. Using eq. 3.10 and the linear speed v_l an expression for the total velocity of the abrasive against the part can be found,

$$\vec{v}(t) = \vec{v}_s(t) + \vec{v}_l, \tag{3.11}$$

where $\vec{v}$ is the total abrasive velocity and $\vec{v}_l = [v_l \ 0]^T$. By integrating eq. 3.11 over one orbit of the sander the average speed of the abrasive against the part can be found,

$$v(\omega_m, v_l) = \frac{\omega_m}{2\pi} \int_0^{\frac{2\pi}{\omega_m}} \|\vec{v}(t)\| \, dt \tag{3.12}$$

$$= \frac{|v_l - \omega_m E| \, \mathsf{E}(-\frac{4\omega_m E v_l}{(v_l - \omega_m E)^2}) + |\omega_m E + v_l| \, \mathsf{E}(\frac{4\omega_m E v_l}{(\omega_m E + v_l)^2})}{\pi}, \tag{3.13}$$

where $v(\omega_m, v_l)$ is the average speed given the orbital rotational speed ω_m and linear speed v_l, and $\mathsf{E}(m)$ is the complete elliptic integral of the second kind. However, assuming $v_l = 0$ in this equation produces only a 0.1% error under normal operating conditions [47]. This allows eq. 3.9 to be directly used. Substituting $v(x, y) = E\omega_m$ into eq. 3.7 leaves the following equation,

$$\bar{h} = \frac{k_p E \omega_m}{w v_l} \iint_A p(x, y) \, dA, \tag{3.14}$$

where only the pressure distribution must be integrated. However, since the double integral of the pressure distribution $p(x, y)$ over the contact area A is by definition the contact force f, this equation can be simplified to,

$$\bar{h} = \frac{k_p E \omega_m f}{w v_l}, \tag{3.15}$$

where no integration is necessary. Furthermore on a flat surface the width $w = 2R$ resulting in the equation,

$$\bar{h} = \frac{k_p E \omega_m f}{2 R v_l}, \tag{3.16}$$

for flat surfaces. While the equation for flat surfaces is complete, on contoured surfaces the contact width w still must be found.

3.4 Sander Pressure Distribution

While through the work of the previous section the need for defining the pressure distribution may no longer be apparent, it is necessary for determining the material removal width w in eq. 3.15. This pressure distribution is derived by first modeling the part surface then utilizing the model to determine the pressure distribution. A differentiable surface can be characterized by its principal curvatures k_1 and k_2 where $k_1 \geq k_2$. To model the pressure distribution on non-flat surfaces these surfaces are first approximated as a (possibly hyperbolic) paraboloid,

$$z = \frac{k_2}{2}x^2 + \frac{k_1}{2}y^2, \tag{3.17}$$

where x, y, and z compose an arbitrary Cartesian coordinates system. It can easily be verified that this paraboloid has principal curvatures k_2 in the x direction and k_1 in the y direction. This representation was chosen because of its simplicity and flexibility to model both convex and concave surfaces as well as saddle points.

While Hertzian contact theory [21] would provide the best accuracy for the pressure distribution on non-flat surfaces, closed form solutions have not been derived for paraboloids via classical methods or dimensional reduction [48]. For this reason the method of dimensional reduction is used, without modification to the surface shape, leading to the equation,

$$p(x, y) = \mathscr{E}\frac{\delta z(x, y)}{\tau}, \tag{3.18}$$

where $\delta z(x, y)$ is the distance the part is pressing into the tool at a given location, $\mathscr{E}$ is the Young's modulus of the tool, and τ is the thickness of the tool. This linear approximation is the same model as used by Feng et al. [22] and Wang et al. [23].

The pressure distribution can now be determined by combining eqs. 3.17 and 3.18 resulting in the equation,

$$p(x, y) = \frac{\mathscr{E}}{\tau}\left(d - \frac{k_2}{2}x^2 - \frac{k_1}{2}y^2\right), \tag{3.19}$$

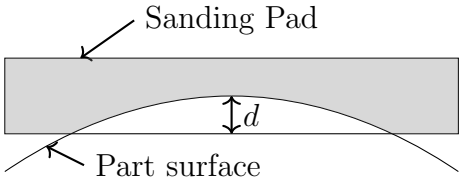

Figure 3.3: A side view of the sanding pad on a parabolic surface with the max pad compression d shown.

where a constant d is added to eq. 3.17 to set the contact force f. This pressure distribution can now be used for determining the contact width and by integrating over the contact area provide a relationship between the contact force f and max pad compression d.

3.5 Sander Contact Area

Given different combinations of k_1 and k_2, there are 7 different contact patterns that can result; however, only the three cases associated with convex surfaces are derived here. Each contact pattern needs a unique equation for the contact area A to be found, which results in a different relation between the contact force f and the max displacement d shown in Fig. 3.3. From this information a test to determine if a given contact pattern is valid can be derived. Now, the average depth of material removed $\bar{h}$ can be determined by first finding the contact width, then using eq. 3.15.

3.5.1 Unconstrained Contact

In unconstrained contact, the contact area naturally fits within the bounds of the sanding pad. Solving the pressure distribution defined in eq. 3.19 for $p = 0$ lets us find the contact area A,

$$1 \geq \frac{k_2}{2d}x^2 + \frac{k_1}{2d}y^2, \tag{3.20}$$

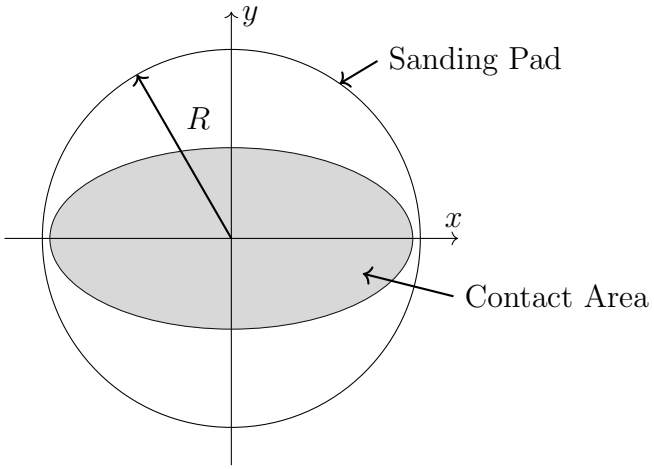

Figure 3.4: The unconstrained contact area showing the sanding pad of radius R and the contact area A.

which is in the shape of an ellipse. Given the contact area equation, the length of the semi-major axis can be seen to be $\sqrt{\frac{2d}{k_2}}$. Therefore, as long as,

$$R \geq \sqrt{\frac{2d}{k_2}}, \tag{3.21}$$

the contact area is unconstrained. Since the contact area is ellipsoidal the width of material removal varies with the direction of travel. To determine this width the y axis bounds of an ellipse centered at the origin and rotated to the required angle can be used. The equation for the y axis bounds of an ellipse is [49],

$$y_{bb} = \pm\sqrt{a^2 \sin^2 \phi + b^2 \cos^2 \phi)}, \tag{3.22}$$

where a and b are from the standard form of an ellipse,

$$1 = \frac{x^2}{a^2} + \frac{y^2}{b^2}, \tag{3.23}$$

and ϕ is the angle of rotation of the ellipse to align it to the direction of travel where $\phi = 0$ denotes travel in the positive x direction. Therefore, from eq. 3.20 the variables $a = \sqrt{\frac{2d}{k_2}}$

and $b = \sqrt{\frac{2d}{k_1}}$, so the width w is twice the y bound y_{bb} resulting in the equation,

$$w = 2y_{bb} \tag{3.24}$$

$$= 2\sqrt{2d\left(\frac{\sin^2\phi}{k_2} + \frac{\cos^2\phi}{k_1}\right)}, \tag{3.25}$$

utilizing eq. 3.22. Substituting this equation into eq. 3.15 results in the formula,

$$\bar{h} = \frac{k_p E \omega_m f}{v_l \sqrt{d} w_s}, \tag{3.26}$$

where,

$$w_s = 2\sqrt{2\left(\frac{\sin^2\phi}{k_2} + \frac{\cos^2\phi}{k_1}\right)}. \tag{3.27}$$

is constant which can be calculated for a given surface shape and direction of travel.

From eq. 3.19 it can be seen that there is a relationship between the contact force f and the max compression distance d. This relationship is useful since eq. 3.26 includes both the contact force f and the max compression distance d leading to a system of equations. To find the relationship the pressure distribution defined in eq. 3.19 can be integrated over the contact area,

$$f = \frac{\mathscr{E}}{\tau} \iint_A d - \frac{k_2}{2}x^2 - \frac{k_1}{2}y^2 \, dA, \tag{3.28}$$

which is equivalent to the volume of a paraboloid of the form,

$$1 = \frac{x^2}{za^2} + \frac{y^2}{zb^2}, \tag{3.29}$$

with $a = \sqrt{\frac{2\tau}{\mathscr{E}k_2}}$, $b = \sqrt{\frac{2\tau}{\mathscr{E}k_1}}$, and $h = \frac{\mathscr{E}}{\tau}d$. Using the paraboloid volume equation from Appendix C the relationship between the contact force f and max compression distance d can be found,

$$f = \frac{\mathscr{E}\pi d^2}{\tau\sqrt{k_1 k_2}}, \tag{3.30}$$

which can be used to solve eq. 3.26 to only depend on d. Now, eq. 3.30 can be substituted into eq. 3.26 resulting in the equation,

$$\bar{h} = \frac{k_p E \omega_m \mathscr{E}\pi d^{\frac{3}{2}}}{v_l w_s \tau\sqrt{k_1 k_2}}, \tag{3.31}$$

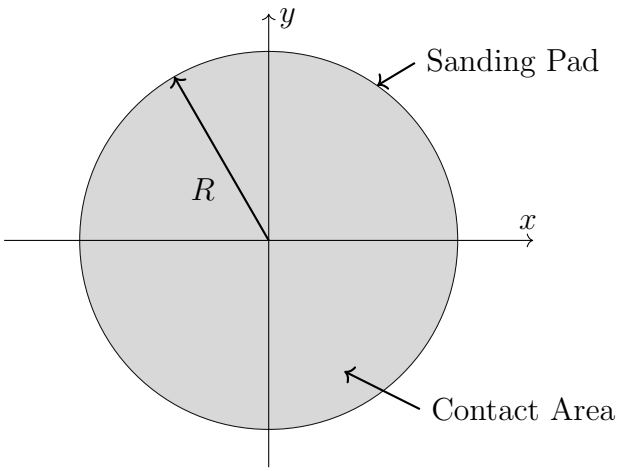

Figure 3.5: The fully constrained contact area showing the sanding pad of radius R and the contact area A completely filling the pad.

which allows the average depth of material removed to be calculated for a given pad compression distance d and other parameters. These equations allow the average depth of material removed to be calculated when the contact area naturally fits within the bounds of the sanding pad.

3.5.2 Fully Constrained Contact

In the fully constrained contact area case, the contact area is bounded by the edge of the sanding pad as shown in Fig. 3.5. Given an infinitely large sanding pad the contact area would be the ellipse defined in eq. 3.20; however, given a finite size round sanding pad of radius R for the contact area to fill the pad the condition,

$$R \leq \sqrt{\frac{2d}{k_1}}, \tag{3.32}$$

must be true. Since the material removal width w is again $w = 2R$, the equation for the average material removal depth $\bar{h}$ on flat surfaces eq. 3.16 is also applicable here. However, as eq. 3.16 is based on the contact force f and the constraint eq. 3.32 uses the max pad

compression distance d, the relationship between f and d should be found by again integrating the pressure distribution over the contact area, now a circle of radius R, as defined in eq. 3.28. This integral can be transformed to polar coordinates with $x = r\cos\theta$ and $y = r\sin\theta$ and solved,

$$f = \frac{\mathscr{E}}{\tau}\int_0^{2\pi}\int_0^R \left(d - \frac{k_2}{2}r^2\cos^2\theta - \frac{k_1}{2}r^2\sin^2\theta\right) r\,dr\,d\theta \tag{3.33}$$

$$= \frac{\mathscr{E}}{\tau}\int_0^{2\pi} d\frac{R^2}{2} - \frac{k_2}{8}R^4\cos^2\theta - \frac{k_1}{8}R^4\sin^2\theta\,d\theta \tag{3.34}$$

$$= \frac{\mathscr{E}}{\tau}\left(dR^2\pi - \frac{k_2}{16}R^4\left(2\pi + \sin 2\pi\cos 2\pi\right) - \frac{k_1}{16}R^4\left(2\pi + \sin 2\pi\cos 2\pi\right)\right) \tag{3.35}$$

$$= \frac{\mathscr{E}\pi}{\tau}\left(dR^2 - \frac{R^4}{8}\left(k_1 + k_2\right)\right), \tag{3.36}$$

resulting in a relationship between the max pad compression distance d and the contact force f. Using these equations when the contact area is the whole surface of the sanding pad the average depth of material removed can be determined.

3.5.3 Partially Constrained Contact

In the partially constrained contact area case, the contact area is constrained by the edge of the pad in some areas, and by the pressure distribution decreasing to zero in others as shown in Fig. 3.6. As this is the remaining contact area case for convex surfaces, it is valid for all convex surfaces ($k_1 > 0$ and $k_2 > 0$) that are not fully constrained or unconstrained. The contact force f is used in eq. 3.15 which defines the average depth of material removed. This equation also requires the material removal width w which in this case may depend on the value of d. Since the contact area is a combination of the contact area from the unconstrained and fully constrained cases, the material removal width w is similarly the minimum of the contact area in the unconstrained case defined in eq. 3.25 and the fully constrained case, $w = 2R$. The relationship between the contact force f and max pad compression d should again be determined using eq. 3.28. As the pressure distribution is symmetric about both the x and y axes the force in the first quadrant can be calculated and quadrupled to determine

the contact force f. The force from the sector of the contact area from 0 to θ as shown in Fig. 3.6 can be determined using eq. 3.28 converted to polar form as in Sec. 3.5.2 and evaluated from 0 to θ,

$$f_1 = \frac{\mathscr{E}}{\tau}\int_0^{\theta}\int_0^{R}\left(d - \frac{k_2}{2}r^2\cos^2\theta - \frac{k_1}{2}r^2\sin^2\theta\right) r\,dr\,d\theta \tag{3.37}$$

$$= \frac{\mathscr{E}}{\tau}\int_0^{\theta} d\frac{R^2}{2} - \frac{k_2}{8}R^4\cos^2\theta - \frac{k_1}{8}R^4\sin^2\theta\,d\theta \tag{3.38}$$

$$= \frac{\mathscr{E}}{\tau}\left(\frac{dR^2}{2}\theta - \frac{R^4}{16}k_2\left(\theta + \frac{\sin(2\theta)}{2}\right) - \frac{R^4}{16}k_1\left(\theta - \frac{\sin(2\theta)}{2}\right)\right), \tag{3.39}$$

which can be used in determining the total force f. The force from the rest of the first quadrant of the pressure distribution is from the sector of the contact area from θ to $\frac{\pi}{2}$ can be found using the equation for a sector of a paraboloid from Appendix D. As in Sec. 3.5.1 $a = \sqrt{\frac{2\tau}{\mathscr{E}k_2}}$, $b = \sqrt{\frac{2\tau}{\mathscr{E}k_1}}$, and $h = \frac{\mathscr{E}}{\tau}d$. Using eq. D.5 the contact force resulting from the pressure in the sector from θ to $\frac{\pi}{2}$ can be found,

$$f_2 = \frac{\mathscr{E}d^2}{2\tau\sqrt{k_1k_2}}\left(\frac{\pi}{2} - \tan^{-1}\left(\sqrt{\frac{k_1}{k_2}}\tan(\theta)\right)\right), \tag{3.40}$$

which can also be used in determining the total force f. Using the equations for f_1 and f_2 the total contact force can be found by calculating $f = 4(f_1 + f_2)$ resulting in the equation,

$$\begin{aligned} f = \frac{\mathscr{E}}{\tau}\Bigg(&\frac{2d^2}{\sqrt{k_1k_2}}\left(\frac{\pi}{2} - \tan^{-1}\left(\sqrt{\frac{k_1}{k_2}}\tan(\theta)\right)\right) \\ &+ 2dR^2\theta - \frac{R^4}{4}k_2\left(\theta + \frac{\sin(2\theta)}{2}\right) - \frac{R^4}{4}k_1\left(\theta - \frac{\sin(2\theta)}{2}\right)\Bigg), \end{aligned} \tag{3.41}$$

which relates the contact force f to the max pad displacement d. To find the value of θ for this equation, we can solve the polar form of the contact area ellipse from the unconstrained case defined in eq. 3.20 for the angle at which it equals the sanding pad radius. The polar

form of eq. 3.20 is,

$$R = \sqrt{\frac{2d}{k_2 \cos^2\theta + k_1 \sin^2\theta}} \tag{3.42}$$

$$\frac{2d}{R^2} = k_2 \cos^2\theta + k_1 \sin^2\theta \tag{3.43}$$

$$\theta = \text{atan2}\left(\pm\frac{\sqrt{k_2 - \frac{2d}{R^2}}}{\sqrt{k_1 - k_2}}, \pm\frac{\sqrt{\frac{2d}{R^2} - k_1}}{\sqrt{k_1 - k_2}}\right) + 2n\pi, \tag{3.44}$$

where n is an integer. Because $0 \leq \theta \leq \frac{\pi}{2}$, the sign of both arguments to atan2 should be positive, and n can be assumed to be zero. Furthermore, the only time $k_1 - k_2$ can equal zero is when $k_1 = k_2$. In this case the pressure distribution would be either unconstrained of fully constrained. Also, the numerators of both arguments cannot equal zero, because they would fulfill the requirements to be unconstrained or fully constrained in eqs. 3.21 and 3.32 respectively. Therefore, this equation can safely be rewritten as,

$$\theta = \tan^{-1}\left(\sqrt{\frac{R^2 k_2 - 2d}{2d - R^2 k_1}}\right), \tag{3.45}$$

since the numerator and denominator cannot be zero, and $0 \leq \theta \leq \frac{\pi}{2}$. With the derived equations the average depth of material removed can be determined when the contact area is a hybrid of the previous two.

3.6 Material Removal Rate Control

To allow the depth of material removed to be controlled, the models derived in this chapter must be inverted, so the contact force f can be found for a desired average depth of material removed $\bar{h}$. The desired contact force f can then be fed into a closed loop force control system for accurate force control. For flat surfaces eq. 3.16 can be trivially inverted resulting in the equation,

$$f = \frac{2\bar{h} R v_l}{E \omega_m k_p}, \tag{3.46}$$

which can directly be used for determining the contact force when sanding flat surfaces. For convex surfaces more steps are necessary.

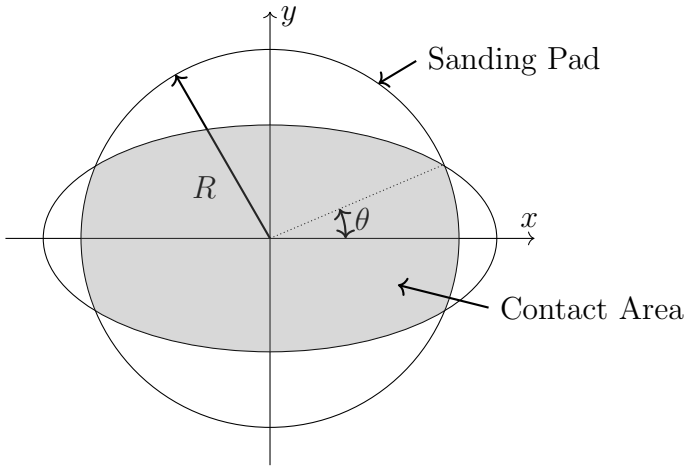

Figure 3.6: The partially constrained contact area showing the edge of the sanding pad with radius R, the shaded contact area A, and the transition angle θ.

3.6.1 Unconstrained Contact

If the contact area is unconstrained the contact force can be calculated by first determining w_s using eq. 3.27. The value of d can then be found by using eq. 3.15 which must be inverted for this purpose,

$$d = \left(\frac{\bar{h} w_s v_l \tau \sqrt{k_1 k_2}}{E \omega_m \mathscr{E} \pi k_p} \right)^{\frac{2}{3}}, \tag{3.47}$$

which allows d to be calculated from the average depth of material removed $\bar{h}$. Finally, the contact force can be found from the calculated max pad compression d using eq. 3.30.

3.6.2 Fully Constrained Contact

When the contact area is fully constrained the contact force can be determined using the same equation used for finding the contact force for flat surfaces eq. 3.46, since the material removal width is the same. To check if the fully constrained case is valid the constraint defined in eq. 3.32 is used; however, the value of d is needed to do this. To find the value of

d eq. 3.36 can be inverted,

$$d = \frac{f\tau}{\mathscr{E}\pi R^2} + \frac{R^2}{8}\left(k_1 + k_2\right), \tag{3.48}$$

this allows d to be found from the contact force f. Using this equation the contact force f for a given average material removal depth $\bar{h}$ can be calculated and a check can be performed to ensure this is the correct contact area case.

3.6.3 Partially Constrained Contact

The particularly constrained contact area is a hybrid of the previous two contact areas. This leads to a complex relationship between the contact force f and the mean depth of material removed $\bar{h}$. While the mean depth of material removed $\bar{h}$ can be determined from the contact force f using the equations derived in Sec. 3.5.3, when attempting the opposite, determining the contact force f from the average depth of material removed $\bar{h}$, a closed form solution is not available. Therefore the solution must be found numerically. This can be done by solving the optimization problem,

$$\min_d \ \left|\bar{h}_d - \bar{h}(d)\right|, \tag{3.49}$$

where $\bar{h}_d$ is the desired depth of material to remove, $\bar{h}(d)$ is the depth of material removed defined in eq. 3.15, where the value of d is required for calculating the contact force using eq. 3.41 and the material removal width w as described in Sec. 3.5.3. After the optimal value of d is found, eq. 3.41 can be used again to determine the correct contact force.

3.7 Conclusion

These equations allow the average depth of material removed to be controlled on convex surfaces when the velocity is unknown a priori. The equations are summarized in Fig. 3.7 which presents a method for determining the correct contact area and contact force when the principal curvatures of the surface are known. An implementation of this method is also presented in Appendix E.

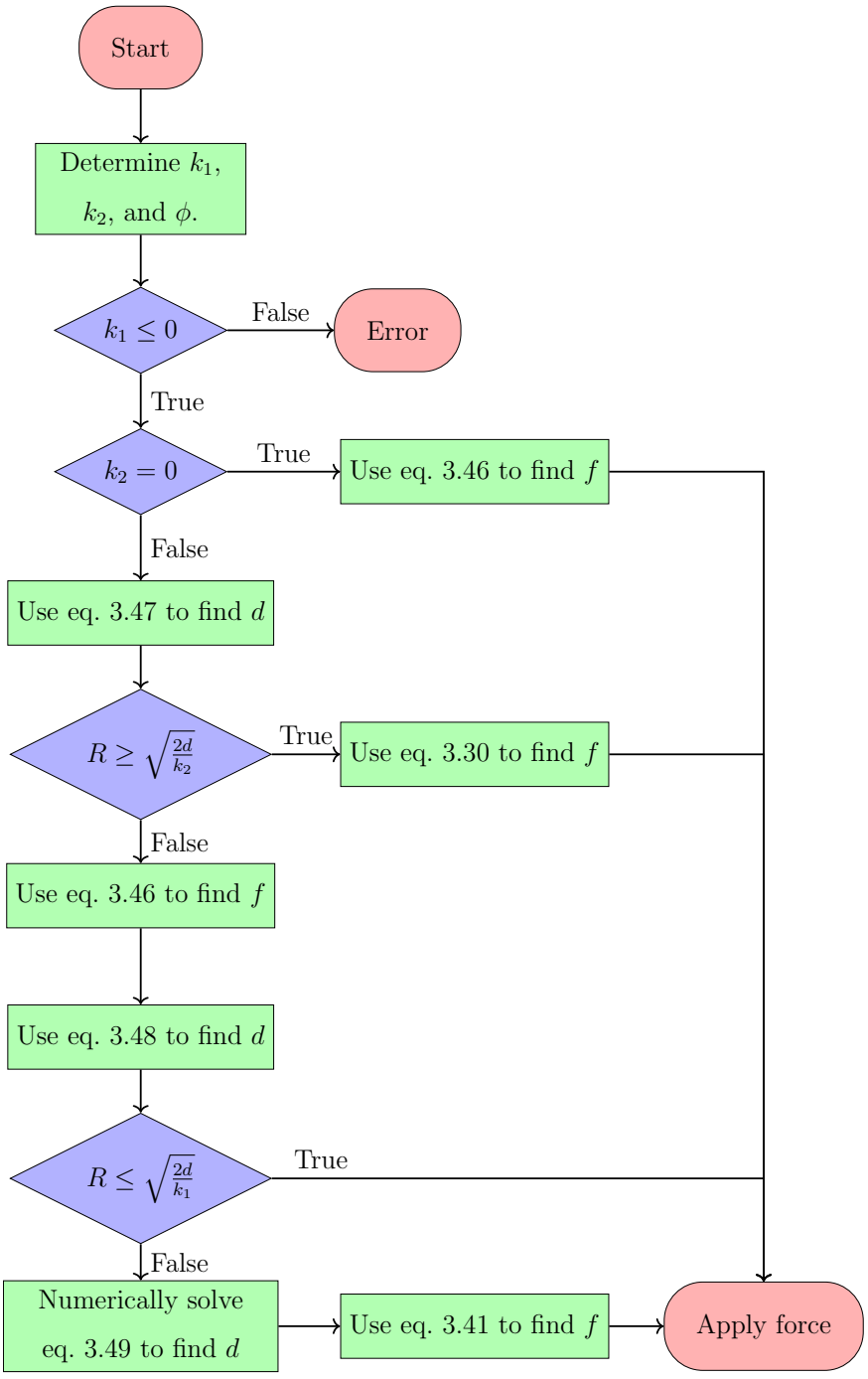

Figure 3.7: A flowchart showing how to control the depth of material removed for flat and convex surfaces.

Chapter 4
CONTROLLER VALIDATION

To ensure that the proposed controller is working correctly it must be validated. This validation will be performed using a series of simulated tests and physical experiments. In both cases a sander is moved back and forth on a linear path with a sinusoidally varying position. As the speed of the sander along the path is non-constant, a constant contact force will result in a spatially non-constant depth of material removed. However, with the controller derived in Chapter 3, the depth of material removed should be spatially consistent.

For these validation tests, both numerical simulations and the robotic sanding system in the BARC lab were used. This system includes an orbital sander with a 4.7 mm eccentricity assumed to be driven at 350 $\frac{\text{rad}}{\text{s}}$ during simulations, but measured in real time on the robotic system. The robot moves this sander along the sinusoidal path in the x axis with a period of 4 seconds. In the simulations, the Preston Equation [14] is used to estimate the material removed on the part surface, and the Preston coefficient is assumed to be $k_p = 1.362 \times 10^{-9}$ $\frac{\text{ms}^2}{\text{kg}}$ as estimated in a previous project [47]. When using the robotic sanding system, the test article is built from two different colored layers of 3 mil PVC thermally welded together. When sanded, this two layer part is appears similar to a heatmap, showing where sanding took place. For each part shape, two tests are performed, one with a constant contact force, and a second with the material removal depth control method derived in Chapter 3. We will begin with the flat test article.

4.1 Flat Part

When testing the controller on a flat part, the test article size was chosen to be approximately 300 mm long which allows for a motion amplitude of 104 mm. A sanding pad 88 mm in

diameter was used. Therefore, the test article was constructed to a width of 90 mm. This experiment was both simulated, and performed on the robotic sanding system.

4.1.1 Simulation

The material removed via sanding can be numerically simulated. As the part is flat and the sander is assumed to be normal to the surface, the pressure distribution is constant across the sanding pad. Running this simulation results in the heatmap of the spatial distribution of material removed shown in Fig. 4.1. In this figure the consistent depth of material removed in the center section of the part as compared to the part sanded with a constant contact force can be seen in Fig. 4.2. A comparison of the depth of material removed along the centerline ($y = 0$) of the two flat parts is shown in Fig. 4.3. The lesser amounts of material removed at the ends of the sander travel are due to the assumption that the sander will fully pass over a given line not being valid at the ends. Furthermore with constant force control the depth of material removed in the center section of the part is non-constant, unlike when the proposed depth control method is used. To compare the results from force and depth control the amount of material removed on the centerline of the part ($y = 0$) can be used. From these measurement the section of the part which the center of the sander completely passes over (ignoring one radius of the sanding pad at each end) will be evaluated to avoid the areas at the end where less material is removed. This data is normalized so the maximum depth of material removed is 1. Then to quantify this comparison, the RMS variation from the mean depth of material removed is calculated using the equation,

$$\sqrt{\text{mean}((\tilde{h}(x) - \text{mean}(\tilde{h}(x)))^2)}, \tag{4.1}$$

where $\tilde{h}(x)$ is the normalized depth of material removed along the centerline of the part ($y = 0$). Using this equation the proposed material removal depth control method reduces the variation by 30.4% versus a constant contact force as shown in Table 4.1. The same test can now be performed on the robotic sanding system.

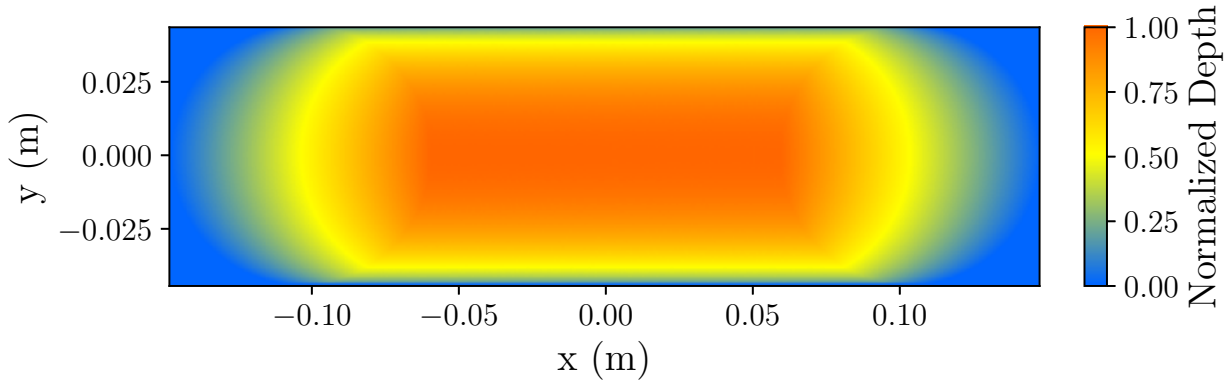

Figure 4.1: The depth of material removed on the surface of a flat part when the sander is moved over the part with a sinusoidally varying position and the contact force is controlled with the proposed method showing the consistent depth of material removed in the center section of the part.

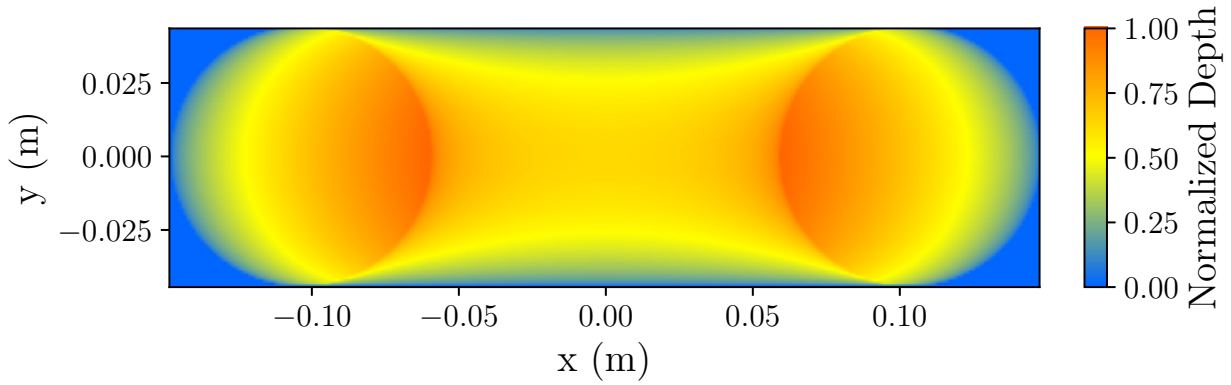

Figure 4.2: The depth of material removed on the surface of a flat part when the sander is moved over the part with a sinusoidally varying position and the contact force is constant showing the varying depth of material removed over the part surface.

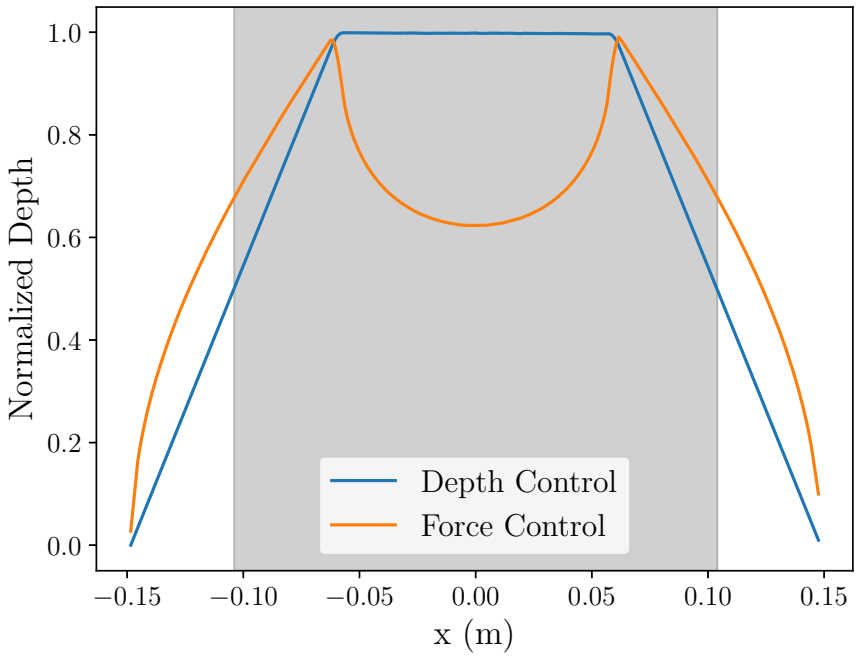

Figure 4.3: The depth of material removed on the centerline ($y = 0$) of the flat test part showing the constant depth of material removed in the center section of the test using the proposed material removal depth control method and the area used for calculation of the RMS variation shaded.

4.1.2 Experiment

To ensure the simulated results are physically realizable the same test was performed using the robotic sanding system. For this test a gimbal was built to ensure that the sander remains normal to the part surface. This gimbal was installed between the force control unit and the sander as shown in Fig. 4.4. This device passively normalizes the sander to ensure an consistent contact pressure across the pad surface. Using the proposed constant material removal depth control method on a flat part resulted in the test article shown in Fig. 4.6. There was a small issue with gimbal which caused slightly more pressure on the right hand side, the effects of which can be seen with a close inspection of Fig. 4.6. The test article shown in Fig. 4.7 was sanded with a constant contact force and shows less material removed in the center of the part and more near the ends. Differences from the simulated heatmap shown in Fig. 4.2 can again mostly be attributed to normalization errors. On both test articles there is also extra material removed at the top and bottom on both ends. This is caused by oscillations when the contact force is low. Overall, the proposed material removal depth control method does create a reasonably constant depth of material removed in the center section, which is not the case with a constant contact force.

After removing the test article, an electronic drop indicator capable of measuring at a resolution of 0.0001 in was used to measure the depth of material removed along the centerline of each test article as shown in Fig. 4.5. The purpose of these measurements is to record the resulting form of the surface, rather than its roughness. These measurements are plotted in Fig. 4.8. This show the constant depth of material removed in the center section of the part sanded with depth control and how less material is removed in the center section when force control is used. This data can also be used to determine the RMS variation along the centerline of the part using eq. 4.1. Before calculating the RMS variation, the raw data was filtered using a FFT [50, 51] based filter where all spectral components above 0.05 m^{-1} were removed. These calculations show that in this ex-

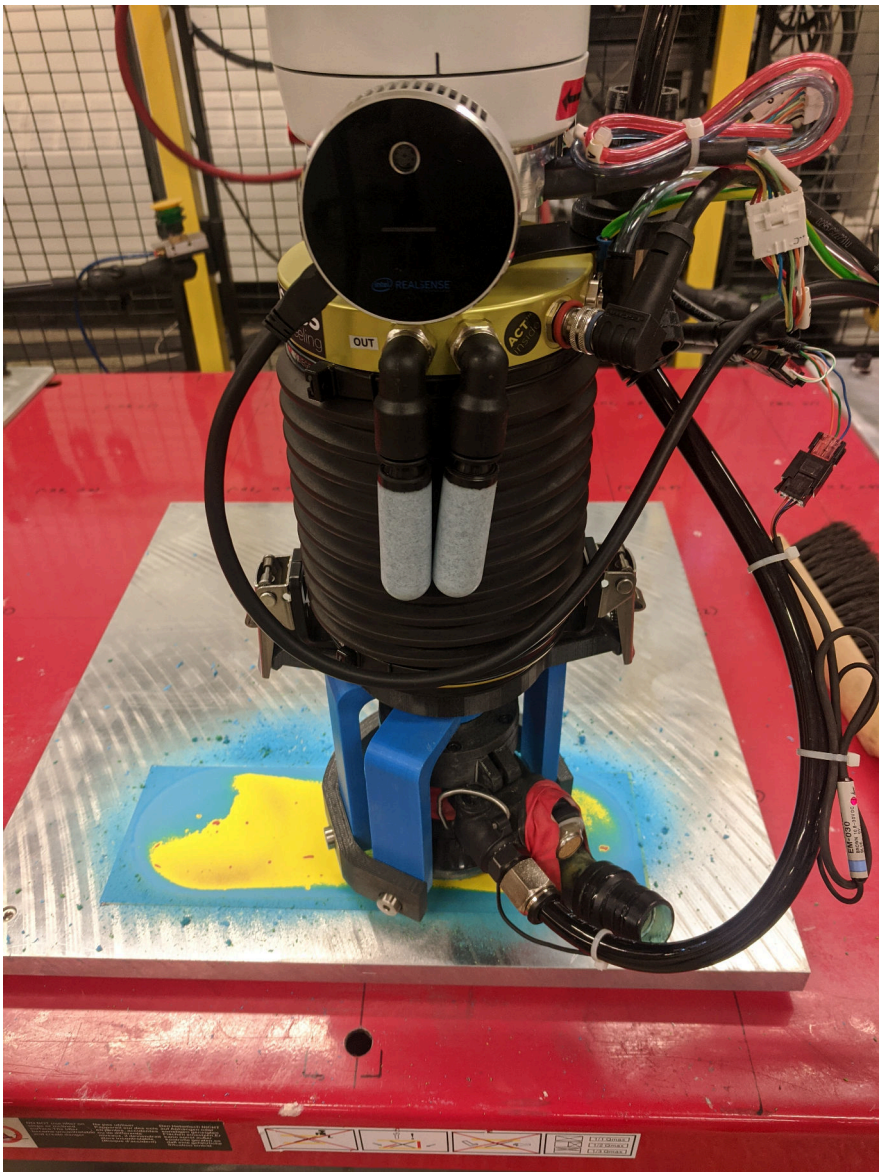

Figure 4.4: A gimbal used to ensure normality of the sander with the part surface.

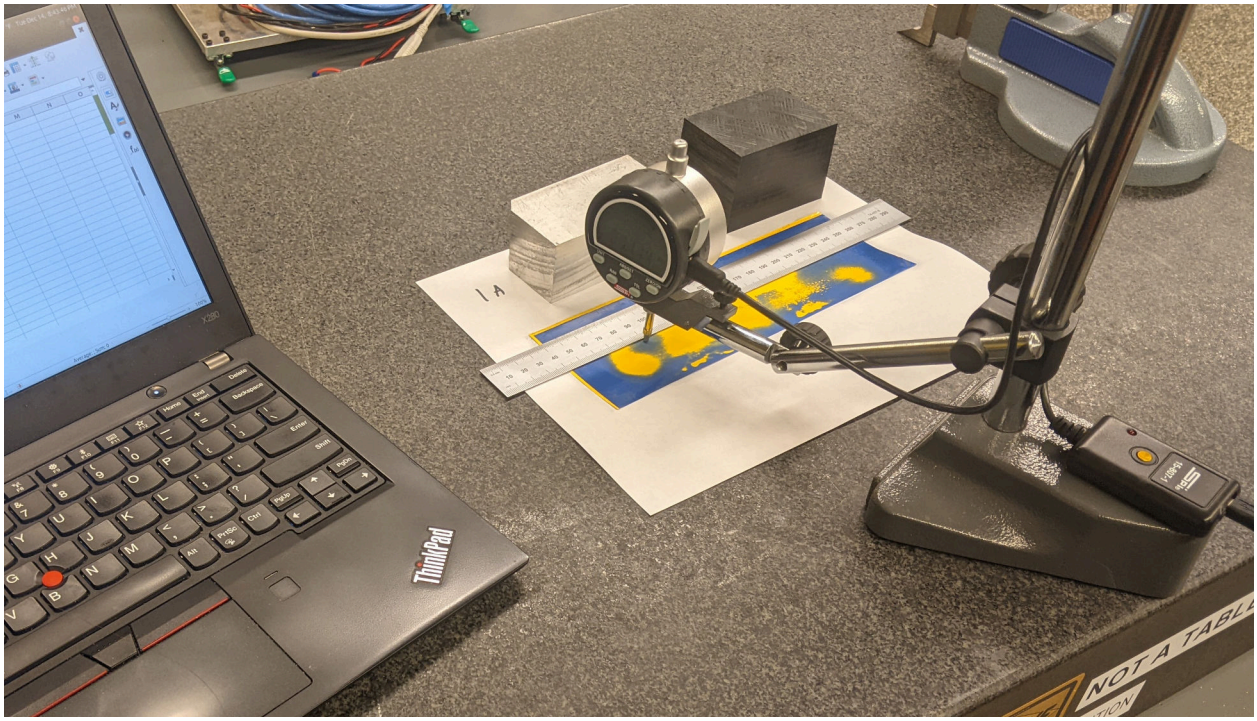

Figure 4.5: The setup used for measuring the sanded test articles consisting of an electronic drop indicator with a resolution of 0.0001 in mounted on a stand and connected to a laptop for data collection. A ruler is used to measure the positions along the part where the height should be measured.

periment the variation was reduced by 32.5% when using the proposed material removal depth control method which is very close to the reduction of 30.4% found via simulation.

4.2 Unconstrained Contact

To test the controller derived for the unconstrained contact area case in Chapter 3, a curved part is used. This curved part was chosen to have a specific curvature of 2 m^{-1} in the x axis, and 1.33 m^{-1} in the y axis. This part was designed with a length of 250 mm and a width

Figure 4.6: The test article sanded using the proposed material removal depth control showing consistent material removed in the center section. The extra material removed at the top and bottom at the ends of the travel is from oscillations in the gimbal when a small force is exerted on the part.

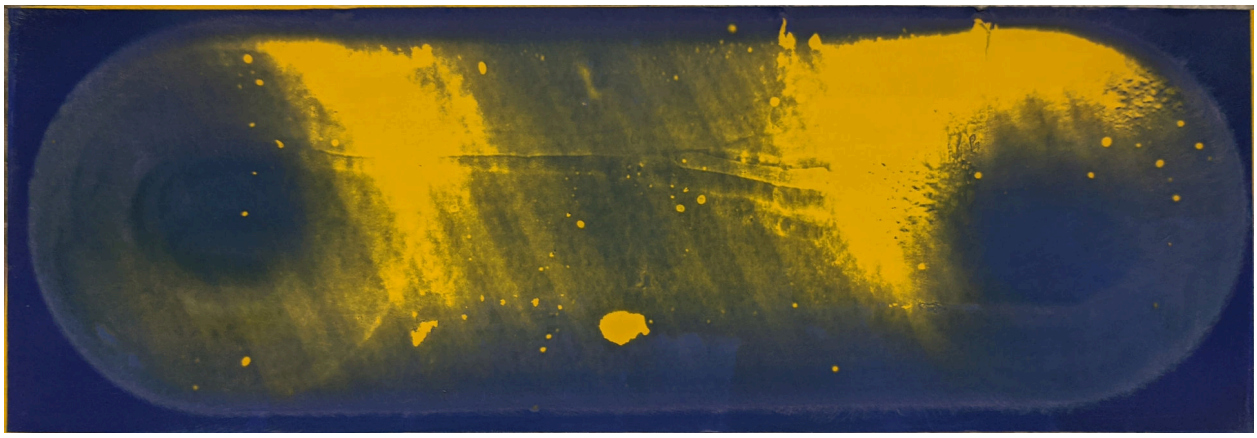

Figure 4.7: The test article sanded using constant force control with more material removed at the ends of the sander travel. The extra material removed at the top is from a small error in normalization during the experiment.

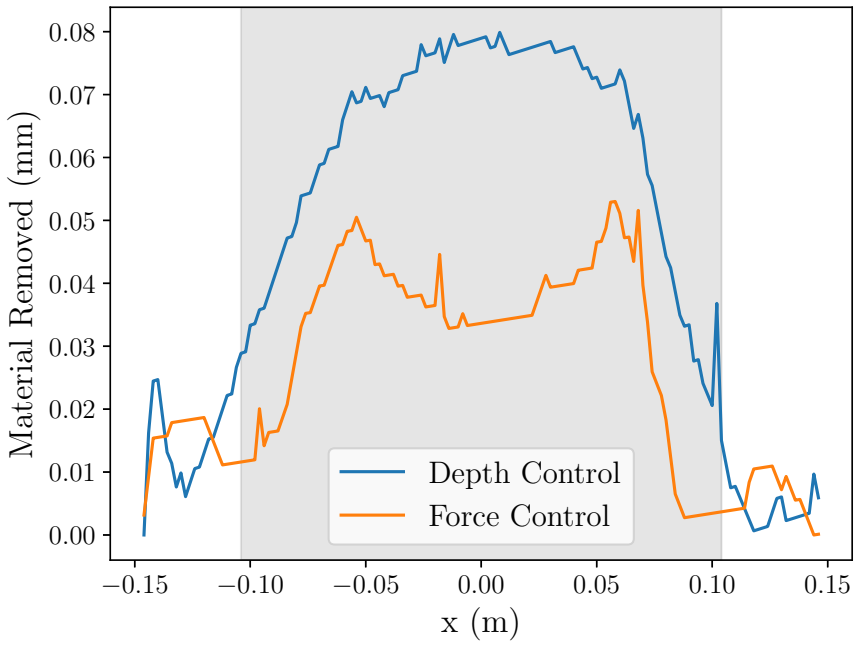

Figure 4.8: The depth of material removed on the centerline of the test parts showing a constant depth of material removed in the center section with depth control including the effect of the normalization errors and with the area used for calculation of the RMS variation shaded.

of 60 mm to accommodate a sanding pad 57 mm in diameter with a modulus of elasticity $\mathcal{E} = 672$ kPa and a thickness $\tau = 9$ mm. To keep the contact area unconstrained, the desired average depth of material removed $\bar{h}$ of 10 μm was chosen. Similarly, a constant force of 18.5 N was chosen as it is approximately the average force applied when using the proposed depth control method.

4.2.1 Simulation

Running this simulation with the proposed depth control method results in the depth of material removed shown in Fig. 4.9. With this setting, the contact forces are low enough to keep the contact area in the unconstrained case for the duration of the sanders movement. As can be seen in Fig. 4.10 this keeps the average depth of material removed relatively constant in the center section of the part and matches the 15 μm desired average depth of material removed. At the ends of the sander travel less material is removed because the sander does not fully cross over these portions of the part. Furthermore, using eq. 4.1 the material removal depth control method the variation is reduced by 81.9% versus constant force control on the same part.

4.2.2 Experiment

To perform the same experiment using the robotic sanding system, a part was 3D printed with the correct curvature. The test article was then stuck to this 3D printed part with removable adhesive. After sanding, the test article can then be removed from the 3D printed part, flattened, and its thickness measured. This setup is shown in Fig. 4.11 including the 3D printed curved part, and the two layer PVC test article. The results of this experiment, first with the proposed material removal depth control method is shown in Fig. 4.12. It can be seen that the ends of the part have been sanded too aggressively because the force control unit has difficulty applying a small force, especially after zero force is requested. Similarly, the results from sanding the same part using a constant contact force can be seen in Fig. 4.13. In this experiment more material was also removed at the top due to normalization errors As

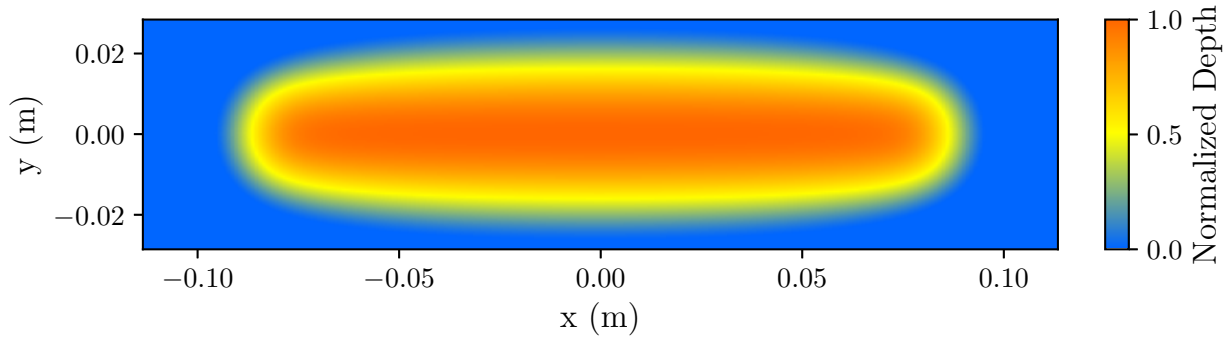

Figure 4.9: The depth of material removed on the surface of a convexly curved part when the sander is moved over the part with a sinusoidally varying position and the contact force is controlled with the proposed method only using the unconstrained contact area case showing the consistent depth of material removed in the center section of the part.

expected, there is less material removed in the center section of the part and more removed towards the ends when sanding with a constant contact force, while there is a relatively consistently center section of the part sanded with the proposed material removal depth control method.

Again, measuring along the centerline of both parts with the electronic drop indicator results in the plot shown in Fig. 4.14. From this plot it can be seen that along the centerline of the test article sanded with a constant contact force there is a spike in the amount of material removed near each end of the travel with a dip in the middle as also seen in Fig. 4.15. Similarly, the centerline of the test article sanded using the proposed depth control method is relatively constant, as also shown in Fig. 4.15. Calculating the RMS variation from the mean using eq. 4.1, the depth control method reduces the variation in surface height by 51.9%.

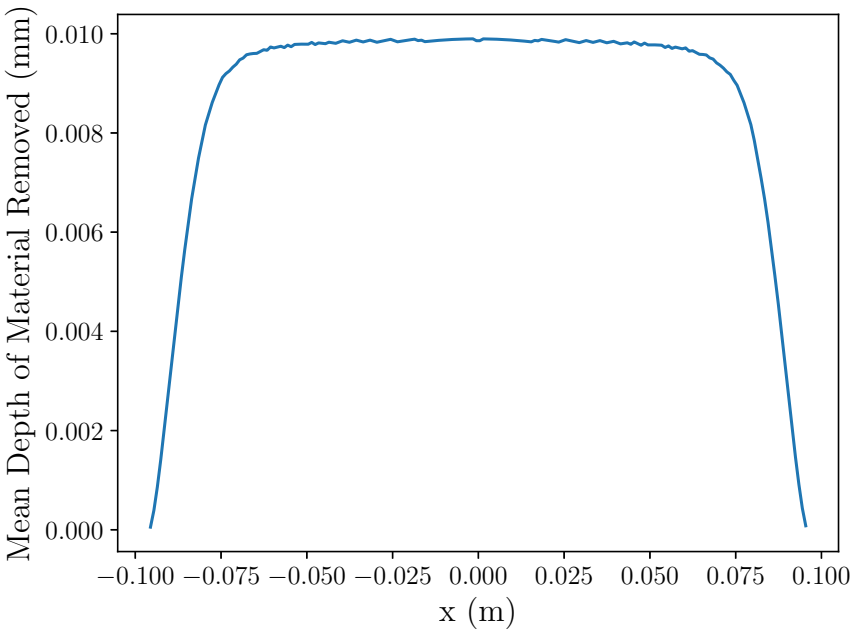

Figure 4.10: The mean depth of material removed on a convex part when the sander is moved over the part with a sinusoidally varying position and the contact force is controlled with the proposed method only using the unconstrained contact area case showing the consistent depth of material removed in the center section of the part.

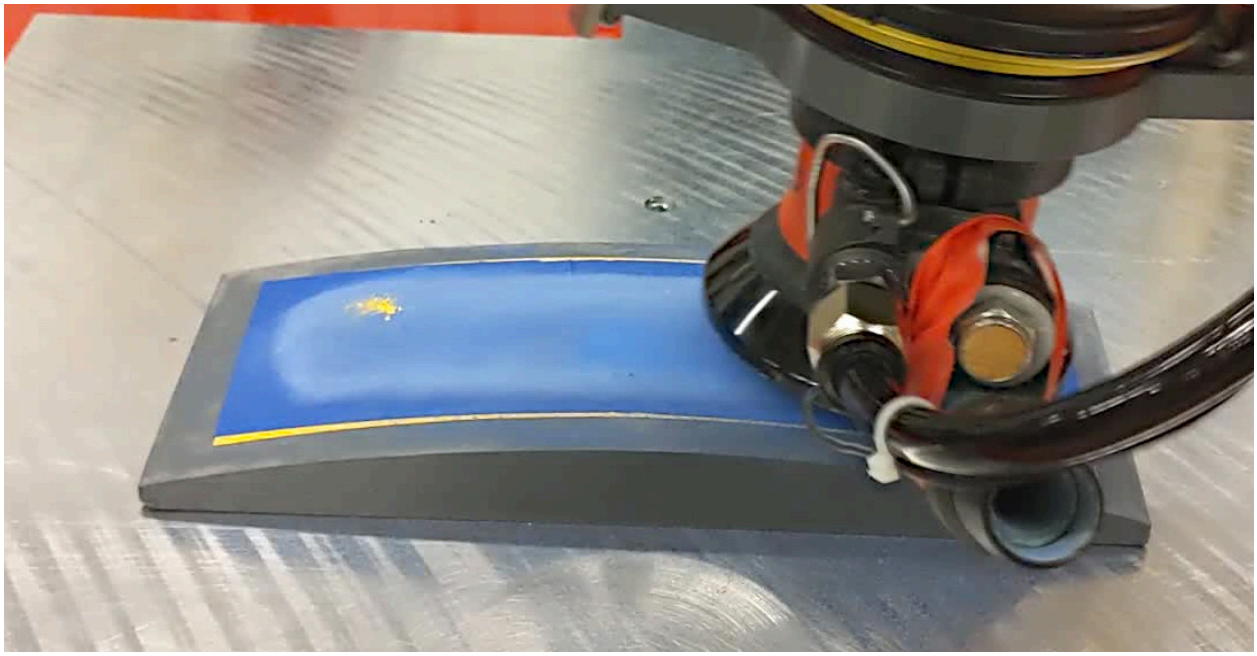

Figure 4.11: The setup for sanding curved test articles consisting of a gray 3D printed part of known curvature, and the thermally welded two layer PVC test article stuck to this surface with removable adhesive.

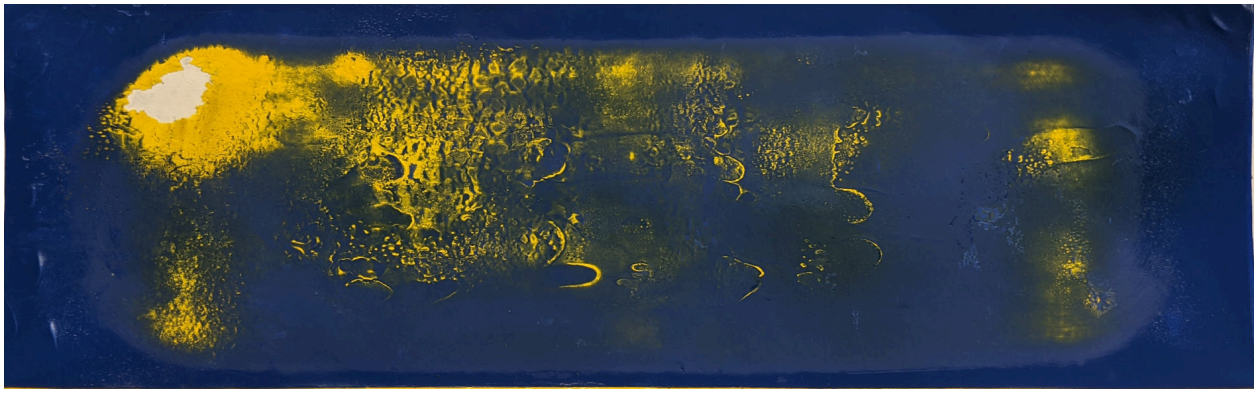

Figure 4.12: The curved test article sanded using the proposed material removal depth control method only utilizing the unconstrained contact area. More material was removed at the ends of the sander travel in this part because the force control unit has degraded accuracy when a low force is applied.

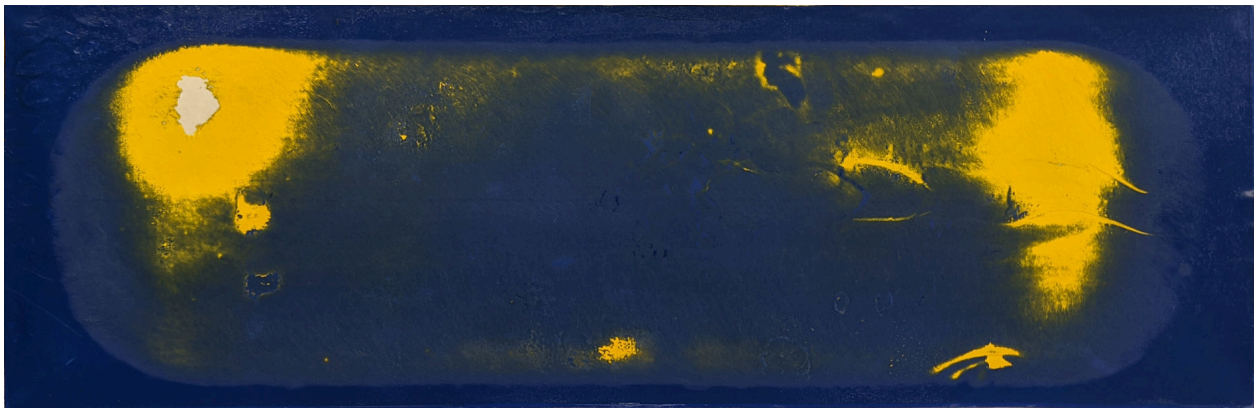

Figure 4.13: The curved test article sanded using constant contact force equal to the average force applied in the validation test using constant material removal depth control and the unconstrained contact area. In this test more material was removed at the ends of the sander travel due to the use of a constant contact force, and more was removed towards the top of the part because of an error in the sander normalization.

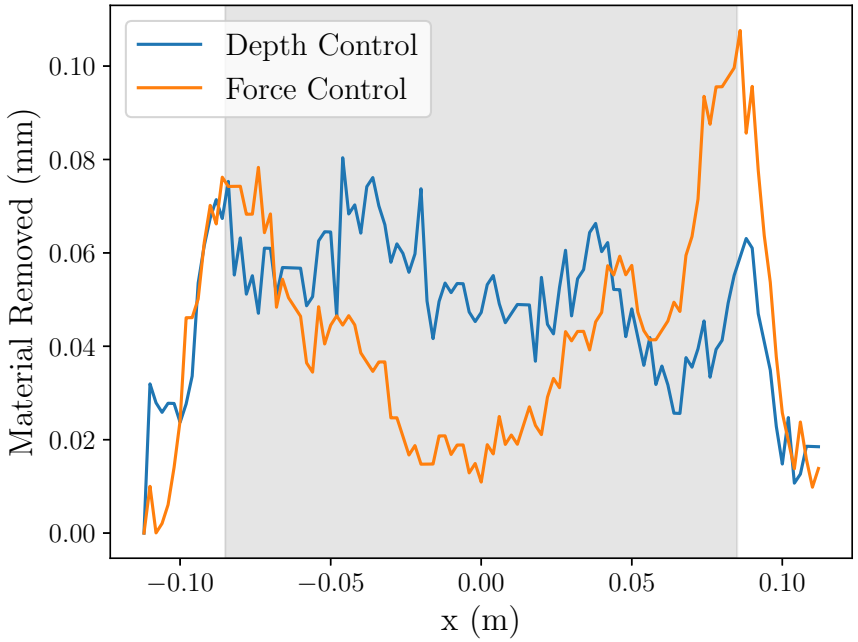

Figure 4.14: The depth of material removed on the centerline ($y = 0$) of a convex test part sanded with the robotic sanding system showing the constant depth of material removed in the center section of the test using the unconstrained contact area case of the proposed material removal depth control method and with the area used for calculation of the RMS variation shaded.

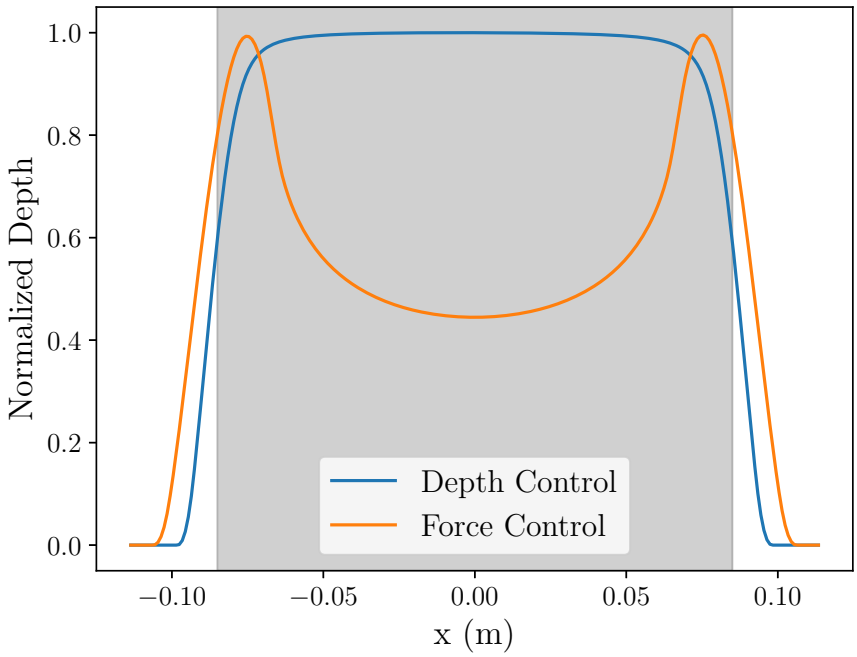

Figure 4.15: The depth of material removed on the centerline ($y = 0$) of a convex part when the sander is moved over the part with a sinusoidally varying position while remaining in the unconstrained contact area case and with the area used for calculation of the RMS variation shaded.

4.3 Partially Constrained Contact

To test the controller for the partially constrained contact, the same method as the previous section was used. In this case a curvature of 1.328 m^{-1} in the x axis, and 0.855 m^{-1} in the y axis was chosen. Using this flatter shape, and slightly more force, the partially constrained contact case can be obtained. To achieve a slightly higher force when using the proposed depth control method, the desired average depth of material removed was increased to $\bar{h} = 12$ μm. Similarly the constant contact force was increased to 22.5 N.

4.3.1 Simulation

Running this simulation with the proposed material removal depth control method results in the depth of material removed shown in Fig. 4.16. With this setting the contact area switches from unconstrained at the beginning when the sander is moving at low velocity to partially constrained as the velocity increases and more force is required. This is shown in Fig. 4.17. In Fig. 4.18 the mean depth of material removed is again shown. This plot shows the correct 12 μm of material is removed and that the center section is again consistent. In Fig. 4.19 the depth of material removed along the centerline ($y = 0$) is shown. The dip in the center of this plot is due to the contact area widening as the sander moves faster. As the sander moves more quickly more force is required to remove the same average depth of material perpendicular to its direction of travel. As the increase in force widens the contact area more material is removed away from the centerline which means less material must be removed at the centerline causing the dip shown in Fig. 4.19. While this dip does exist, the variation in the depth of material removed along the centerline ($y = 0$) is reduced by 79.7% which is less than other contact area cases but is still a significant improvement over constant force control.

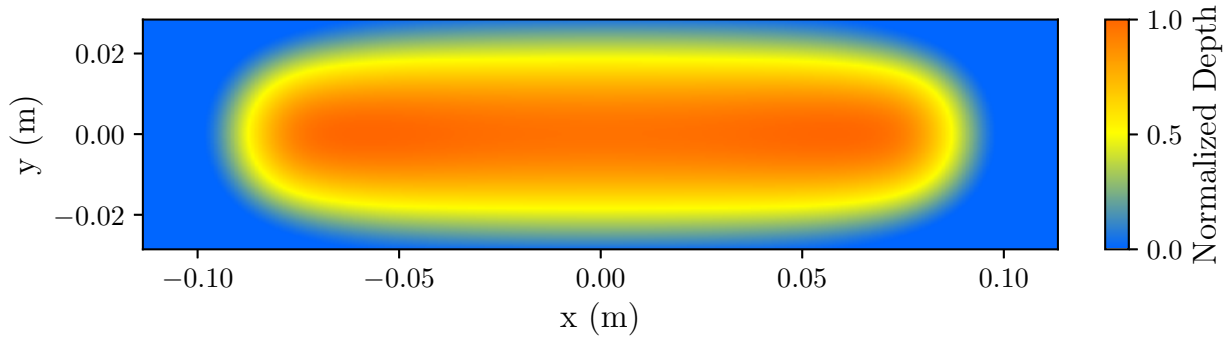

Figure 4.16: The depth of material removed on the surface of a convexly curved part when the sander is moved over the part with a sinusoidally varying position and the contact force is controlled with the proposed method using the unconstrained and partially constrained contact area cases showing the consistent depth of material removed in the center section of the part.

4.3.2 Experiment

Performing this experiment on the robotic sanding system using the proposed material removal depth control method and the same techniques as previous experiments results in the test article shown in Fig. 4.20. While there is some material removed at the ends of the sander travel, the center section looks very consistent. This contrasts well with the test article sanded with a constant contact force shown in Fig. 4.21 where there are large sections of yellow at each end, and very little material removed in the middle. The slight checkered pattern visible on these test articles is due to a minor error in the construction of the curved part, where the facets of the 3D printed part were too large. While not perfect, the measured depth along the centerline ($y = 0$) is shown in Fig. 4.22 is similar to the datas in Fig. 4.19. Although the datas look similar, the RMS variation calculated using eq. 4.1 shows a 27.7% improvement over constant force control which is much smaller than the reduction of 79.7% found via simulation, but still an improvement over a constant contact force.

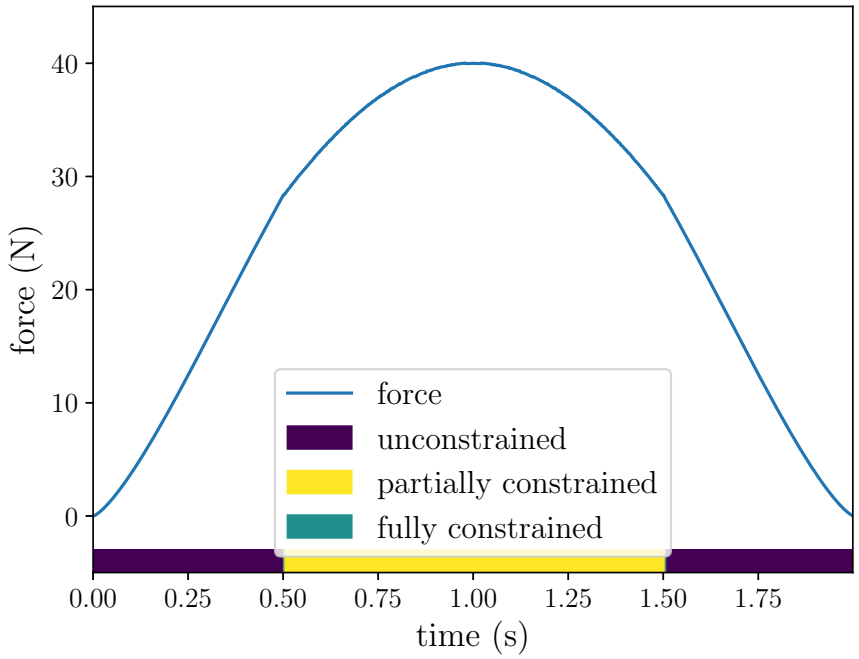

Figure 4.17: The force applied for removing a constant depth of material removed on a convex surface with the contact area cases also shown.

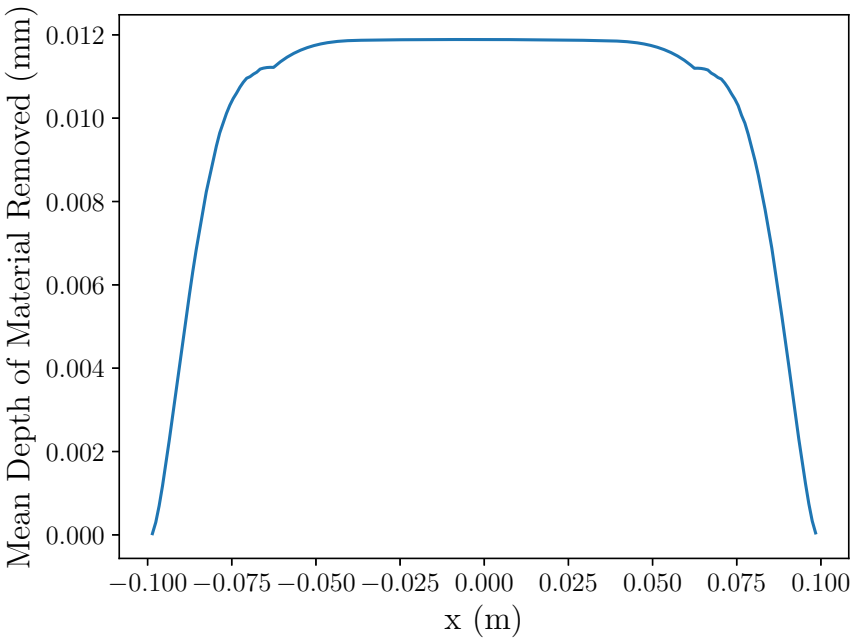

Figure 4.18: The mean depth of material removed on a convex part when the sander is moved over the part with a sinusoidally varying position and the contact force is controlled with the proposed method using the unconstrained and partially constrained contact area cases showing the consistent depth of material removed in the center section of the part.

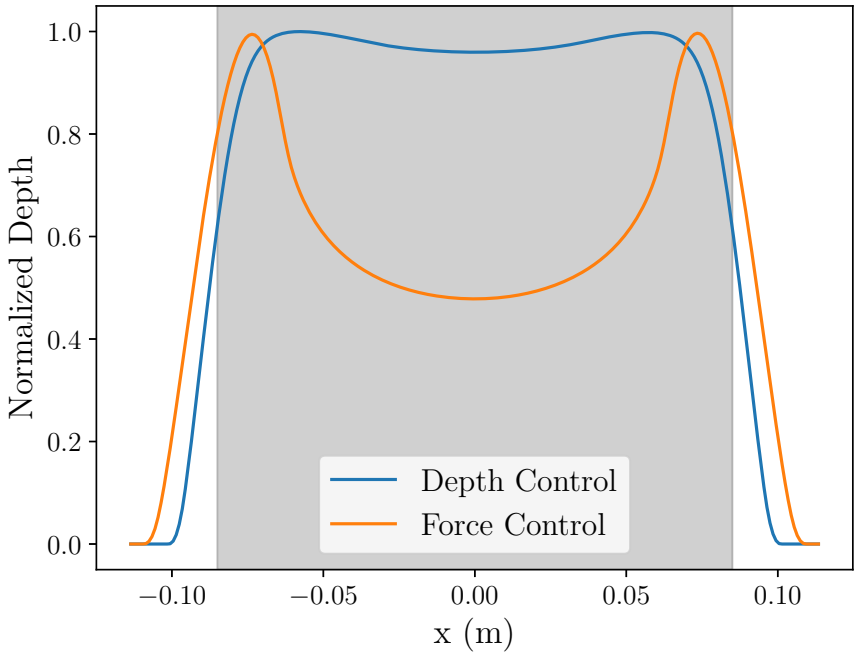

Figure 4.19: The depth of material removed on the centerline ($y = 0$) of a convex test part showing the constant depth of material removed in the center section of the test using the unconstrained and partially constrained contact area cases of the proposed material removal depth control method and with the area used for calculation of the RMS variation shaded.

Figure 4.20: The curved test article sanded using the proposed material removal depth control method only utilizing the unconstrained and partially constrained contact areas. More material was removed at the ends of the sander travel in this part because the force control unit has degraded accuracy when a low force is applied.

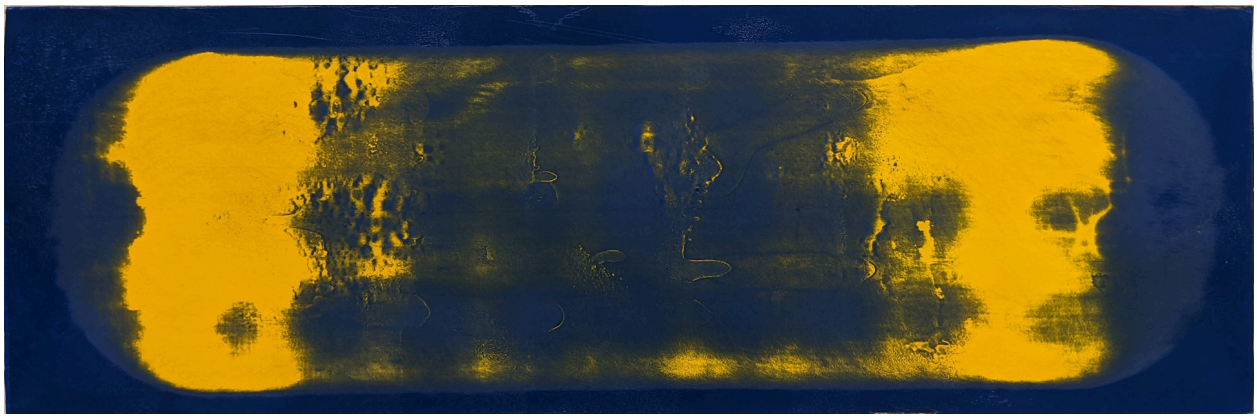

Figure 4.21: The curved test article sanded using constant contact force equal to the average force applied in the validation test using constant material removal depth control and the unconstrained and partially constrained contact areas. The mild checkered pattern is due to slight variations in the part surface from 3D printing.

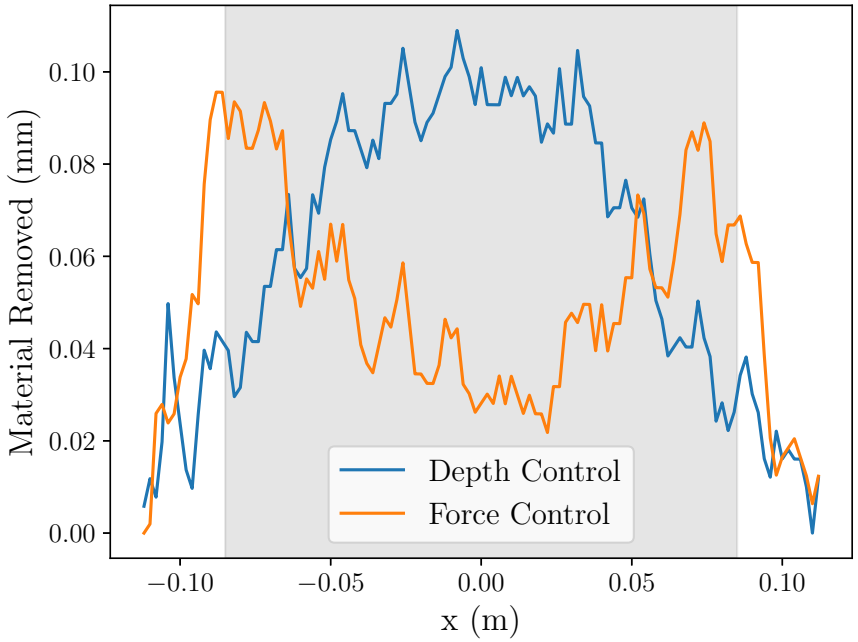

Figure 4.22: The depth of material removed on the centerline ($y = 0$) of a convex test part sanded with the robotic sanding system showing the constant depth of material removed in the center section of the test using the unconstrained and partially constrained contact area cases of the proposed material removal depth control method and with the area used for calculation of the RMS variation shaded.

4.4 Fully Constrained Contact

Finally, to test the fully constrained contact area case, the part curvature was flattened to a curvature of 0.885 m^{-1} in the x axis, and 0.59 m^{-1} in the y axis. The desired average depth of material removed was also increased to $\bar{h} = 13$ μm, and the constant contact force was increased to 26 N. These changes allow the robotic sanding system to achieve the fully constrained contact area.

4.4.1 Simulation

Running this simulation with the proposed material removal depth control method results in the heatmap shown in Fig. 4.23 which has a consistent amount of material removed in the center section of the part. When sanding this part, the contact force changes depending on a number of factors as shown in Fig. 4.24. In this plot it can be seen that as the force is increased, the contact area case changes, utilizing all three cases. Again, the average depth of material removed is constant in the center section of Fig. 4.25 and matches the specified 13 μm average depth of material removal. Moreover, using eq. 4.1 the proposed depth control method reduces the variation in the depth of material removed by 78.3% as shown in Table 4.1.

4.4.2 Experiment

Using the robotic sanding system to perform this test with the proposed material removal depth control method produced the test article shown in Fig. 4.26. Although there are still areas at the ends where more material was removed than desired, the center section of the part looks to be relatively evenly sanded. When compared to the test article sanded with a constant contact force, shown in Fig. 4.27, the much greater depth of material removed at the ends of the test article is readily apparent. Measuring the test articles along their centerlines ($y = 0$) results in the plot in Fig. 4.28. In this plot the areas at the ends of the test article sanded with the proposed material removal depth

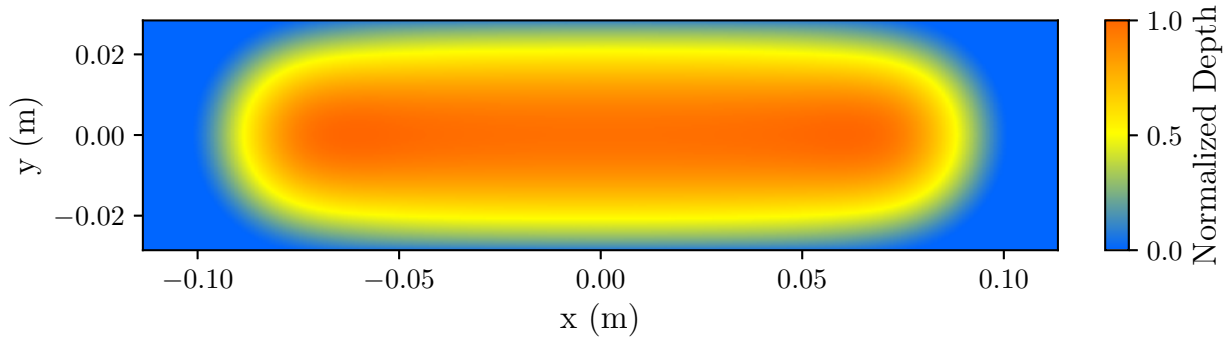

Figure 4.23: The depth of material removed on the surface of a convexly curved part when the sander is moved over the part with a sinusoidally varying position and the contact force is controlled with the proposed method using all contact area cases showing the consistent depth of material removed in the center section of the part.

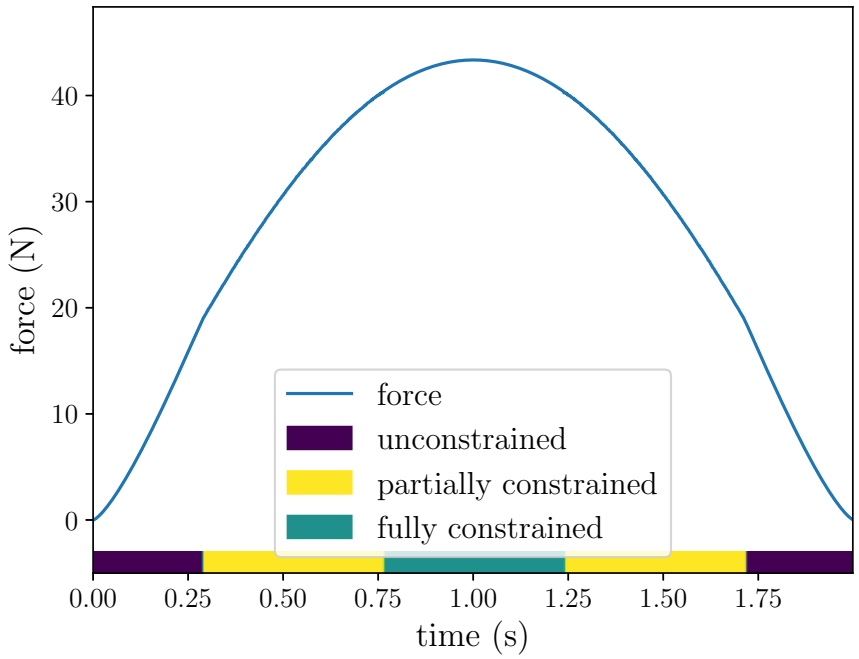

Figure 4.24: The force applied for removing a constant depth of material removed on a convex surface with the contact area cases also shown.

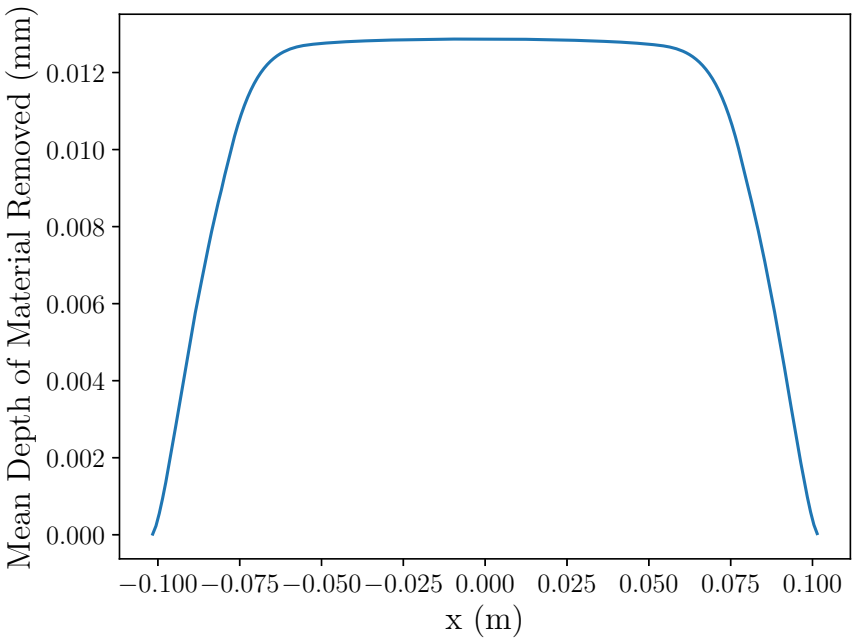

Figure 4.25: The mean depth of material removed on a convex part when the sander is moved over the part with a sinusoidally varying position and the contact force is controlled with the proposed method using all contact area cases showing the consistent depth of material removed in the center section of the part.

Figure 4.26: The curved test article sanded using the proposed material removal depth control method only utilizing all three contact area cases. A minor normalization error is also visible here.

control method can be seen. While the two profiles shown look similar, calculating the RMS variation from the mean using eq. 4.1 shows a 20.1% reduction in surface variation.

4.5 Conclusion

As shown in Table 4.1 the RMS variation from the mean depth of material removed found using eq. 4.1 is reduced when the proposed material removal depth control method is used both in simulation and in experiments performed on the robotic sanding system. While in simulation, the RMS variation is greatly reduced (by around 80%) when curved surfaces are sanded, the reduction is lower at around 30% when a flat surface is sanded. Although this isn't as high as 80%, it is still a notable improvement. However, when the robotic sanding system is used to do the same experiments, the results are slightly different. While on flat surfaces the reduction in RMS variation is almost identical to the simulation results, on curved surfaces the performance is reduced. For unconstrained contact depth control reduces

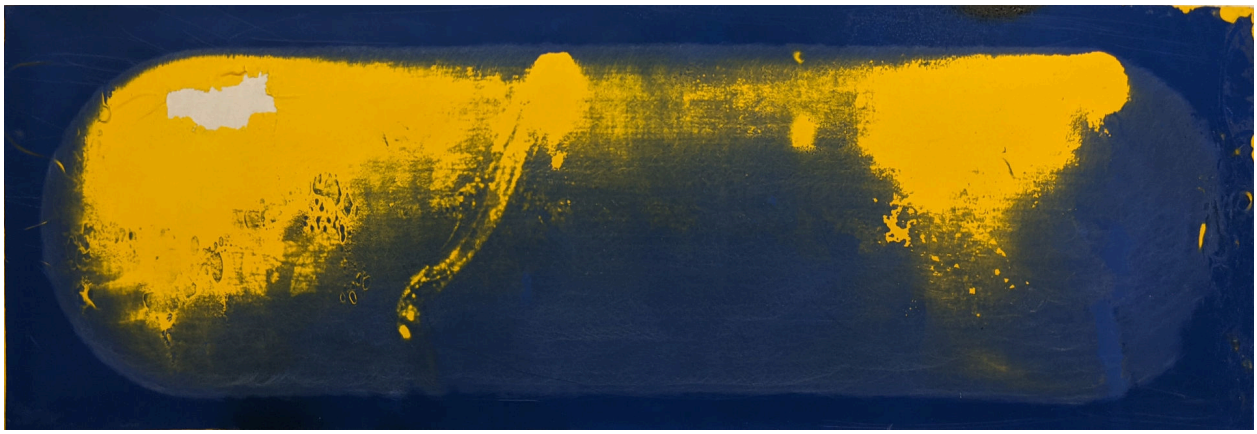

Figure 4.27: The curved test article sanded using constant contact force equal to the average force applied in the validation test using constant material removal depth control and all three contact area cases. The excess material removed at the ends of the sander travel and small amount removed in the middle is visible along with a small normalization error favoring the top of the part.

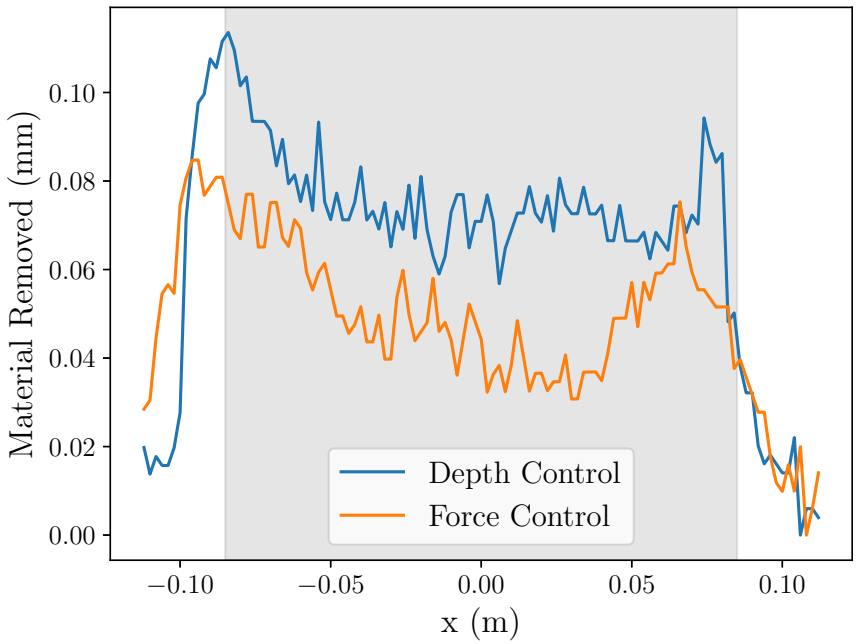

Figure 4.28: The depth of material removed on the centerline ($y = 0$) of a convex test part sanded with the robotic sanding system showing the constant depth of material removed in the center section of the test using all three contact area cases of the proposed material removal depth control method and with the area used for calculation of the RMS variation shaded.

Table 4.1: The RMS variation from the normalized mean depth of material removed along the centerline of the part ($y = 0$) calculated using eq. 4.1 in the center section of the part that the center of the sanding pad completely covers (ignoring one radius of the sanding pad from each end) for flat parts and curved parts with an unconstrained, partially constrained, and fully constrained contact areas.

	Simulation			Experiment		
Constraint	Force Control	Depth Control	Percent Change	Force Control	Depth Control	Percent Change
Flat	0.268	0.187	-30.4%	0.435	0.294	-32.5%
Unconstrained	0.434	0.0783	-81.9%	0.59	0.284	-51.9%
Partial	0.397	0.0807	-79.7%	0.466	0.337	-27.7%
Full	0.363	0.0788	-78.3%	0.389	0.311	-20.1%

the RMS variation by about 50%, while for partially and fully constrained contact areas, the RMS variation is reduced by 20% to 30% versus a constant contact force. As this reduction in the improvement is also correlated with an increase in force, this may be caused by other issues such as clogging of the sanding pad or nonlinearities in the pad compliance. Overall, the proposed material removal depth control method shows improvement in all cases both in simulation and physical experiments.

Chapter 5

INITIAL VIRTUAL HUMAN ROBOT INTERACTION EXPERIMENT

To check that the method derived in Chapter 3 improves the work of human operators, a human robot interaction experiment was designed and conducted. This experiment allows a quantitative comparison of constant force control and the proposed material removal depth control method with a human operator. By answering a series of questions after the experiment the operator's feelings on the different methods of control can also be measured. For this experiment, a human operator moves a sander over a part surface along a single axis and is tasked with sanding away the top layer of a multi-layer part. A change in color will allow the operator to determine when the first layer has been removed. The operator will perform the same experiment with both constant force control and the proposed constant material removal depth control. Using the data from this experiment, both the quantitative performance of the human robot system and the qualitative performance of the system can be analyzed. Both measurements are important for the system to be accepted in a manufacturing environment. First, when using the system the quality of the final product must be as good or better than those from existing tools otherwise it will not be accepted because it cannot meet the quality expectations for the process. Second, the operators must prefer the system over other available tools. If operators prefer existing tools they may use them instead of new tools even if the new tool has been shown to produce better results. For these reasons the proposed material removal depth control method must produce better parts and be preferred by operators.

To test if these conditions are true, an experiment was performed where a human operator is tasked with sanding away the top layer of a multi-layer part. This multi-layer part has

different colored layers so the human operator can determine how much they have sanded in a given area. To test the proposed material removal depth control method this part is sanded twice, once with the proposed controller, and once with a constant contact force in a random order. After sanding, the operator is asked a series of questions to determine their opinion on the control methods used.

In this experiment a flat part 0.3 m long and that 30% of the sander is allowed to hang over the end of the part is sanded. The velocity is limited to 0.18 $\frac{\mathrm{m}}{\mathrm{s}}$ and the acceleration is limited to 0.18 $\frac{\mathrm{m}}{\mathrm{s}^2}$ except at the ends of the part where deceleration is not limited. Before attempting sanding, the operator is given a chance to try out the sanding process to familiarize themselves with the controls. As well as investigating the difference between a constant contact force and the proposed material removal depth control method, the difference between tests where the operator is able is able to see where they have sanded too far is also explored. This is implemented by having a single transition from a starting color to a goal color when over-sanding is not shown, and a second transition from the goal color to a third over-sanded color when over-sanding is shown. These two cases will be evaluated separately to determine if this has any effect on the quantitative results or operators feelings.

5.1 Virtual Environment

To simplify the initial experiment, a virtual environment was created. This allows easy replication and sharing of the experiment since no physical hardware is needed. The environment was created to run in a web browser using THREE.js to render the sander, workpiece, and table as shown in Fig. 5.1. In this environment, the sander follows the mouse cursor and pressing the left mouse button causes it to contact the part surface while releasing the left mouse button causes it to raise slightly off the part surface. When the sander is at the end of its travel a portion of it hangs off the edge of the part resulting in a non-constant pressure distribution which is simulated in the spatial distribution of material removal at that location. This environment was used for initial human robot interaction experiments since it easily allows rapid experiment changes.

Figure 5.1: The virtual environment used for the initial human robot interaction experiment.

5.2 Stationary Sander Detection

In trial experiments, an issue was identified where operators would stop the sander while it was touching the surface. It was assumed the operator was attempting to remove material at a single location. With constant force control this had the desired effect; however, with the proposed depth control method, stopping the sander results in no force being applied. For example, setting $v_l = 0$ in eq. 3.46 results in zero contact force. To mitigate this issue, a system was designed to apply a constant force when the sander is near stationary. To determine when the sander should be considered stationary a Gaussian Mixture Model with two components was fit to the recorded velocity data from initial virtual experiments as shown in Fig. 5.2. Both Gaussian Mixture Model components are centered at approximately zero velocity. The first component has a low standard deviation, and the second has a higher standard deviation. Therefore, low velocities which should be considered stationary are more likely in the first component rather than the second. However, when the sander switches the direction it is moving the velocity will pass through zero. To avoid this system applying extra force when this happens, a low pass filter with a time

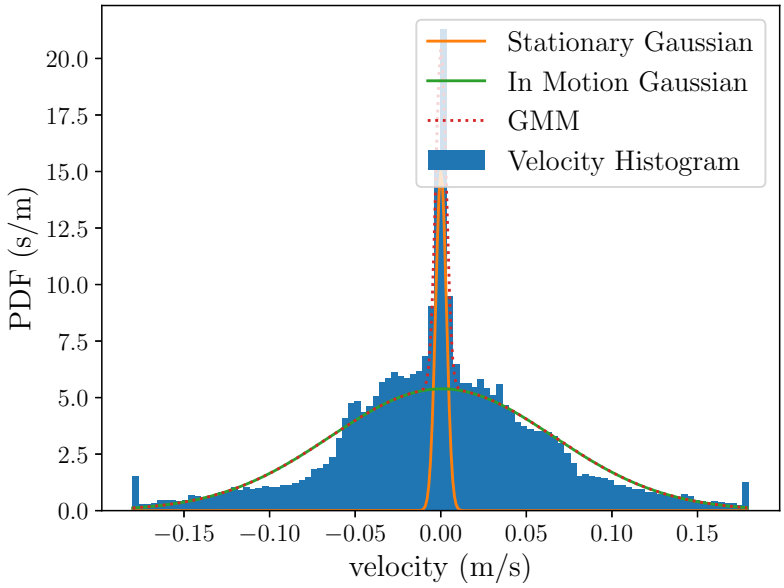

Figure 5.2: The distribution of sander velocities from human operators with a two component Gaussian Mixture Model.

constant of 0.05 s was applied to the likelihood of the current velocity being classified as stationary by the Gaussian Mixture Model. If the output value of the low pass filter is greater than 0.5 then the sander can be considered stationary and a constant force applied. Further experiments showed this system did not apply extra force when the sander was changing directions and applied a constant contact force[1] in the areas previously identified.

[1]The constant contact force set when using the stationary sander detection is typically the same value as used for constant force control.

5.3 Results

This experiment was completed by 15 people. The root mean square variation from the average depth of material removed[2] on the four experiments was calculated. The variation from the average depth removed, rather than the goal depth, was chosen as this eliminates any potential errors from misjudging the goal depth color. Again, only the center section of the part was used, this time the area the sander completely passes over. These RMS variation values are shown in Fig. 5.3. As can be seen in the figure, parts sanded with the proposed material removal depth control method have a lower RMS variation. Also, when the human operators were able to see the areas where they have over-sanded the part, they produce parts with lower RMS variation. This implies both that the proposed material removal depth control method is helping the human operators as expected, and that when they cannot see when too much sanding has occurred in a given area, they are happy to continue sanding that area.

While the RMS variation results for the center section of the part look promising, the operators can see the entire part. Therefore, the RMS variation for the full part were also calculated and are shown in Fig. 5.4. There is still a decrease in the RMS variation when the over-sanded areas are visible. However, when looking at the full part, there is very little difference in the RMS variation when using a constant contact force versus the proposed material removal depth control method. This is an indication of the difficult of completing the task perfectly. As qualitative methods are also used to evaluate the proposed control method, which will inherently be based on the operators visual analysis of the resulting part, this issue may skew the results.

Even if little to no change is visible when looking at the entire part, the qualitative results do show promise. For these questions the operator is asked to answer whether they agree or disagree with a number of statements and their answers are recorded on a 7 point Likert scale [52]. The first question asked was whether or not the participant agreed with

[2]This same metric was used to evaluate the validation tests in Chapter 4.

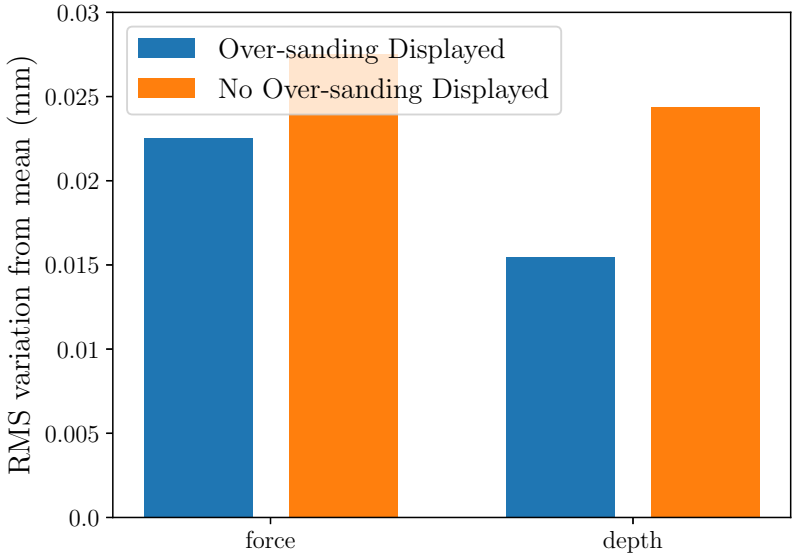

Figure 5.3: The RMS variation from the mean depth of material removed in the center section of the part which the sander fully passes over for the four different experimental conditions in the initial virtual experiment showing better performance when the proposed method is used and when the operator is able to see locations where too much sanding has taken place.

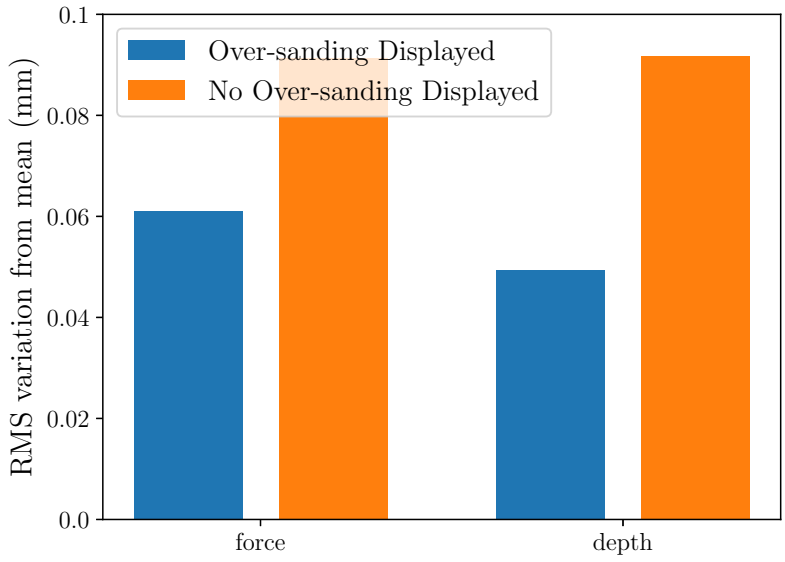

Figure 5.4: The RMS variation from the mean depth of material removed using the entire length of the part for the four different experimental conditions in the initial virtual experiment showing a small change when the proposed method is used and a substantial improvement when the operator is able to see locations where too much sanding has taken place.

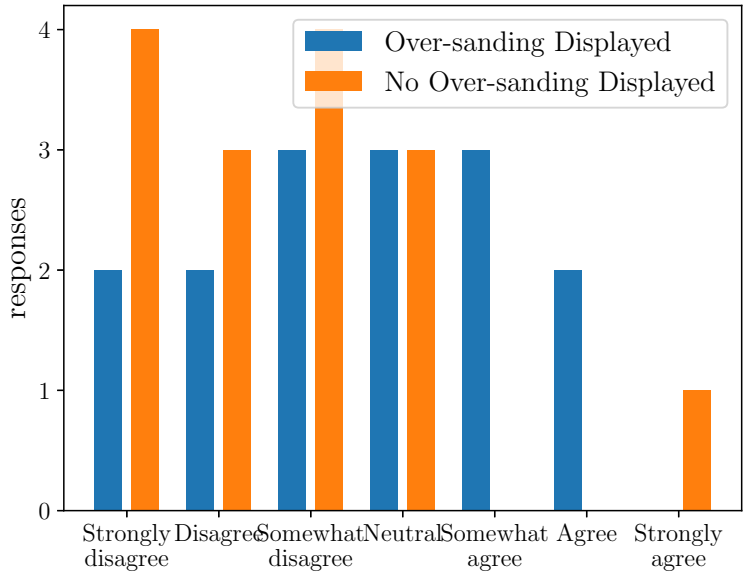

Figure 5.5: Responses to the statement "In test A I was able to produce a better end result than in test B" in the initial virtual experiment where test A uses the proposed material removal depth control method, and test B uses a constant contact force.

the statement "In test A I was able to produce a better end result than in test B" where the order of tests is normalized so test A uses a constant contact force, and test B uses the proposed material removal depth control method. The responses to this question are visible in Fig. 5.5. When over-sanding is not visible to the operators, the responses are biased towards a constant contract force producing a better result; however, when over-sanding is visible, the responses are more neutral. This implies that operators are better able to judge their performance when they can see the areas were they have sanded too much.

Chapter 6

PHYSICAL HUMAN ROBOT INTERACTION EXPERIMENT

To further validate the control method derived in Chapter 3, an experiment should be performed with a human in the loop using the robotic sanding system described in Chapter 1. This experiment should show that the proposed material removal depth control method improves sanding performance, not only in a virtual environment, but also when using the physical robotic sanding system.

6.1 Experiment Design

To show that the proposed material removal depth control method helps operators produce a better sanded part, an experiment similar to the experiment in Chapter 5, was performed. In this experiment, not only will parts with a constant curvature be sanded, but parts with a variable curvature will be sanded as well. While in the previous experiment the constant curvature part was flat, in this experiment a part with a nonzero constant curvature is used. This was chosen to ease normalization because if the contact area is small enough to be in the unconstrained case, a small change in the angle that the sander is contacting the part simply shifts the location of the contact area without changing its shape or pressure distribution.

A part with a variable curvature was also included because of the increased difficulty with these parts. Unlike constant curvature parts where the rate of material removal per unit area is constant if the contact force and abrasive speed are constant, on parts with variable curvature the material removal rate per unit area changes based on the local part curvature as well. This is visible in eq. 3.15 which depends on the contact width, which will change with local part curvature. For this reason, parts with variable curvature are more difficult to sand. An example of a part with variable curvature is shown in Fig. 6.1.

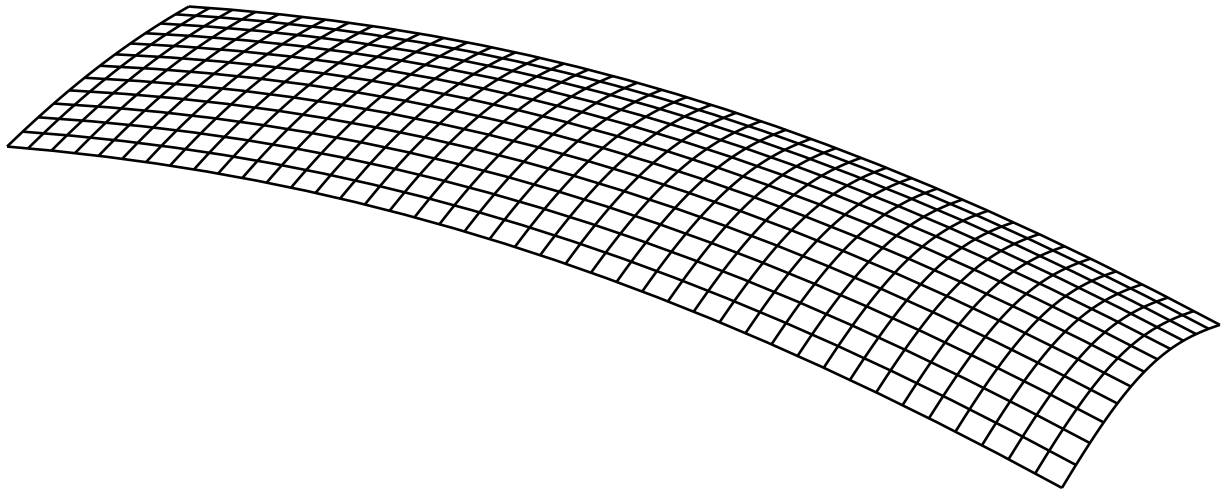

Figure 6.1: The part surface of the curved test article used in the revised experiment with a lower curvature on the left, and a higher curvature on the right.

The test articles used in this experiment are of the same construction as those in Chapter 4. Furthermore, a red color is placed under the two layer test article, so that if a portion of the test article is over-sanded, the red color will begin to show through similar to the experiments where over-sanding is shown in Chapter 5. Figure 6.2 shows the parts of different curvature installed in the robotic sanding system with the multi-layer test articles installed.

For this experiment, a slightly lower maximum speed of 0.126 $\frac{\mathrm{m}}{\mathrm{s}}$ was used. The maximum acceleration was also modified to 0.252 $\frac{\mathrm{m}}{\mathrm{s}^2}$, and like in the initial virtual experiment in Chapter 5 an unlimited deceleration is allowed at the end of the sander travel. The maximum allowed velocity profile is shown in Fig. 6.3. However, during the initial testing of this experiment, it was noted that participants often did not use the maximum velocity of the sanding system, likely because of the visually apparent mass and power of the robot. The lower velocity requested in these cases causes the system to reach a constant velocity faster, which then increases the time at a constant velocity. With

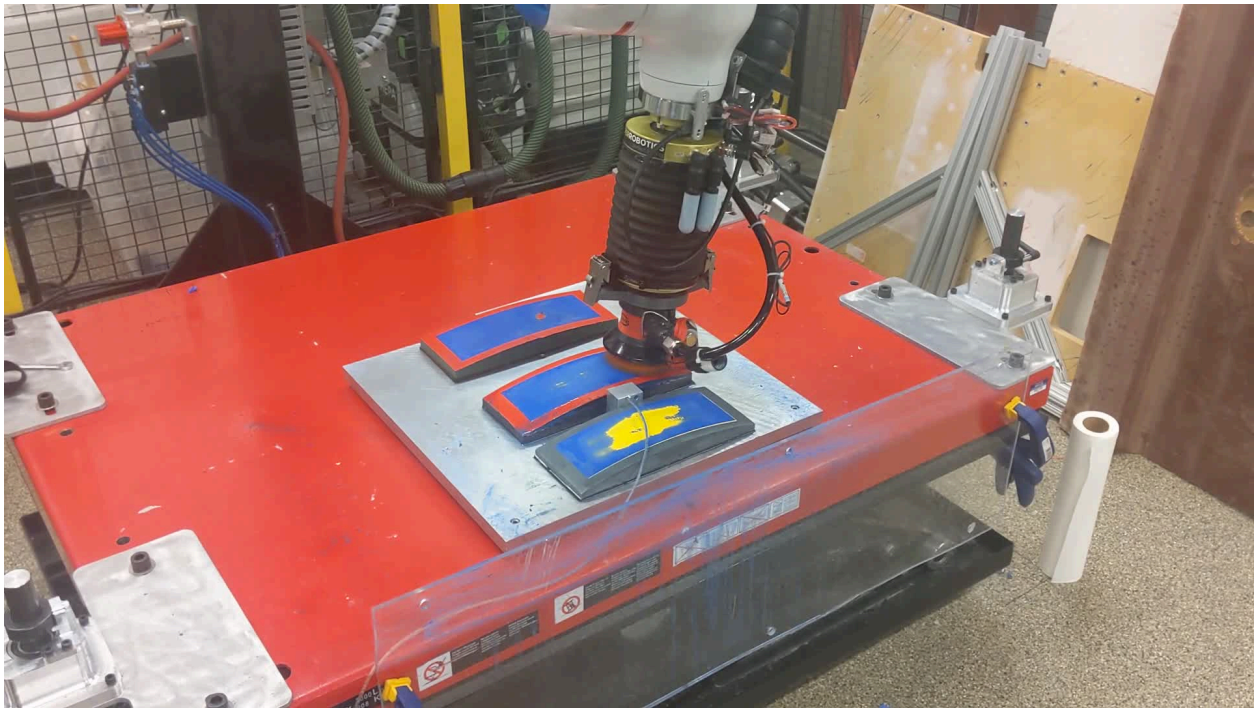

Figure 6.2: The experimental setup for the human robot interaction experiment using the robotic sanding system with multiple parts, one for operators to learn the operation of the system, and two for the experiment, one with a constant curvature, and a second with a variable curvature.

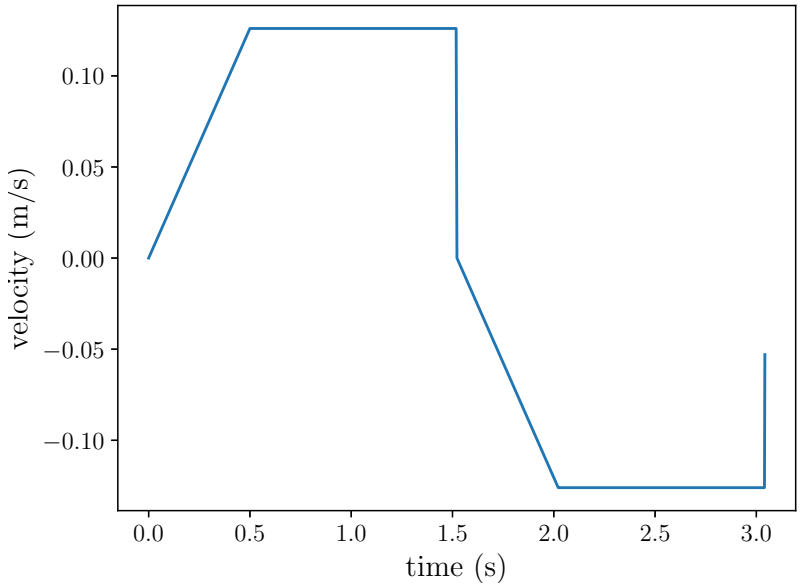

Figure 6.3: The maximum allowed velocity profile in the physical human robot interaction experiment.

a constant velocity and a surface of constant curvature, the proposed material removal depth control method requests a constant contact force. To fix this issue, the operation of the robotic sanding system was changed from an analog control of the desired sander linear velocity using a game controller joystick, to a binary velocity control using the same human interface device. This binary control allows the operator to select a desired velocity of zero, full speed right, or full speed left using the same joy stick as before.

The part with a constant curvature was sanded with a constant force of up to 18.5 N, which is variable using a trigger on the game controller user interface device. When sanding the same part with the proposed material removal depth control method, the maximum average depth of material removed was set to 10 μm and is variable in the same way as the force. For the part with a variable curvature, when sanded with a constant contact force

a maximum of 20 N is used, and when sanded with the proposed material removal depth control method the maximum average depth of material removed is 1.2 μm. The stationary sander detection method from Chapter 5 was also implemented.

6.2 Results

In the end, four participants completed this experiment. The difficulty of making the test articles and other time consuming aspects of this experiment made if difficult to increase the sample size. However, as this experiment has some similarities to other experiments, agreement with other results helps to validate results obtained using the physical robotic sanding system.

To determine which control methods result in a more evenly sanded part, the RMS variation from the mean was calculated using eq. 4.1 for the center section of the part which the sander fully passes over. These values are shown in Fig. 6.4. From this figure it can be seen that there is a reduction in the RMS variation when using the proposed material removal depth control method when sanding a surface with a constant curvature. However, there is a more significant reduction when sanding a surface with a variable curvature.

After sanding using both control methods, operators were asked the same questions as in Chapter 5. The responses to the statement "In test A I was able to produce a better end result than in test B" where the randomly ordered responses have been normalized so that test A uses the proposed material removal depth control method, and test B uses a constant contact force are shown in Fig. 6.5. When sanding the part with a constant curvature the participants tended to believe that a constant contact force resulted in a better sanded part, and when sanding the part with a variable curvature, the opinions were mixed. Although the operators judgment on which method produces a better end result does not match the RMS variation data, the participants did notice the greater reduction in RMS variation on surfaces with variable curvature.

The responses to the statement "In test A I was able to more precisely remove material than in test B" are shown in Fig. 6.6. These responses heavily favor a constant contact force

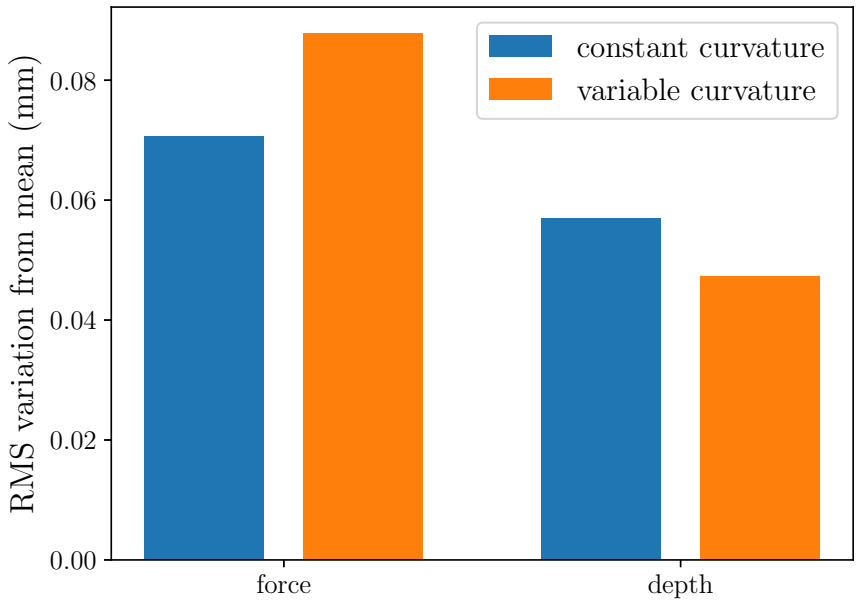

Figure 6.4: The RMS variation from the mean depth of material removed in the center section of the part which the sander fully passes over for the four different experimental conditions in the physical experiment showing better performance when the proposed method on parts with both a constant and variable curvature, but showing more improvement on the surface with variable curvature.

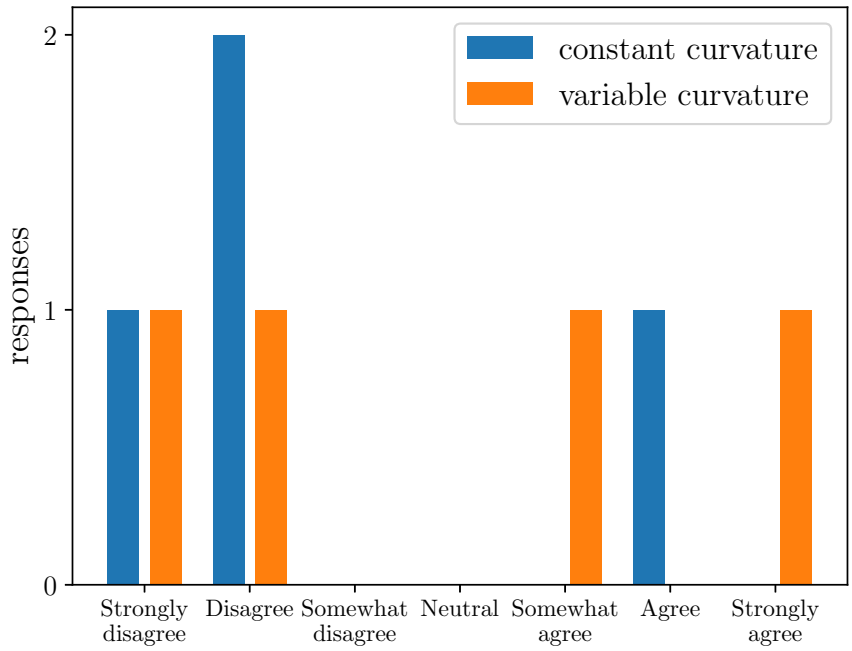

Figure 6.5: Responses to the statement "In test A I was able to produce a better end result than in test B" in the physical experiment where test A uses the proposed material removal depth control method, and test B uses a constant contact force.

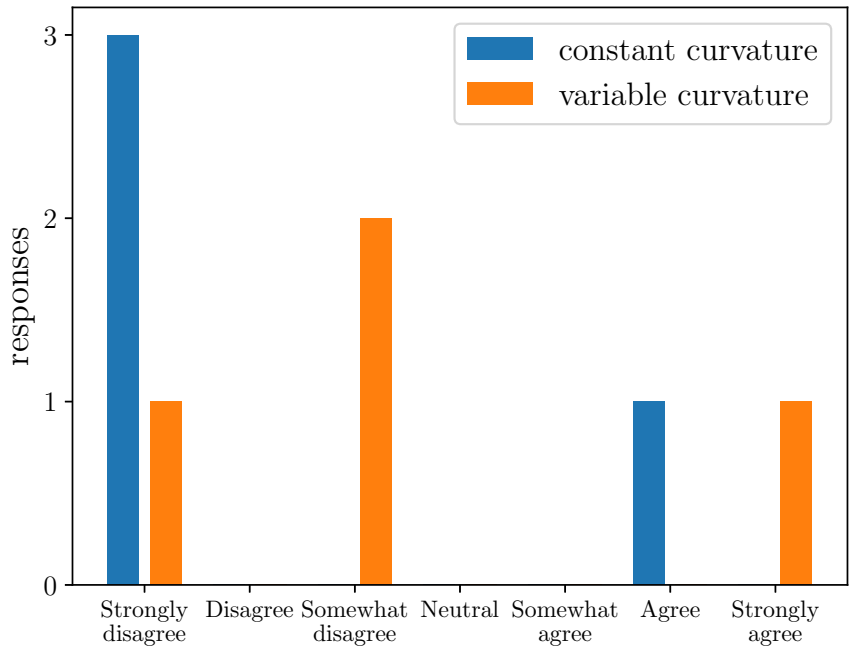

Figure 6.6: Responses to the statement "In test A I was able to more precisely remove material than in test B" in the physical experiment where test A uses the proposed material removal depth control method, and test B uses a constant contact force.

as the method for more precisely removing material on a surface with constant curvature, but again are more mixed on surfaces with variable curvature. However, when looking at the responses to the statement "I preferred the operation of the sander in test A over test B" shown in Fig. 6.7, a constant contact force is preferred on surfaces with both constant and variable curvature. This implies some participants prefer a control method which they don't think produces a better end result. The difference here may be that the human operators don't understand how the material removal depth control system is working, and therefore don't prefer it, even though they see it produces better results.

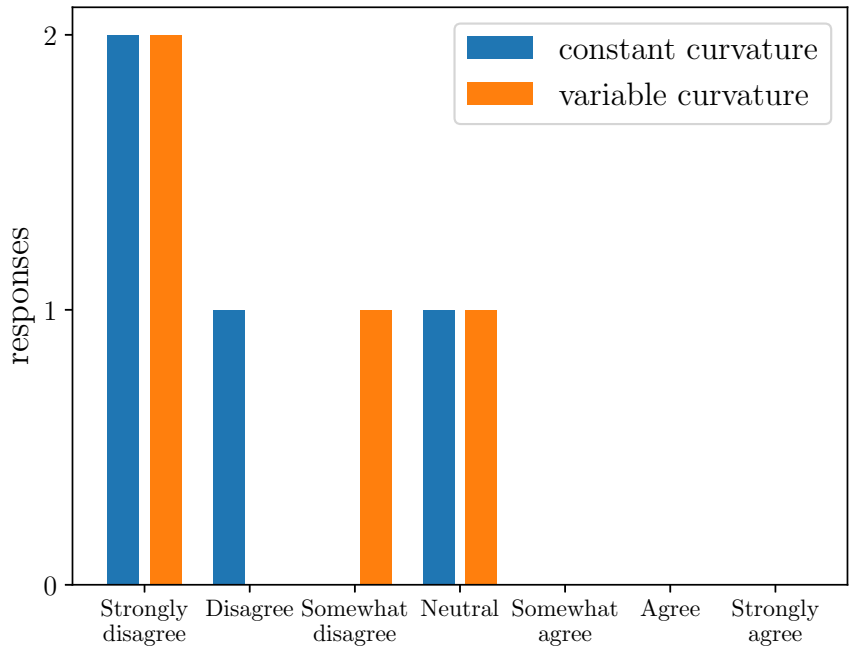

Figure 6.7: Responses to the statement "I preferred the operation of the sander in test A over test B" in the physical experiment where test A uses the proposed material removal depth control method, and test B uses a constant contact force.

6.3 Conclusion

Overall, this experiment shows some of the benefits of the proposed material removal depth control method. While the RMS variation was improved on both constant and variable curvature surfaces, operators were not always able to see this improvement. For example, when sanding the surface with a constant curvature the operators believe they created a better end result with constant force control which is not in agreement with the RMS variation data which shows a 19% reduction. Interestingly, while sanding surfaces with a variable curvature, participants thought they created a better end result with the proposed material removal depth control method, they still preferred the and thought a constant force was more intuitive. This is likely due to to the fact that in experiments using the robotic sanding system the operator can judge the force applied to the part by the sound of the sander and the characteristics of the systems motion. Being able to judge the force applied could confuse the operators when the proposed material removal depth control method is used because the amount the trigger on the game controller is pulled, does not directly correlate with the force applied. This could imply that more training or time to get acquainted with the proposed control method is required. Furthermore, to avoid clogging of the sand paper, WD-40 was used as a lubricant. While this did an effective job of avoiding clogging it also created a slurry of swarf and WD-40 over the part surface which did, at times, make it difficult to judge the color at times. The small sample size could also be affecting these results, but they can be validated with future experiments.

Chapter 7

REVISED VIRTUAL HUMAN ROBOT INTERACTION EXPERIMENT

After the experiments in Chapters 5 and 6, a few deficiencies were found. First, it was determined that not bounding the deceleration at the end of the sander's travel benefited constant force control, making it more likely for operators to prefer that control method. This is because when the linear velocity which the sander is moving at remains constant, the force to achieve a given depth is constant as well. Secondly, the areas at the end of the part greatly effect the overall RMS variation as can be seen when comparing Figs. 5.3 and 5.4. It is probable this is also affecting the operators preferences, therefore the areas where the sanding progress is visible should exclude the ends of the part.

To fix these issues the sander was not allowed to have infinite deceleration at the end of the sander travel, and instead used the same maximum deceleration rate as other areas of the part which was set at 0.12 $\frac{\mathrm{m}}{\mathrm{s}^2}$. With this change, the sander will spend only a small period of time at its constant maximum velocity of 0.18 $\frac{\mathrm{m}}{\mathrm{s}}$, better showing the benefits of the proposed material removal depth control method. The updated maximum allowed velocity profile is shown in Fig. 7.1. The area of the part where the participants can see how much they have sanded has also been reduced to exclude one full diameter from each end as shown in Fig. 7.2. This area is also limited in width to mitigate against the differing depths of material removed perpendicular to the motion of the sander. This should help operators better understand their performance in a manner similar to the RMS variation metric used. Also, as normalization is not an issue in this environment a flat part was used instead of the part with constant curvature in the previous experiment.

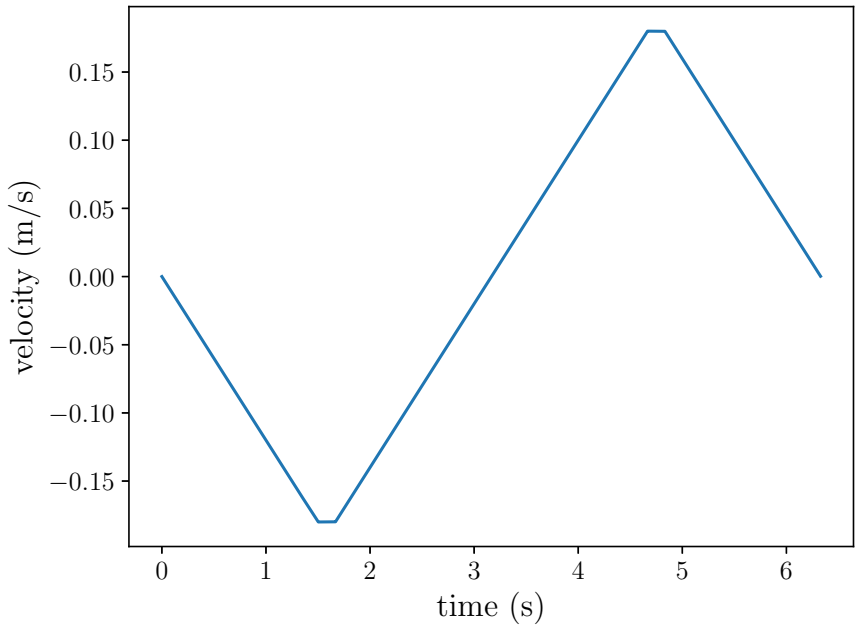

Figure 7.1: The maximum allowed velocity profile in the revised virtual experiment.

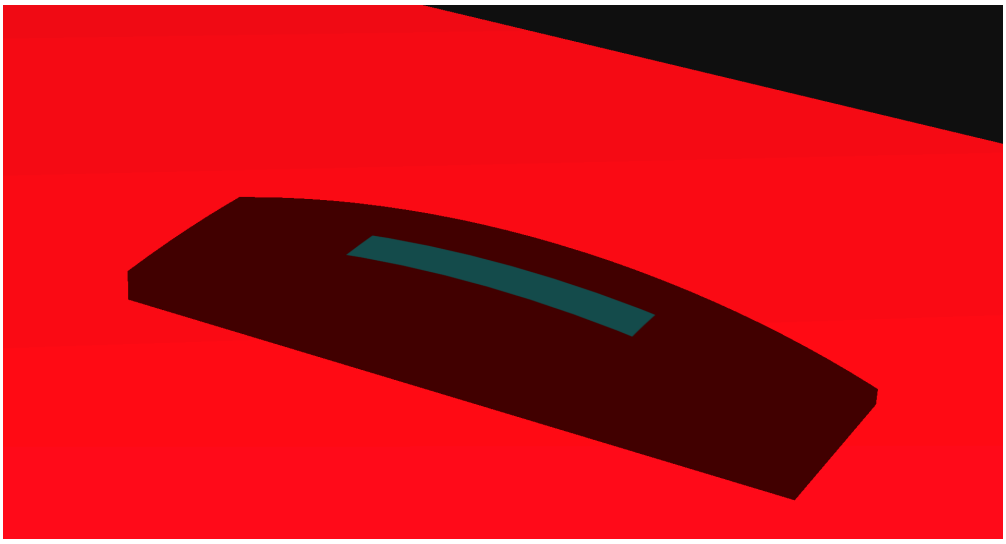

Figure 7.2: The revised virtual experiment curved test article with the limited area where the state of the material removed is visible.

7.0.1 Virtual Environment

Like with the initial virtual experiment, a virtual environment was created. This time, Python was used which allows access to useful scientific packages such as NumPy [53], Matplotlib [54], and SciPy [55]. The 3D rendering for the experiment, shown in Fig. 7.2, was implemented in the Panda3D 3D rendering framework. A game controller was used as a user input device with a joystick commanding the velocity of the sander, and an analog trigger providing the contact force or desired average material removal depth fed to the proposed material removal depth control method.

7.1 Results

This revised virtual experiment was completed by 9 individuals. Again, the RMS variation from the mean is calculated for the center section of the part that the sander passes over, which is also the area where participants can see the progress of their sanding, resulting in the data shown in Fig. 7.3. In this figure it can be seen that there is a reduction in RMS variation of 12.9% when using the proposed material removal depth control method vs a constant contact force on flat surfaces. However, on surfaces with a variable curvature, there is a more pronounced reduction in the RMS variation of 47.4%.

An alternate metric is the min-max variation where the difference between the minimum and maximum amount of material removed is calculated in the region the sander fully passes over. These min-max variation results are shown in Fig. 7.4 and are similar to those obtained using the RMS variation metric.

Participants opinions were measured by asked for their agreement with several statements using a seven point Likert scale [52]. Agreement with the statement “In test A I was able to produce a better end result than in test B” is shown in Fig. 7.5 where the order of the tests was random, but the results have been normalized so that test A uses the proposed material removal depth control method, and test B uses a constant contact force. When sanding a flat part it can be seen that the operators preferences are mixed and there is

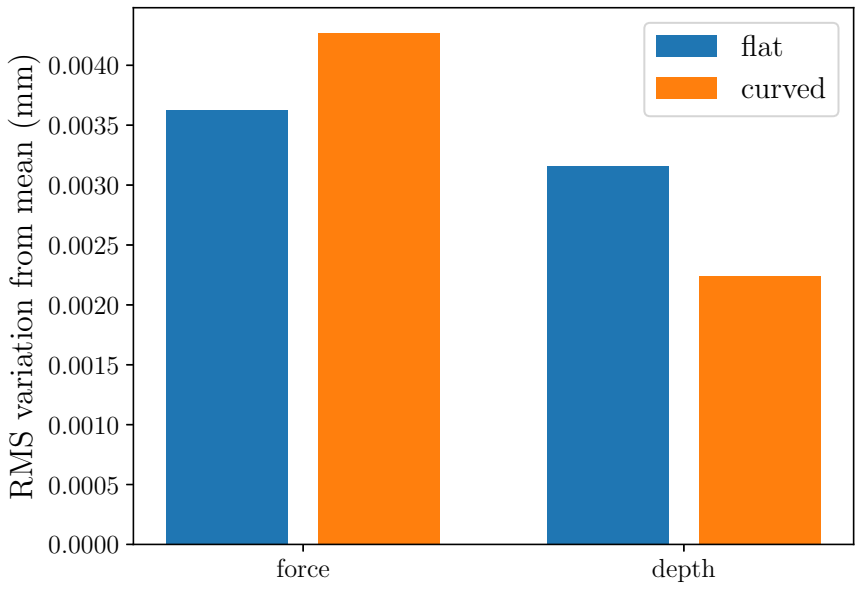

Figure 7.3: The RMS variation from the mean depth of material removed in the center section of the part which the sander fully passes over for the four different experimental conditions in the revised virtual experiment showing better performance when the proposed method is used on a surface with variable curvature and a small improvement when a flat surface is sanded.

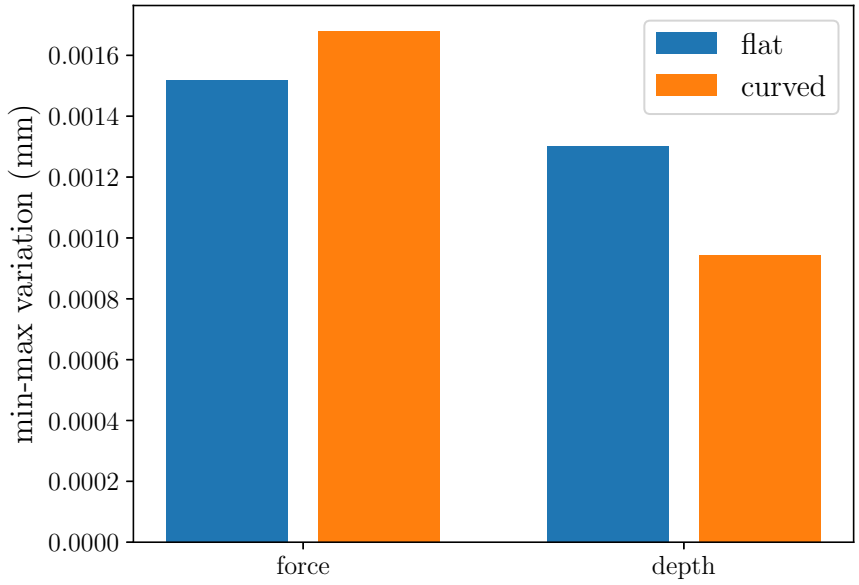

Figure 7.4: The min-max variation of material removed in the center section of the part which the sander fully passes over for the four different experimental conditions in the revised virtual experiment again showing better performance when the proposed method is used on a surface with variable curvature and a small improvement when a flat surface is sanded.

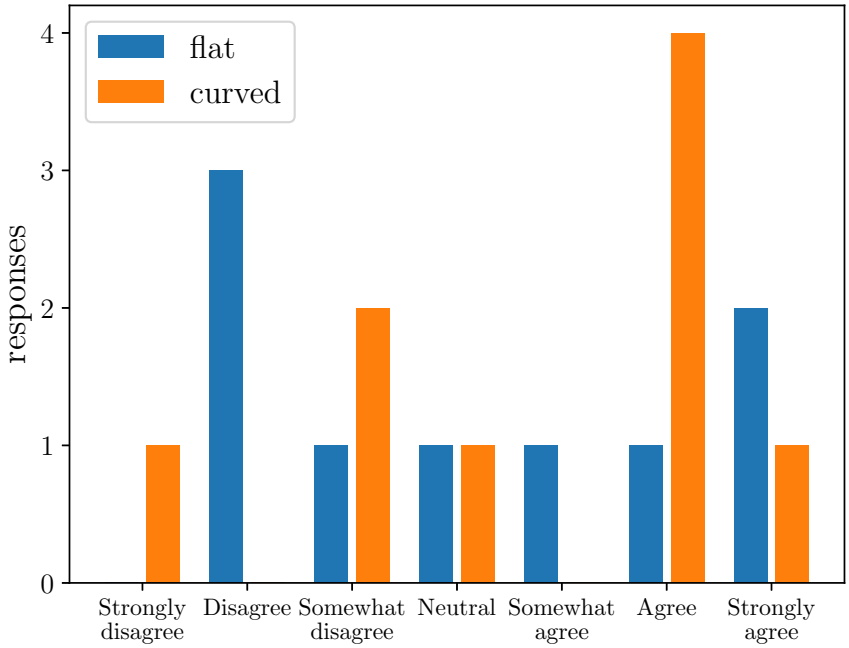

Figure 7.5: Responses to the statement "In test A I was able to produce a better end result than in test B" in the revised virtual experiment where test A uses the proposed material removal depth control method, and test B uses a constant contact force.

not a clear consensus towards either control method. However, when sanding a part with variable curvature, the operators are more likely to prefer the proposed material removal depth control method. The limited improvement in RMS variation on flat surfaces may be making it difficult for the human operator to see any improvement.

When looking at responses to the statement, "I found sanding in test A was more intuitive than in test B", shown in Fig. 7.6, a very similar pattern is present. When sanding a flat part, most participants feel neutral about which method is more intuitive, but when sanding a part with variable curvature, most participants "agree" that the proposed material removal depth control method is more intuitive. Similarly, in Fig. 7.7, showing the responses to the statement, "I preferred the operation of the sander in test A over test B", most participants prefer the material removal depth control method on a part surface with variable curvature,

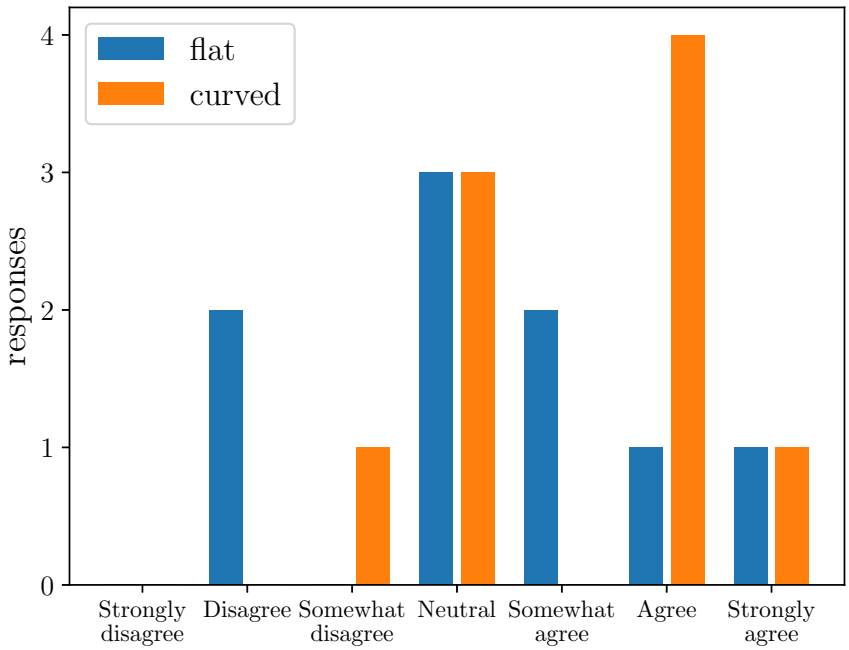

Figure 7.6: Responses to the statement "I found sanding in test A was more intuitive than in test B" in the revised virtual experiment where test A uses the proposed material removal depth control method, and test B uses a constant contact force.

but there is again no clear consensus when sanding a flat surface. While the qualitative data shows no clear winner for flat surfaces, human operators see multiple benefits to the proposed material removal depth control method when sanding surface with a non-constant curvature.

7.2 Conclusion

The results presented in this chapter have shown several useful results. First, it was shown that the proposed material removal depth control method reduces the RMS variation in the depth of material removed on surfaces that are both flat and have a variable curvature. Furthermore, the qualitative results show that human operators prefer the proposed method and think it produces better results when sanding surface with a variable curvature. On flat

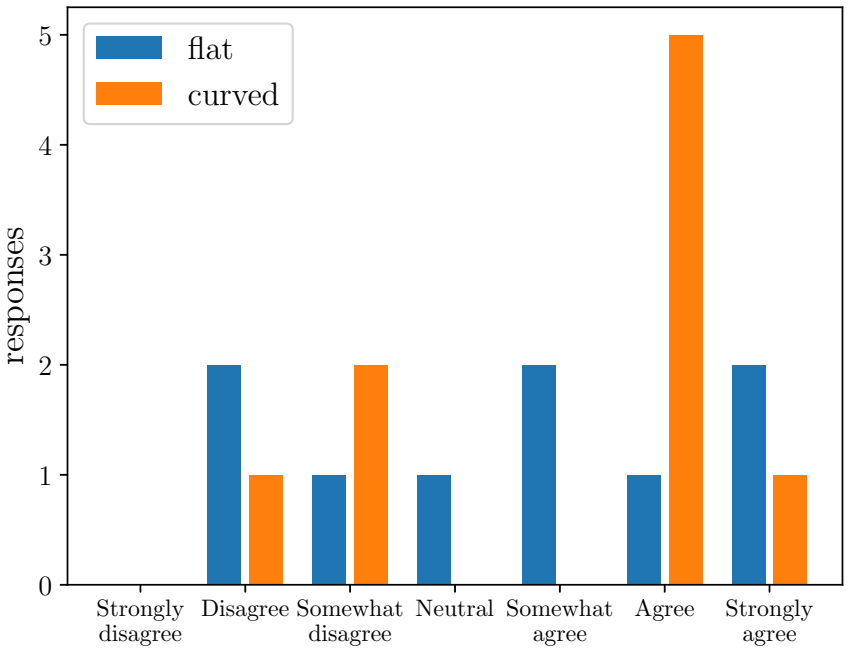

Figure 7.7: Responses to the statement "I preferred the operation of the sander in test A over test B" in the revised virtual experiment where test A uses the proposed material removal depth control method, and test B uses a constant contact force.

Table 7.1: The RMS variation from the mean depth of material removed along the centerline of the part calculated using eq. 4.1 in the center section of the part that the sander completely passes over (ignoring one diameter of the sanding pad from each end) for parts with constant and variable curvature.

	Simulation			Physical		
Curvature	Force Control	Depth Control	Percent Change	Force Control	Depth Control	Percent Change
Constant	0.00362 mm	0.00315 mm	-12.9%	0.0707 mm	0.057 mm	-19.4%
Variable	0.00427 mm	0.00224 mm	-47.4%	0.0878 mm	0.0472 mm	-46.2%

surfaces the operators do not share a clear preference or belief about which control method is better, which is likely due to the smaller reduction in the RMS variation being harder to see visually.

The reduction in RMS variation from this experiment and from the previous experiment in Chapter 6 were collected. This data is presented in Table 7.1. From this table it is easily visible that the physical and virtual experiments match extremely well. This indicates that while the sample size in Chapter 6 was small, increasing the sample size is unlikely to change the results substantially. Interestingly, for surfaces with a constant curvature, the reduction in RMS variation is greater than in the experiment using the virtual environment. This is likely because contoured surfaces, especially in the unconstrained contact area case, resulted in a larger percent change as shown in Table 4.1.

The qualitative results from this experiment and the previous experiment in Chapter 6 can be compared. In general, the results from the experiment using the physical robotic system are more biased towards a constant contact force. Specifically, comparing the responses to the statement "In test A I was able to produce a better end result than in test B" from this experiment (Fig. 7.5) and the previous experiment (Fig. 6.5) shows that both for a variable and a constant curvature the operators are more likely to think that a better result is created with a constant contact force. This is taken to an extreme with the responses to the statement "I preferred the operation of the sander in test A over test B". In this

experiment (Fig. 7.7) the participants felt that the proposed material removal depth control method helped them create a better result both on flat surfaces, and those with a variable curvature. While this result is very clear for surfaces where the curvature is variable, it is less pronounced on flat surfaces. However, in the previous experiment (Fig. 6.7) for both surfaces, the participants strongly preferred a constant contact force. This is likely due to the ability of the operator to visually and audibly sense the force being applied[1]. Overall, many qualitative results show that the proposed method is believed to be superior, and further training and practice would likely improve these results. Furthermore, on all surfaces tested the method derived in Chapter 3 reduces the RMS variation in the depth of material removed.

[1]This is discussed further at the end of Chapter 6.

Chapter 8

CONCLUSION

8.1 Summary

The objective of this thesis is to reduce ergonomic injuries caused by hand sanding of aircraft interior panels. Robotic sanding is a popular approach used to remove the operator from the damaging vibrations of the sander. As the primary purpose of this sanding is to remove excess fairing compound used to repair defects, the common methods of robotic sanding which use a pre-planned path are not compatible. This is because the location and thickness of the fairing compound are unknown. Teleoperation allows a skilled operator to control the sander path in real time, and visually determine when the sanding is complete. However, with teleoperated robotic sanding the operator's sensory perception is reduced making it difficult to effectively control the depth of material removed. For this reason, it is desirable to automatically control the rate of material removal. However, existing methods for controlling the rate of material removal are not compatible with teleoperation since the path of the sander, and the speed along the path are unknown a priori. Therefore, the main contribution of this thesis is a method for controlling the depth of material removed during teleoperated robotic sanding.

8.1.1 Material Removal Modeling and Control

In order to control the depth of material removed during teleoperated robotic sanding, a model of the sanding process must be derived. This model was derived from the Preston equation [14] which was integrated over a straight section of path. To do so a pressure distribution model for flat and convex surfaces, and a sander velocity model was required. The average depth of material removed was then determined from this model. The resulting equation can then be algebraically inverted, in most cases, to determine the contact force

required to achieve a given average depth of material removal. In one contact area case (see Fig. 3.6) algebraic inversion was not possible, so numerical methods must be used. Together, these methods allow the depth of material removed to be controlled during teleoperated robotic sanding.

8.1.2 Sinusoidal Motion: Simulation and Experiment

To ensure the control method performs as designed, validation experiments were performed. For these experiments, a sander moving along a single axis with a sinusoidally varying position was used. Initially, this control method was tested in simulation, then a physical robotic sanding system was also used to ensure the proposed method works in the real world. To evaluate the performance, the RMS variation of the depth of material removed along the centerline of the part is used and compared to a constant contact force. These results are compiled in Table 7.1 showing lower RMS variation when the proposed method is used vs a constant contact force. This indicates that material is removed more evenly with this control method. Specifically, in simulation there is between a 30% and 80% reduction in the RMS variation. When using the robotic sanding system, the reduction was between 20% and 52%. This shows that the proposed method will result in parts that are sanded at least 20% more evenly than with a constant contact force.

8.1.3 Human Robot Interaction

The main contribution of this thesis is a method of controlling the sander contact force to reduce the spatial variation of material removal during teleoperated sanding. Therefore, the method derived in Chapter 3 should be tested with a human operator in the loop. These human robot interaction experiments compare the proposed material removal depth control method with a constant contact force. In these experiments the operator freely moves a sander along a single axis. As the sander removes material, the color of the test article changes proportionally to the material removed. This allows the operator to visually asses

areas where more sanding is necessary and can continue to sand until they are happy with the result. The final surface profiles can then be compared.

Initial Virtual Human Robot Interaction Experiment

First, a virtual environment was constructed to perform this experiment. From this initial experiment it was determined that human operators do a better job when they are able to visually identify areas of the part surface where too much material has been removed. It was also found that at times the operator may wish to sand in a single spot without moving the sander. Because of the design of the depth control method this results in no force being applied and therefore no material removed. To fix this issue, a Gaussian mixture model was fit to velocity data which can be used to detect when the sander is near stationary and a constant force should be applied. While the results from this experiment did not directly support the goal of this test, it did provide valuable insights used in designing later experiments.

Physical Human Robot Interaction Experiment

Utilizing the results from the previous experiment, a similar experiment using the robotic sanding system was undertaken to determine if the proposed depth control method results in more evenly sanded parts. In this experiment along with the quantitative assessment of the RMS variation of the depth, operator opinions were surveyed using a Likert scale. From the resulting data it was found that operators did not feel like the proposed depth control method was intuitive, instead preferring a constant contact force. Further training on the use and functionality of the depth control method could sway this opinion. The results also showed that operators were not able to accurately visually assess the reduction in RMS variation as there was a 19% reduction in the RMS variation when using the proposed depth control method. However, operators believed a constant contact force produced a better end result. In this experiment swarf did obscure the part surface, making it difficult to visually analyze the sanded part. Overall, there is a 46% reduction in the RMS variation of the depth when

using the proposed depth control method on a surface with a variable curvature, while the reduction is 19% when sanding a surface with a constant curvature.

Revised Virtual Human Robot Interaction Experiment

As the sample size in the previous experiment was small, the experiment was replicated in a virtual environment. In this environment there was a 47% decrease in RMS variation on a surface with variable curvature, and a reduction of 13% when sanding a flat surface when the proposed material removal depth control method is used vs a constant contact force. This aligns with the qualitative results which show operators preferred using the proposed depth control method over a constant contact force when sanding a surface with varying curvature. On a flat surface there was no clear consensus. These results match well with the results from the previous experiment, validating those results.

Across all the human robot interaction experiments, operators often felt they produced a better end result when using the proposed material removal depth control method. However, they sometimes felt this control method was not intuitive or preferable. But, in all cases, teleoperated robotic sanding with the proposed material removal depth control method reduced the RMS variation in the depth of material removed. Therefore, if parts need to be sanded via teleoperation, the method for controlling the depth of material removed derived in Chapter 3 can be used to produce a more evenly sanded part.

8.2 Future Work

While the research questions posed in Chapter 1 have been answered, there are many ways in which this research could be expanded.

8.2.1 Orbital Velocity Model

In Chapter 3 a simplified velocity model for an orbital sander was derived. While this model does allow closed form equations for the average depth of material removed to be found in

several contact area cases, it does also a certain amount of error to the model. If the velocity model was not simplified, a more precise model could be created. However, it is likely that this model could only be solved numerically.

8.2.2 Flexible Parts

The model derived in Chapter 3 assumes that the only flexible portion of the system is the sanding pad. However, for many parts, the flexibility of the part itself must be considered. Therefore, this model could be extended to include the effects of deformation of the part on the contact area. This would expand the pool of possible use cases of this model.

8.2.3 Further Qualitative Assessment

There are differences in the qualitative results from the human robot interaction experiments which could be studied further. In particular, the fact that the preferred control method changes between virtual and physical experiments is important to consider as operator preference can influence adoption in an industrial environment. Some specific experiments could be to add simulated sander noise to the experiment in a virtual environment, or to obscure the virtual test article in a similar way as swarf in the physical experiment. Qualitative results of experiments like these may better match the physical experiment, indicating the reasons why the results from the existing experiments differ.

8.2.4 Pressure Distribution Validation

The pressure distribution model used in this thesis has been assumed to be correct, but has not been tested. Testing of the pressure distribution on different part curvatures and with different forces could provide useful information on the expected error of the proposed control method. It could also provide information that could be used to improve the pressure distribution model; however, switching to a nonlinear model could make finding a closed form solution difficult or impossible in many cases.

8.2.5 Sandpaper Wear Modeling

Sandpaper is known to wear out as its abrasive particle become less sharp. This results in it removing less material even with the same process parameters. There are existing methods to estimate the reduction in efficiency [56] which could be integrated with the proposed depth control method to counteract this phenomena. This could improve accuracy of the proposed method, especially for longer sanding tasks, or when a single piece of sandpaper is used on multiple parts.

8.2.6 Cycle Time Reduction

There is a constant desire in manufacturing to decrease cycle times. If the variation in surface height is linearly related to both the duration of sanding, and the contact force, these variables can be traded off with one another to reach a desired state. For example, the contact force could be increased to decrease cycle times, at the expense of increasing the variation in the surface height. However, with approximately a 50% reduction in RMS variation when sanding parts with non-constant curvature using the proposed depth control method, cycles times could be cut in half while maintaining the original quality of work.

8.2.7 Comparison to Other Control Methods

In this thesis the proposed material removal depth control method is compared to a constant contact force. However, there are other control methods that could also be compared such as a constant volumetric material removal rate per unit area. On a flat surface, or when the contact area is otherwise constant, a constant contact force produces a constant volumetric rate of material removal, but on surfaces where the curvature is not constant, this is not the case. As this method of control does account for changes in the part curvature, but not the linear velocity of the sander, it would likely perform better than a constant contact force, but worse than the proposed material removal depth control method.

8.2.8 Applications to Other Tools

While much of the derivation of the control method proposed in this thesis was written for sanding or polishing tools of arbitrary shape or type, at a certain point the characteristics of a round orbital sander were required to derive the control method. As there are many different sanding and polishing tools used for different applications, the control methods for other tools could also be derived. This would require new velocity and pressure distribution functions to be written. Deriving the control methods for other tools would allow others to more easily take advantage of this research.

BIBLIOGRAPHY

[1] K. H. E. Kroemer. Cumulative trauma disorders: their recognition and ergonomics measures to avoid them. *Applied Ergonomics*, 20(4):274–280, December 1989.

[2] Alice Hamilton. Effect of the air hammer on the hands of stonecutters. *Monthly review of the U.S. Bureau of Labor Statistics*, 6(4):25–33, 1918.

[3] Brian D. Curry, James L. W. Bain, Ji-Geng Yan, Lin Ling Zhang, Mark Yamaguchi, Hani S. Matloub, and Danny A. Riley. Vibration injury damages arterial endothelial cells. *Muscle & Nerve*, 25(4):527–534, March 2002.

[4] Yalun Wen and Prabhakar R. Pagilla. Robotic surface finishing of curved surfaces: real-time identification of surface profile and control. In *International Manufacturing Science and Engineering Conference*, volume 3. American Society of Mechanical Engineers, June 2018.

[5] Ariyan M. Kabir, Aniruddha V. Shembekar, Rishi K. Malhan, Rohil S. Aggarwal, Joshua D. Langsfeld, Brual C. Shah, and Satyandra K. Gupta. Robotic finishing of interior regions of geometrically complex parts. In *Volume 3: Manufacturing Equipment and Systems*. ASME, June 2018.

[6] M. J. Tsai, J. F. Huang, and W. L. Kao. Robotic polishing of precision molds with uniform material removal control. *International Journal of Machine Tools and Manufacture*, 49(11):885–895, 2009.

[7] Morgan Quigley, Ken Conley, Brian P. Gerkey, Josh Faust, Tully Foote, Jeremy Leibs, Rob Wheeler, and Andrew Y. Ng. ROS: an open-source robot operating system. In *ICRA Workshop on Open Source Software*, 2009.

[8] Raphael Poiree, Sebastien Garnier, and Benoit Furet. Material removal distribution in robotized random orbital sanding. *Research in Interactive Design*, 4:558–564, 2016.

[9] James B. Taylor, Andres L. Carrano, and Richard L. Lemaster. Quantification of process parameters in a wood sanding operation. *Forest Products Journal*, 49(5):41–46, May 1999.

[10] Daniel E. Saloni, Richard L. Lemaster, and Steven D. Jackson. Abrasive machining process characterization on material removal rate, final surface texture, and power consumption for wood. *Forest Products Journal*, 55(12):35–41, December 2005.

[11] Ariyan M. Kabir, Joshua D. Langsfeld, Krishnanand N. Kaipa, and Satyandra K. Gupta. Identifying optimal trajectory parameters in robotic finishing operations using minimum number of physical experiments. *Integrated Computer-Aided Engineering*, 25:111–135, 2018.

[12] Yingxin Huo, Diancheng Chen, Xiang Li, Peng Li, and Yun-Hui Liu. Development of an autonomous sanding robot with structured-light technology. In *2019 IEEE/RSJ International Conference on Intelligent Robots and Systems (IROS)*, 2019.

[13] Bruno Maric, Alan Mutka, and Matko Orsag. Collaborative human-robot framework for delicate sanding of complex shape surfaces. *IEEE Robotics and Automation Letters*, 5(2):2848–2855, April 2020.

[14] F. W. Preston. The theory and design of plate glass polishing machines. *Journal of the society of glass technology*, 1927.

[15] Karl Theodor Reye. Zur theorie der zapfenreibung. *Der Civilingenieur: Zeitschrift für das Ingenieurwesen*, 6:235–255, 1860.

[16] J. F. Archard. Contact and rubbing of flat surfaces. *Journal of Applied Physics*, 24(8):981–988, August 1953.

[17] Cheng Fan, Ji Zhao, Lei Zhang, Wansong Zhou, and Lining Sun. Local material removal model considering the tool posture in deterministic polishing. *Proceedings of the Institution of Mechanical Engineers, Part C: Journal of Mechanical Engineering Science*, 230(15):2660–2675, 2016.

[18] Fengjie Tian, Zhenguo Li, Chong Lv, and Guangbao Liu. Polishing pressure investigations of robot automatic polishing on curved surfaces. *The International Journal of Advanced Manufacturing Technology*, 87(1):639–646, October 2016.

[19] Lijuan Ren, Guangpeng Zhang, Lu Zhang, Zhen Zhang, and Yumei Huang. Modelling and investigation of material removal profile for computer controlled ultra-precision polishing. *Precision Engineering*, 55:144–153, January 2019.

[20] Dingwei Li, Jixiang Yang, Huan Zhao, and Han Ding. Contact force plan and control of robotic grinding towards ensuring contour accuracy of curved surfaces. *International Journal of Mechanical Sciences*, 227:107449, August 2022.

[21] H. Hertz. Über die berührung fester elastischer körper. *für die reine und angewandte Mathematik*, 92:156–171, 1881.

[22] Deyang Feng, Yuwen Sun, and Huapeng Du. Investigations on the automatic precision polishing of curved surfaces using a five-axis machining centre. *The International Journal of Advanced Manufacturing Technology*, 72(9):1625–1637, June 2014.

[23] Qing-Hui Wang, Yu-Jun Liang, Chen-Yang Xu, Jing-Rong Li, and Xue-Feng Zhou. Generation of material removal map for freeform surface polishing with tilted polishing disk. *The International Journal of Advanced Manufacturing Technology*, 102(9-12):4213–4226, March 2019.

[24] Qizhi Zhao, Lei Zhang, Yanjun Han, and Cheng Fan. Polishing path generation for physical uniform coverage of the aspheric surface based on the archimedes spiral in bonnet polishing. *Proceedings of the Institution of Mechanical Engineers, Part B: Journal of Engineering Manufacture*, 233(12):2251–2263, March 2019.

[25] MuBang Xiao, Ye Ding, Zaojun Fang, and Guilin Yang. Contact force modeling and analysis for robotic tilted-disc polishing of freeform workpieces. *Precision Engineering*, 66:188–200, November 2020.

[26] Chi Fai Cheung, Chunjin Wang, Lai Ting Ho, and Jiangbo Chen. Curvature-adaptive multi-jet polishing of freeform surfaces. *CIRP Annals*, 67(1):357–360, 2018.

[27] Hongyao Zhang, Lun Li, Jibin Zhao, Jingchuan Zhao, and Yadong Gong. Theoretical investigation and implementation of nonlinear material removal depth strategy for robot automatic grinding aviation blade. *Journal of Manufacturing Processes*, 74:441–455, February 2022.

[28] Cheng Fan, Lei Zhang, Qizhi Zhao, Jun Zhao, Ji Zhao, and Lining Sun. Modeling and optimization of material removal influenced by sliding velocity in polishing. *Proceedings of the Institution of Mechanical Engineers, Part B: Journal of Engineering Manufacture*, 233(4):1127–1135, May 2018.

[29] Robert A. Jones. Optimization of computer controlled polishing. *Applied Optics*, 16(1):218, January 1977.

[30] Yunfei Zhang, Fengzhou Fang, Wen Huang, and Wei Fan. Dwell time algorithm based on bounded constrained least squares under dynamic performance constraints of machine tool in deterministic optical finishing. *International Journal of Precision Engineering and Manufacturing-Green Technology*, 8(5):1415–1427, January 2021.

[31] Hon-Yuen Tam, Chiu-Kam Albert Mok, and Ka-Lok Yiu. Tool dwell time computation in computer-controlled surfacing based on constrained optimization. *Machining Science and Technology*, 13(3):356–371, August 2009.

[32] Guifang Zhang, Junwei Wang, Feng Cao, Yuan Li, and Xiaoqi Chen. 3D curvature grinding path planning based on point cloud data. In *12th IEEE/ASME International Conference on Mechatronic and Embedded Systems and Applications*, pages 1–6, Piscataway, New Jersey, 2016. IEEE.

[33] Yun Zhang, Jing Feng Zhi, and Yong Bo Wu. Pressure-based grinding and polishing of free-form lenses with spherical tools. *Key Engineering Materials*, 257-258:401–406, February 2004.

[34] Chen-Yang Xu, Jing-Rong Li, Yu-Jun Liang, Qing-Hui Wang, and Xue-Feng Zhou. Trochoidal toolpath for the pad-polishing of freeform surfaces with global control of material removal distribution. *Journal of Manufacturing Systems*, 51:1–16, April 2019.

[35] Yufeng Ding, Xinpu Min, Weiwei Fu, and Zilong Liang. Research and application on force control of industrial robot polishing concave curved surfaces. *Proceedings of the Institution of Mechanical Engineers, Part B: Journal of Engineering Manufacture*, 233(6):1674–1686, October 2018.

[36] F. Nagata, K. Watanabe, S. Hashino, H. Tanaka, T. Matsuyama, and K. Hara. Polishing robot using a joystick controlled teaching system. In *2000 26th Annual Conference of the IEEE Industrial Electronics Society. IECON 2000. 2000 IEEE International Conference on Industrial Electronics, Control and Instrumentation. 21st Century Technologies*. IEEE, 2000.

[37] F. Nagata and K. Watanabe. Teaching system for a polishing robot using a game joystick. In *SICE 2000. Proceedings of the 39th SICE Annual Conference. International Session Papers*. Soc. Instrum. & Control Eng, 2000.

[38] F. Nagata, K. Watanabe, K. Kiguchi, K. Tsuda, S. Kawaguchi, Y. Noda, and M. Komino. Joystick teaching system for polishing robots using fuzzy compliance control. In *Proceedings 2001 IEEE International Symposium on Computational Intelligence in Robotics and Automation*. IEEE, 2001.

[39] Jung-Hoon Choo, Jae-Yong Lee, and Jae-Won Le. Force-reflecting teleoperation for grinding work. In *Proceedings of 2003 International Conference on Control, Automation and Systems*, 2003.

[40] Vicent Girbes-Juan, Vinicius Schettino, Yiannis Demiris, and Josep Tornero. Haptic and visual feedback assistance for dual-arm robot teleoperation in surface conditioning tasks. *IEEE Transactions on Haptics*, 2020.

[41] Atsuko Enomoto, Koichi Sugimoto, Yoshio Matsumoto, and Isao Todo. Control of polishing work by robot for a difficult case of direct teaching (method for acquiring skill from experts in teleoperation and its control application). *Transactions of the Japan Society of Mechanical Engineers Series C*, 70(693):1433–1440, 2004.

[42] Claudio Gaz, Emanuele Magrini, and Alessandro De Luca. A model-based residual approach for human-robot collaboration during manual polishing operations. *Mechatronics*, 55:234–247, November 2018.

[43] J. Ernesto Solanes, Luis Gracia, Pau Muñoz-Benavent, Jaime Valls Miro, Vicent Girbés, and Josep Tornero. Human-robot cooperation for robust surface treatment using non-conventional sliding mode control. *ISA Transactions*, 80:528–541, September 2018.

[44] Guy Hoffman. *Ensemble: fluency and embodiment for robots acting with humans*. Phd thesis, Massachusets Institute of Technology, September 2007.

[45] Parker Owan. *A learning approach for extending human-robot collaboration to manufacturing-specific tasks*. Phd thesis, University of Washington, 2019.

[46] Aaron Steinfeld, Terrence Fong, David Kaber, Michael Lewis, Jean Scholtz, Alan Schultz, and Michael Goodrich. Common metrics for human-robot interaction. In *Proceeding of the 1st ACM SIGCHI/SIGART conference on Human-robot interaction - HRI '06*. ACM Press, 2006.

[47] Cameron Devine. Material removal rate control for a teleoperated robotic sander. Master's thesis, University of Washington, 2018.

[48] Valentin L. Popov. Method of reduction of dimensionality in contact and friction mechanics: A linkage between micro and macro scales. *Friction*, 1(1):41–62, March 2013.

[49] J. M. is a poor mathematician. How to get the limits of rotated ellipse? Mathematics Stack Exchange, December 2011. `https://math.stackexchange.com/q/91304`.

[50] Carl Friedrich Gauss. Theoria interpolationis methodo nova tractata. 1805.

[51] James W. Cooley and John W. Tukey. An algorithm for the machine calculation of complex fourier series. *Mathematics of Computation*, 19(90):297–301, 1965.

[52] Rensis Likert. A technique for the measurement of attitudes. *Archives of Psychology*, 22:5–55, 1932.

[53] Charles R. Harris, K. Jarrod Millman, Stéfan J. van der Walt, Ralf Gommers, Pauli Virtanen, David Cournapeau, Eric Wieser, Julian Taylor, Sebastian Berg, Nathaniel J. Smith, Robert Kern, Matti Picus, Stephan Hoyer, Marten H. van Kerkwijk, Matthew Brett, Allan Haldane, Jaime Fernández del Río, Mark Wiebe, Pearu Peterson, Pierre Gérard-Marchant, Kevin Sheppard, Tyler Reddy, Warren Weckesser, Hameer Abbasi, Christoph Gohlke, and Travis E. Oliphant. Array programming with NumPy. *Nature*, 585(7825):357–362, September 2020.

[54] J. D. Hunter. Matplotlib: A 2D graphics environment. *Computing in Science & Engineering*, 9(3):90–95, 2007.

[55] Pauli Virtanen, Ralf Gommers, Travis E. Oliphant, Matt Haberland, Tyler Reddy, David Cournapeau, Evgeni Burovski, Pearu Peterson, Warren Weckesser, Jonathan Bright, Stéfan J. van der Walt, Matthew Brett, Joshua Wilson, K. Jarrod Millman, Nikolay Mayorov, Andrew R. J. Nelson, Eric Jones, Robert Kern, Eric Larson, C. J. Carey, İlhan Polat, Yu Feng, Eric W. Moore, Jake VanderPlas, Denis Laxalde, Josef Perktold, Robert Cimrman, Ian Henriksen, E. A. Quintero, Charles R. Harris, Anne M. Archibald, Antônio H. Ribeiro, Fabian Pedregosa, Paul van Mulbregt, and SciPy 1.0 Contributors. SciPy 1.0: fundamental algorithms for scientific computing in Python. *Nature Methods*, 17(3):261–272, February 2020.

[56] Alena Očkajová, Martin Kučerka, Luboš Krišťák, Ivan Ružiak, and Milan Gaff. Efficiency of sanding belts for beech and oak sanding. *Bioresources*, 11(2):5242–5254, April 2016.

[57] barrycarter. Deriving the area of a sector of an ellipse. Mathematics Stack Exchange, April 2017. `https://math.stackexchange.com/q/693430`.

Appendix A
EXPERIMENTAL SETUP

In support of the experiments in Chapters 4 and 6 the details of the experimental setup are described here.

A.1 Robotics Sanding System

The robotic sanding system is built around a Yaskawa HC10 human collaborative robot. To avoid issues, the collaborative power force limiting features were disabled during these experiments. This robot has six degrees of freedom, a reach of 1200 mm, and a payload of 10 kg. To control the robot, the Yaskawa MotoRos driver was used. This allows a Linux computer running ROS [7] to command its motion in near real time[1].

Force control for the system is provided by an Active Contact Flange (model ACF/110/04) made by FerRobotics. This device pneumatically controls the force applied using a proprietary control system which testing shows has a bandwidth of approximately 6 Hz. The force applied by this device can also be modulated in real time via ROS [7].

Finally, a 6 in Sioux orbital sander (model number RO2512-60SRP) is mounted on the force control unit. This sander has a 3/16 in orbital eccentricity and a free speed of 12,000 rpm which is reduced under load. To reduce sand paper clogging a valve was placed in the air line to act as a flow control device. This valve further reduces the rotational velocity of the sander.

---

[1]There is an approximately 250 ms delay between a motion command getting sent to the robot, and the robot beginning the commanded motion

A.2 Test Article Construction

The test articles used in this thesis are built from two layers of PVC film. The film used is Orafol Oracal 631, adhesive backed vinyl film, typically used for signage. The two colors used are yellow (Oracal 631-021 Yello) and blue (Oracal 631-086 Bri B). The film is 3 mils thick and is backed with a water soluble removable adhesive. One piece of each color is used to create a test article.

The test articles were assembled by first scuffing the top surfaces of two pieces of the film. The two scuffed surfaces were then placed together and heated with a heat gun. Once heated sufficiently, a roller was used to compress the pieces together, forming a welded joint. Finally, the backing paper and adhesive were removed, the latter using denatured alcohol.

A.3 Test Article Fixturing

For the experiments the test articles are sanded on a 2000 lb capacity 3×4 ft hydraulic table. A 18 inch square 3/4 inch thick MIC6[2] plate was mounted to the table using screws at three locations to avoid warping the surface. For experiments using a flat surface, the test article is adhered directly to this plate using the PVC film's original adhesive. For experiments on curved surface, an 3D printed ABS plastic surface of known curvature was bolted to the MIC6 plate. For the human robot interaction experiments in Chapter 6, a 3 mm thick piece of rubber was also placed under the 3D printed parts to avoid contact with the WD-40 lubricant used to avoid clogging of the sandpaper.

A.4 Test Article Measurement System

To measure the sanded test articles a 24×36 inch grade B granite surface plate made by Mojave was used. Along with this an SPI digital drop indicator (SPI 21-799-2) was used to measure the height variation on the surface. This indicator has a range of 12.7 mm, an

[2]MIC6 is a stress relieved cast aluminum plate that has been machined to reasonably tight tolerances for thickness ($\pm$0.005 in) and flatness (0.005 in).

accuracy of 0.008 mm, a resolution of 0.002 mm, and has an approximately 3 mm ball tip. An SPI transfer stand (SPI 30-579-7) was used to hold the indicator. For flat parts, the entire MIC6 plate was moved to the surface plate for measurement. When measuring the curved parts, the test article was removed from the 3D printed curved surface and placed on a piece of 11×17 60 lb printer paper. The paper and test article together were then measured on the surface plate with the instruments described earlier in this section.

Appendix B

POTENTIAL EXPERIMENTAL AND MEASUREMENT ERRORS

The experiments performed in Chapters 4 and 6 have multiple potential sources of error, both in the experimental setup and the measurement tools used[1].

B.1 Potential Experimental Errors

In the experimental setup for sanding parts there are several potential sources of error. One of these sources of error is the possibility that the surface being sanded may flex, changing the curvature and normal direction of the surface and leading to differences between the assumed and actual pressure distribution. There is also the possibility of errors in the sanding surface profile, which would also affect the pressure distribution. Similarly, the sanding pad stiffness is known to be nonlinear which further affects the contact pressure. The thickness of the test articles may also not be spatially consistent before sanding, further affecting the results. The delay in the robot executing motion commands, and it's flexibility can also cause errors in the assumed location of the sander. Finally, there is both noise in the force sensor built into the force control unit, and the force control unit's transient response causing the force not be equal to that specified by the control algorithm.

B.2 Potential Measurement Errors

When measuring the sanded test articles, there are several potential sources of error. First is errors in the surface plate flatness which would directly affect the measurements. Similarly, when measuring test articles directly on the MIC6 plate the non-ideal flatness of the plate

[1]The measurement tools used are described in Appendix A.

will affect the results. For test articles sanded on curved surfaces, deviations in the thickness of the paper used will also affect the measurements. There is also the potential for dust and debris to be caught between the surface plate and the paper or between the test article and paper. Finally, the good but inherently limited, accuracy of the indicator used to measure the test article thickness is a source of error.

Appendix C

PARABOLOID VOLUME

To relate the normal force applied to the sander to the pressure distribution an integral equation is derived and must be solved. This integral in some cases has the same form as the volume of a paraboloid. As the equation for the volume of non-circular paraboloids is not readily available it is derived here.

C.1 Derivation

The volume of a paraboloid can be calculated by integrating the areas of the elliptic sections of the paraboloid, $z = \frac{x^2}{a^2} + \frac{y^2}{b^2}$, in the x-y plane. The elliptic section of the paraboloid in standard form is,

$$1 = \frac{x^2}{za^2} + \frac{y^2}{zb^2}, \tag{C.1}$$

which allows existing equations such as for the area of the ellipse to be used. Therefore, the area of the section is $A(z) = \pi zab$. Finally, by integrating the areas of the elliptic sections of the paraboloid up to the height h,

$$V = \int_0^h A(z)\,dz \tag{C.2}$$

$$= \int_0^h \pi zab\,dz \tag{C.3}$$

$$= \frac{\pi h^2 ab}{2}, \tag{C.4}$$

the volume can be found.

C.2 Verification

To check this equation, we can compare to the standard equation for the volume of a circular paraboloid ($a = b$) where the equation has been previously derived by others as,

$$V = \frac{\pi h r^2}{2}, \tag{C.5}$$

where h is identically defined as in eq. C.4, and r is the radius of the paraboloid at $z = h$. In this case the eq. C.1 can be reduced to,

$$z = \frac{x^2}{a^2} + \frac{y^2}{a^2}, \tag{C.6}$$

because $a = b$. Therefore eq. C.4 can be reduced to $V = \frac{\pi h^2 a^2}{2}$. The radius of the paraboloid at a given height z can be found using the equation of a circle, $r^2 = x^2 + y^2$. Therefore, eq. C.6 can be rewritten as,

$$z = \frac{r^2}{a^2}, \tag{C.7}$$

therefore the radius at height h is $r^2 = ha^2$. Substituting this into eq. C.5 the resulting equation is,

$$V = \frac{\pi h^2 a^2}{2}, \tag{C.8}$$

which matches eq. C.4 when $a = b$. This proves that the equation is correct for circular paraboloids and provides some certainty that it is also correct for elliptic paraboloids as well.

Appendix D

PARABOLOID SECTOR VOLUME

When relating the normal force applied to the sander to the pressure distribution an integral equation can result where a portion of the domain is the volume of a sector of a paraboloid. To more succinctly derive the contact force, the general form of this portions of the integral is derived here.

D.1 Derivation

The volume of a sector of a paraboloid can be calculated by integrating the elliptic sector areas of the paraboloid, $z = \frac{x^2}{a^2} + \frac{y^2}{b^2}$, in the x-y plane. The equation,

$$1 = \frac{x^2}{za^2} + \frac{y^2}{zb^2}, \tag{D.1}$$

defines the elliptic cross sections of this paraboloid in the x-y plane. The area of a sector of this ellipse is [57],

$$A(z) = \frac{zab}{2}\left(\tan^{-1}\left(\frac{a\tan(\theta_2)}{b}\right) - \tan^{-1}\left(\frac{a\tan(\theta_1)}{b}\right)\right), \tag{D.2}$$

where θ_1 and θ_2 are angles from the x axis denoting the start and end of the sector respectively, and are both non-negative and less than $\frac{\pi}{2}$. Integrating this equation over a range of z values from 0 to a given height h,

$$V = \int_0^h A(z)\,dz \tag{D.3}$$

$$= \int_0^h \frac{zab}{2}\left(\tan^{-1}\left(\frac{a\tan(\theta_2)}{b}\right) - \tan^{-1}\left(\frac{a\tan(\theta_1)}{b}\right)\right) dz \tag{D.4}$$

$$= \frac{h^2ab}{4}\left(\tan^{-1}\left(\frac{a\tan(\theta_2)}{b}\right) - \tan^{-1}\left(\frac{a\tan(\theta_1)}{b}\right)\right), \tag{D.5}$$

results in an equation for the volume of the sector of the paraboloid.

D.2 Verification

To check this equation it can be compared to the eq. C.4 derived in Appendix C. Using eq. D.5 for the sector of the paraboloid from 0 to $\frac{\pi}{2}$ should be $\frac{1}{4}$ the volume calculated using eq. C.4 since the paraboloid is symmetric across the x and y axes. By setting $\theta_1 = 0$ and $\theta_2 = \frac{\pi}{2}$ eq. D.5 is reduced to,

$$V = \frac{\pi h^2 ab}{8}, \tag{D.6}$$

which is $\frac{1}{4}$ of eq. C.4.

Appendix E

DEPTH CONTROL ALGORITHM CODE

A method for controlling the depth of material removed during orbital sanding was derived in Chapter 3. For various experiments whether simulated, virtual, or physical, required this method to be implemented in Python. The code used is listed below.

```
import numpy as np
from scipy.optimize import minimize_scalar


class OrbitalDepthControl:
    """A class for determining the force required to remove a specific depth.

    This is a class for determining the force required to remove a specific average
    depth of material via orbital sanding. All variables should be in base SI units.

    Attributes:
        kp (float): The Preston coefficient.
        R (float): The sanding pad radius.
        E (float): The orbital motion eccentricity.
        stiffness (float): The stiffness of the sanding pad defined as the modulus
            of elasticity divided by the pad thickness.
        hbar (float): The desired average depth of material to remove.
        omega_m (float): The rotational velocity of the orbital motion.
        k1 (float): The maximum principal curvature.
        k2 (float): The minimum principal curvature.
        vl (float): The linear velocity of the sander.
        phi (float): The angle between the direction of motion and the vector of
            the maximum principal curvature.
    """
    def __init__(self, **kwargs):
        """The class constructor

        Args:
            **kwargs: The keyword arguments set the values of the class attributes
                of the same name to the values supplied in these arguments.
        """
        self.kp = 1.362e-9
        self.R = 44.5 / 1000
        self.E = 4.8 / 1000
```

```
35          self.stiffness = 0
36          self.hbar = 0
37          self.omega_m = 0
38          self.k1 = 0
39          self.k2 = 0
40          self.vl = 0
41          self.phi = np.pi / 2
42
43          self._set_vars(kwargs)
44
45      def _set_vars(self, args):
46          """This function sets the class attributes to the values given in the argument.
47
48          Args:
49              args (dict of str: float): A dictionary where the keys are the class
50                  attributes to set to the value given in the dictionary.
51          """
52          for var, val in args.items():
53              setattr(self, var, val)
54
55      def calculate(self, **kwargs):
56          """Calculates the force to achieve a given average depth of material removed.
57
58          Args:
59              **kwargs: The keyword arguments set the values of the class attributes
60                  of the same name to the values supplied in these arguments.
61
62          Returns:
63              float: The force required.
64              int: The resulting contact area case.
65          """
66          self._set_vars(kwargs)
67          self.vl = abs(self.vl)
68
69          if self.k1 == 0 and self.k2 == 0:
70              return self._calculate_flat(), 0
71
72          if self.k1 > 0 and self.k2 > 0:
73              d = self._calculate_case1_d()
74              if self.R >= np.sqrt(2 * d / self.k2):
75                  return self._calculate_case1_f(d), 1
76
77              f = self._calculate_flat()
78              d = self._calculate_case2_d(f)
79              if self.R <= np.sqrt(2 * d / self.k1):
80                  return f, 2
81
82              d = self._find_case3_d()
83              return self._calculate_case3_f(d), 3
84
```

```
85          raise NotImplementedError
86
87      def _calculate_flat(self):
88          """Calculate the force for a desired depth on flat surfaces.
89
90          This function calculate the force required to achieve a desired average
91          depth of material removed for flat surfaces.
92
93          Returns:
94              float: The force required for the desired depth.
95          """
96          return 2 * self.hbar * self.R * self.vl / (self.E * self.omega_m * self.kp)
97
98      def _calculate_ws(self):
99          """Calculates the width scale factor.
100
101         The width scale factor is the contact width divided by the square root of
102         the max compression distance d.
103
104         Returns:
105             float: The width scale factor.
106         """
107         return 2 * np.sqrt(
108             2 * (np.sin(self.phi) ** 2 / self.k2 + np.cos(self.phi) ** 2 / self.k1)
109         )
110
111     def _calculate_case1_d(self):
112         """Calculates the max pad compression in case 1.
113
114         This function calculates the maximum pad compression distance when the
115         contact area is in case 1, which is also called unconstrained contact.
116
117         Returns:
118             float: The max pad compression distance.
119         """
120         return (
121             self.hbar
122             * self._calculate_ws()
123             * self.vl
124             * np.sqrt(self.k1 * self.k2)
125             / (self.E * self.omega_m * self.stiffness * np.pi * self.kp)
126         ) ** (2 / 3)
127
128     def _calculate_case1_f(self, d=None):
129         """Calculates the contact force for case 1 given the max pad compression.
130
131         This function calculates the contact force given the max pad compression
132         when the contact area is in case 1, which is also called unconstrained
133         contact.
134
```

```
135         Args:
136             d (float, optional): The max pad compression distance. If not supplied,
137                 `_calculate_case1_d` is used to find it automatically.
138
139         Returns:
140             float: The contact force for the desired depth of material removal.
141         """
142         if d is None:
143             d = self._calculate_case1_d()
144         return self.stiffness * np.pi * d**2 / np.sqrt(self.k1 * self.k2)
145
146     def _calculate_case2_d(self, f=None):
147         """Calculates the max pad compression distance given a contact force.
148
149         This function calculates the max pad compression distance given a contact
150         force when the contact area is in case 2, which is also called fully
151         constrained.
152
153         Args:
154             (float, optional): The contact force. If not supplied, `_calculate_flat`
155                 is used to find it automatically.
156
157         Returns:
158             float: The max pad compression distance.
159         """
160         if f is None:
161             f = self._calculate_flat()
162         return (
163             f / (self.stiffness * np.pi * self.R**2)
164             + self.R**2 * (self.k1 + self.k2) / 8
165         )
166
167     def _find_case3_d(self):
168         """Numerically solves for the max pad compression in case 3.
169
170         This function calculates the maximum pad compression distance when the
171         contact area is in case 3, which is also called partially constrained
172         contact. As a closed form solution is not available, numerical optimization
173         is used to find a solution.
174
175         Returns:
176             float: The max pad compression distance.
177         """
178         res = minimize_scalar(
179             self._case3_objective,
180             bounds=(self.R**2 * self.k2 / 2, self.R**2 * self.k1 / 2),
181             method="bounded",
182             options={"xatol": 1e-6},
183         )
184         return res.x
```

```
185
186     def _calculate_case3_theta(self, d):
187         """Calculates the contact area transition angle.
188
189         Returns:
190             float: The contact area transition angle.
191         """
192         return np.arctan(
193             np.sqrt((self.R**2 * self.k2 - 2 * d) / (2 * d - self.R**2 * self.k1))
194         )
195
196     def _calculate_case3_f(self, d):
197         """Calculates the contact force from the max pad compression in case 3.
198
199         This function calculates the contact force from the given max pad compression
200         distance when the contact area is in case 3, which is also called, partially
201         constrained contact.
202
203         Args:
204             d (float): The max pad compression.
205
206         Returns:
207             float: The required contact force.
208         """
209         theta = self._calculate_case3_theta(d)
210         return (
211             4
212             * self.stiffness
213             * (
214                 d**2
215                 / (2 * np.sqrt(self.k1 * self.k2))
216                 * (np.pi / 2 - np.arctan(np.sqrt(self.k1 / self.k2) * np.tan(theta)))
217                 + d * self.R**2 * theta / 2
218                 - self.R**4 / 16 * self.k2 * (theta + np.sin(2 * theta) / 2)
219                 - self.R**4 / 16 * self.k1 * (theta - np.sin(2 * theta) / 2)
220             )
221         )
222
223     def _calculate_case3_hbar(self, d):
224         """Calculates the average depth of material removed in case 3.
225
226         This function calculates the average depth of material removed given the
227         maximum pad compression distance.
228
229         Args:
230             d (float): The max pad compression.
231
232         Returns:
233             float: The average depth of material removed.
234         """
```

```
235         f = self._calculate_case3_f(d)
236         w = self._calculate_case3_width(d)
237         return self.E * self.omega_m * f * self.kp / (w * self.vl)
238 
239     def _calculate_case3_width(self, d):
240         """Calculates the width of contact in case 3.
241 
242         Args:
243             d (float): The max pad compression.
244 
245         Returns:
246             float: The contact width for the value of `d`.
247         """
248         return min(2 * self.R, np.sqrt(d) * self._calculate_ws())
249 
250     def _case3_objective(self, d):
251         """The objective function for finding d in case 3.
252 
253         This objective function is used when determining the max pad compression
254         in case 3, also called partially constrained contact.
255 
256         Args:
257             d (float): The max pad compression.
258 
259         Returns:
260             float: The absolute error between the desired and actual average
261                 depth of material removed values.
262         """
263         return np.abs(self.hbar - self._calculate_case3_hbar(d))
```